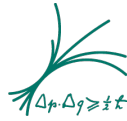Technical University of Munich
Department for Physics

Max Planck Institute for Physics

**Master's Thesis
in Nuclear, Particle and Astrophysics**

Application of a TRISTAN Silicon Drift Detector as Forward Beam Monitor in KATRIN

Supervisor:	Prof. Dr. Susanne Mertens
Author:	Korbinian Urban
Date:	December 9, 2019

I hereby declare that I have written the present master's thesis independently only using the cited external resources.

Korbinian Urban
Munich, December 9, 2019,

Primary reviewer: Prof. Dr. Susanne Mertens
Secondary reviewer: Prof. Dr. Stefan Schönert

Abstract

Sterile neutrinos are a minimal extension of the Standard Model of particle physics. This particle, if it exists, could solve some fundamental open questions in particle physics, as well as astrophysics and cosmology. For example, with a mass in the keV regime, it is a viable candidate for dark matter.

The TRISTAN project within the KATRIN experiment investigates the option of searching for the signature of a keV-scale sterile neutrino in the β-decay spectrum of tritium. This requires a novel detector system for high-rate β-spectroscopy. The most suitable design is a multi-pixel Silicon Drift Detector (SDD) focal plane array. The characterization of the first 7-pixel prototypes with $2\,\mathrm{mm}$ pixel diameter showed their excellent performance, with an energy resolution of $\Delta E_{\mathrm{FWHM}} = 260\,\mathrm{eV}$ at $14\,\mathrm{keV}$ and a shaping time below $1\,\mathrm{\mu s}$. Low shaping times are essential for detecting high-rates in the order of 10^5 cps per pixel.

Within this thesis a 7-pixel TRISTAN prototype Silicon Drift Detector was integrated as Forward Beam Monitor (FBM) in the KATRIN beam line. Situated before the large KATRIN main spectrometer the FBM continuously monitors the high flux of beta electrons. Beyond that, the high resolution of the SDD detector allows to investigate the spectral shape of the tritium β-decay spectrum, and hence to search for the signal of sterile neutrinos. The detector features seven hexagonal pixels with a small pixel diameter of $250\,\mathrm{\mu m}$.

As a first step the necessary hardware, including a new detector board, mounting structure, shielding and cables, was designed and assembled. Before the installation in KATRIN, the fully integrated system was characterized in a test stand at MPP with electron and photon calibration sources. A special focus was put on the characterization of charge sharing between pixels, as this effect is especially relevant for small pixel sizes. In this context a model of charge sharing for photons and electrons was developed. As a result, it could be shown that the measured distribution of charge sharing events is consistent with a Gaussian shaped charge cloud of $20\,\mathrm{\mu m}$ width.

In summer 2019 the new FBM detector was successfully installed and commissioned in the KATRIN setup. The first tritium data was taken in autumn 2019. The detector achieved its goal to monitor the activity of the tritium source on the $0.1\,\%$ level on a time scales of a several hours. On a longer time scale a declining rate of $1.5\,\%$ per month was observed, which is currently under investigation.

To enable a sensitive sterile neutrino search a precise model for the tritium spectrum over a wide energy range is necessary. In this thesis a simplified model of the full tritium spectrum, including the most relevant detector effects, was developed. A good agreement of this model and the spectral shape above $10\,\mathrm{keV}$ could be demonstrated. Finally, the statistical sensitivity of the FBM detector to sterile neutrinos was computed. For a measurement time of $50\,\mathrm{d}$, a sensitivity for sterile mixing on the level of 2×10^{-5} could potentially be achieved, which would supersede current laboratory-based bounds.

Contents

Contents

1. Introduction

1.1. Neutrino Physics

Neutrinos are elementary particles, described as leptons in the Standard Model of particle physics. Similar to the charged leptons e, μ, τ, they come in three flavors ν_e, ν_μ, ν_τ. As neutral leptons, neutrinos only take part in the weak interaction.

One famous physics process that involves the neutrino is the β^--decay, where a neutron decays to a proton, an electron and a neutrino:

$$n \rightarrow p + e^- + \bar{\nu}_e \tag{1.1}$$

1.1.1. History

The neutrino was first postulated by Wolfgang Pauli in 1930. He proposed a not detectable particle to explain the continuous energy spectrum of the β-decay. A few years later Enrico Fermi developed the corresponding theory to describe the β-decay. It took more than 20 years until in 1956 the existance of the neutrino could finally be proven experimentally by Cowan and Reines [1]. They were able to detect the $\bar{\nu}_e$ flux from a nuclear reactor by the inverse β-decay on protons:

$$p + \bar{\nu}_e \rightarrow n + e^+ \tag{1.2}$$

In the following years several experiments detected neutrinos of different origins and flavors. One of these pioneer experiments was the Homestake experiment [2], which measured the ν_e flux from the sun for the first time. Compared to the theoretical prediction, less neutrinos were observed than expected. This disagreement, known as the solar neutrino problem and was later confirmed by other solar neutrino experiments.

The solar neutrino problem can be explained if the three flavor eigenstates $|\nu_e\rangle$, $|\nu_\mu\rangle$ and $|\nu_\tau\rangle$ are a superposition of three mass eigenstates $|\nu_1\rangle$, $|\nu_2\rangle$ and $|\nu_3\rangle$. This mixing of flavor and mass eigenstates is described by the Pontecorvo-Maki-Nakagawa-Sakata (PMNS) matrix

$$\begin{pmatrix} |\nu_e\rangle \\ |\nu_\mu\rangle \\ |\nu_\tau\rangle \end{pmatrix} = \begin{pmatrix} U_{e1} & U_{e2} & U_{e3} \\ U_{\mu1} & U_{\mu2} & U_{\mu3} \\ U_{\tau1} & U_{\tau2} & U_{\tau3} \end{pmatrix} \begin{pmatrix} |\nu_1\rangle \\ |\nu_2\rangle \\ |\nu_3\rangle \end{pmatrix}. \tag{1.3}$$

Thanks to the mixing, neutrinos can change their flavor during propagation [3]. In 2001 the SNO experiment finally prooved that the missing solar ν_e flux was corresponding

to an appearing ν_μ flux [4]. The change of the neutrino flavor during propagation was not only observed for solar neutrinos: Detectors measuring reactor neutrinos (e.g. KamLAND [5]) and atmospheric neutrinos (e.g Super-Kamiokande [6]) observed the effect of neutrino flavor oscillation. The probability of oscillation can be calculated by

$$P_{\nu_e \to \nu_\mu}(t) = |\langle \nu_e(t)|\nu_\mu \rangle|^2. \tag{1.4}$$

Since the propagation of the wave functions is calculated in the mass eigenstates $|\nu_1\rangle, |\nu_2\rangle, |\nu_3\rangle$, $\langle \nu_e(t)|$ can be written as

$$\langle \nu_e(t)| = \sum_i U_{ei}^* \cdot e^{iEt} \langle \nu_i|. \tag{1.5}$$

Assuming only two mass eigenstates and the relativistic approximation $E_i \approx E + \frac{m_i^2}{2E}$, a simplified equation for the oscillation probability is obtained

$$P_{\nu_e \to \nu_\mu}(t) = \sin^2(2\theta) \sin^2 \left(\frac{\Delta m^2}{4E} L \right), \tag{1.6}$$

where L is the propagated distance, and $\sin^2(2\theta) = 4U_{e1}U_{\mu 1}U_{e2}U_{\mu 2}$ is the mixing amplitude in the PNMS matrix. The observation of neutrino oscillations implies a non-zero Δm^2, which is the squared mass difference between the mass eigenstates. The current values, obtained by various experiments, are summarized in table 1.1.

1.1.2. Neutrino Mass

Oscillation experiments measure the Δm^2 between the mass eigenstates but are not sensitive to the absolute scale of the neutrino mass. There are currently three experimental approaches to measure the absolute neutrino mass:

Cosmology Neutrinos are very abundant in the universe. Today still 340 neutrinos per cm^3 are relic from the big bang [7]. This big number of neutrinos played an important role during the large-scale structure formation of the universe. They contribute to the overall mass density, but are not trapped in the small-scale gravitational wells formed by ordinary matter and cold dark matter. The sum of the neutrino masses

$$m_\nu = \sum_i m_i \tag{1.7}$$

Table 1.1.: Current experimentaly determined mixing parameters of the neutrinos, assuming normal order. Details can be found in [7].

$\sin^2(\theta_{12}) =$	0.307 ± 0.013	$\Delta m_{12}^2 =$	$(5.43 \pm 0.18) \times 10^{-5}\,\mathrm{eV}^2$
$\sin^2(\theta_{23}) =$	0.51 ± 0.12	$\Delta m_{23}^2 =$	$(2.51 \pm 0.05) \times 10^{-3}\,\mathrm{eV}^2$
$\sin^2(\theta_{13}) =$	$(2.21 \pm 0.08) \times 10^{-2}$		

therefore has an influence on the expected matter power spectrum in the universe today. Depending on the underlying cosmological models and measured data sets, the resulting cosmological limit on the neutrino mass ranges from $m_\nu < 0.73\,\text{eV}$ to $m_\nu < 0.12\,\text{eV}$ (at 95 % C.L.) [7]. The cosmological limits on the neutrino mass are model dependent, and usually based on the λCDM model [7], which describes the evolution of the universe.

Search for $0\nu\beta\beta$**-decay**   The double β-decay ($2\nu\beta\beta$) is the simultaneous appearance of two β-decays in one nucleus. It can be observed in several isotopes where the single β-decay is energetically forbidden, e.g. ^{76}Ge. As the $2\nu\beta\beta$-decay is a second order weak process, these isotopes have very long lifetimes of 10^{18} to $10^{22}\,\text{y}$. In this process two $\bar{\nu}_e$ are created.

The $0\nu\beta\beta$-decay is a double beta decay where no neutrino is emitted. This can be illustrated as if a virtual outcoming neutrino of one β-decay serves instantaneous as incoming antineutrino for another inverse β-decay. This requires the ν and $\bar{\nu}$ to be the same particle, which is only possible if the neutrino is a massive Majorana particle. In this case the only difference between ν and $\bar{\nu}$ is its helicity, which is not conserved for massive particles. The half live of the $0\nu\beta\beta$-decay is related to the Majorana mass of the neutrino:

$$m_{\beta\beta} = \left| \sum_i U_{ei}^2 m_i \right| \tag{1.8}$$

Up to now no $0\nu\beta\beta$-decay has been observed. The GERDA experiment for example states a limit for the ^{76}Ge $0\nu\beta\beta$-decay half-life of $T_{\frac{1}{2}} > 8 \times 10^{25}\,\text{y}$. This gives a limit $m_{\beta\beta} < 0.26\,\text{eV}$ on the Majorana neutrino mass [8]. Nevertheless, if the neutrino is not a Majorana particle, no statement about its mass can be made with the $0\nu\beta\beta$-decay.

Kinematics of β**-decay**   A non-zero neutrino mass has an influence on the spectrum of the β-decay. The mass of the neutrino reduces the maximum energy the β-electron can receive in the decay. Besides this, also the shape of the spectrum close to the endpoint changes due to the phase space factor in the Fermi theory which describes the β-decay. As the electron antineutrino is involved in the β-decay, the spectrum is sensitive to the effective electron antineutrino mass:

$$m_\beta = \sqrt{\sum_i |U_{ei}|^2 \cdot m_i^2} \tag{1.9}$$

A very promising β emitter to study the neutrino mass is tritium. On the one hand it has a low endpoint energy of only $E_0 = 18.6\,\text{keV}$, which leads to a high count rate close to the endpoint region. On the other hand the tritium decay is a superallowed β-decay with a short half-life of $T_{1/2} = 12.3\,\text{a}$. This is advantageous as a high β-electron rate can be observed already at low source densities. The differential β-spectrum of tritium
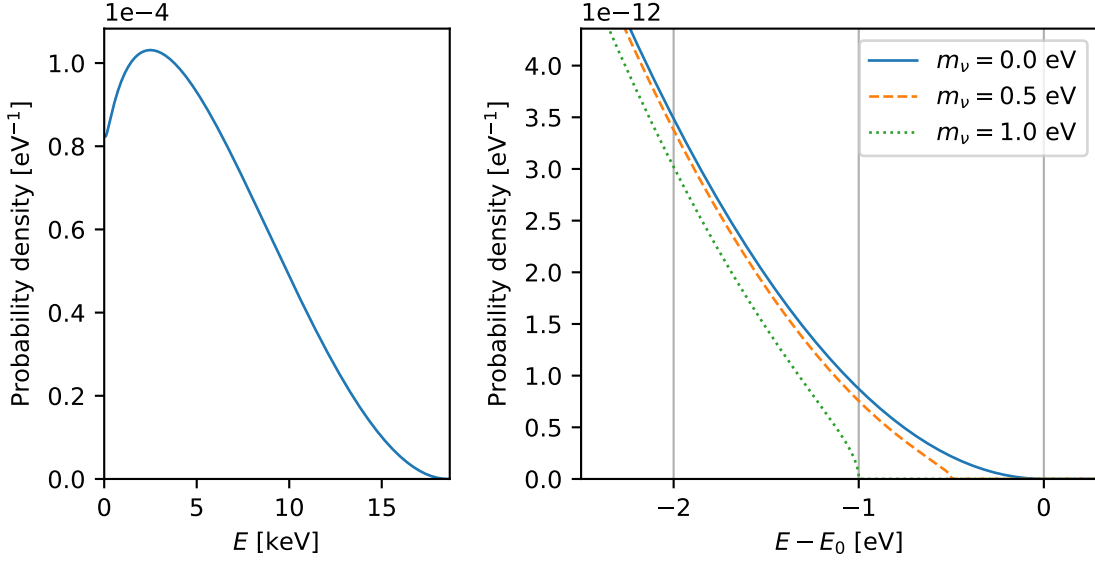
Figure 1.1.: Differential electron spectrum of tritium, based on [9]. The right plot shows a zoom into the endpoint region when assuming different neutrino masses. The probability for an electron to have an energy within the range of the right plot is less than 5×10^{-12}.

can be calculated by

$$
\begin{aligned}
\frac{d\Gamma}{dE} &= C \cdot F_C(E) \cdot p_e E_e \cdot p_\nu E_\nu \\
&= C \cdot F_C(E) \cdot \sqrt{(E + m_e)^2 - m_e^2} \cdot (E + m_e) \cdot \sqrt{(E_0 - E)^2 - m_\nu^2} \cdot (E_0 - E).
\end{aligned}
\tag{1.10}
$$

where E is the kinetic energy of the electron, E_0 is the endpoint energy, C is a constant that absorbs the nuclear matrix element and $F_C(E)$ is the Fermi function that takes into account the electromagnetic interaction of the outgoing electron with the daughter nucleus. Further details on the calculation of the differential tritium spectrum can be found in [9].

The differential tritium spectrum and the influence of a neutrino mass is shown in figure 1.1. An experiment following the approach to measure the neutrino mass by studying the tritium β-decay spectrum is KATRIN, which will be described in more detail in section 1.2. The KATRIN experiment recently published a current upper limit on m_β of $1.1\,\mathrm{eV}$ (90 % C.L.) [10].

1.1.3. Sterile Neutrinos

Figure 1.2 shows the fermions of the Standard Model. The three active neutrinos take a special role within these: First, their mass ($< 1\,\mathrm{eV}$) is much smaller compared

to all other fermions. Furthermore, as neutrinos only interact weakly, they are only observed as left-handed particles, while all other fermions are observed left- and right-handed. Right-handed neutrinos would not interact in the Standard Model and extend the Standard Model in a natural way. The introduction of a right-handed, hence sterile, neutrino typically leads to the existence of further neutrino mass eigenstates of arbitrary mass. These new mass eigenstate are mostly, but not fully composed of the sterile state (Nevertheless, throughout this work, these new mass eigenstates are called sterile neutrinos.) The key parameters of these new hypothetical particles are its mass and the mixing with the active neutrinos (i.e. their fraction of left-handedness).

The new mass eigenstate can in principle have an arbitrary mass, motivated by the following considerations:

- The introduction of a sterile neutrino can explain the lightness of the active neutrinos: In the Standard Model all fermions get their mass from Yukawa coupling to the Higgs field. If this mechanism is applied to the very light active neutrinos, one has to introduce a very small coupling constant, which seems unnatural [12]. Theories can solve this with the see-saw mechanism, which introduces a Majorana mass term and a sterile neutrino with a mass $\mathcal{O}(\text{TeV})$. A sterile neutrino in this mass range can also be related to the generation of the baryon asymmetry in the early universe through its implications on leptogenesis [7].

- In cosmology a sterile neutrino is a viable candidate for dark matter [12]. The allowed sterile mass m_s is in the $\mathcal{O}(\text{keV})$ scale in this case, and the mixing is below 10^{-7}.

- There are several further motivations to introduce a sterile neutrino with a huge spread of proposed masses. One example is a sterile neutrino in the $\mathcal{O}(\text{eV})$ mass

Figure 1.2.: Fermions of the Standard Model. Every particle has a right- and a left-handed version, but neutrinos are only observed left-handed. Adapted from [11].

range that could solve several anomalies in neutrino experiments. One of these is the reactor anomaly, where less $\bar{\nu}_e$ are observe from nuclear reactors than expected.

Experimental search　As for the active neutrino, one can experimentally observe a sterile neutrino by investigating the β-decay, if its mass is in the range of the observed electron energies. For tritium the imprint of an exemplary sterile neutrino ($m_s = 10\,\text{keV}$ and $\sin^2\theta_s = 0.2$) is shown in figure 1.3. The mixing $\sin^2\theta_s = 0.2$ implies that the observed spectrum is a superposition of two spectra: The "ordinary" spectrum where an active neutrino with negligible mass is produced is contributing 80 %. The remaining 20 % are added by a β-spectrum assuming a heavy sterile neutrino with a mass of $10\,\text{keV}$ is produced. This results in a kink in the overall spectrum, which can be observed experimentally.

The current laboratory upper limit for $\sin^2\theta_s$ is in the order of 10^{-3} for sterile neutrino masses $1\,\text{keV} \lesssim m_s \lesssim 18\,\text{keV}$[13].

One approach to search for sterile neutrinos in the tritium β-spectrum is the TRISTAN upgrade of KATRIN. It aims a statistical sensitivity for $\sin^2\theta_s$ of around 10^{-6} for keV-scale sterile neutrinos up to $m_s = 18\,\text{keV}$.
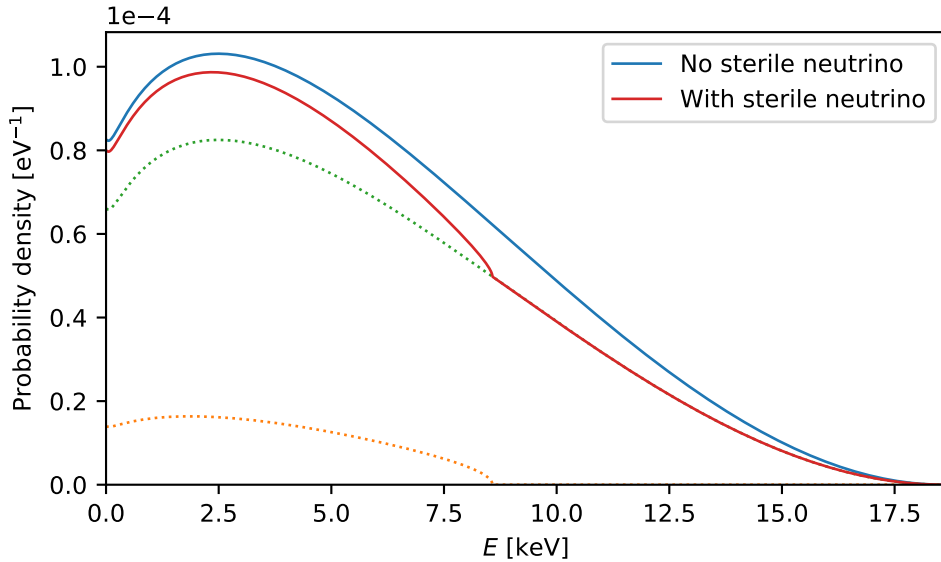

Figure 1.3.: Imprint of a sterile neutrino on the differential tritium spectrum. In this example $\sin^2\theta_s = 0.2$ and $m_s = 10\,\text{keV}$ is assumed. Plot adopted from [13].

1.2. KATRIN

The KArlsruhe TRitium Neutrino experiment (KATRIN) is a tritium β-decay experiment aiming to measure the effective electron antineutrino mass with a sensitivity of 0.2 eV (90 % C. L.). To reach this goal it combines a very stable, high intensity, windowless gaseous tritium source with a high precision electron spectrometer based on the MAC-E filter principle. The following section gives an quick overview over the experimental setup of KATRIN [14]. After that the potential of KATRIN to search for sterile neutrinos is discussed.

1.2.1. Overview

The 70 m long beam line of KATRIN is shown in figure 1.4. Tritium β-decay electrons created in the source are magnetically guided to the spectrometer vessel, which acts as an electrostatic filter. The transmitted electrons are then counted by a detector.

Windowless gaseous tritium source The source of KATRIN is a windowless gaseous tritium source (WGTS). It consists of a 10 m stainless steel tube with a diameter of 9 cm. In the middle of the tube molecular tritium gas is injected with a pressure of 3 µbar and flows in both direction in the tube. Superconducting magnets create a longitudinal magnetic field of 3.6 T to guide the electrons, created in the gas by β-decay, along the beamtube. There is no physical barrier between the source and the spectrometer to allow electrons to reach the spectrometer without scattering. The tritium molecules on the other hand should not leave the source and enter the spectrometer. This is achieved by pumps along the WGTS, which remove the magnetically not con-
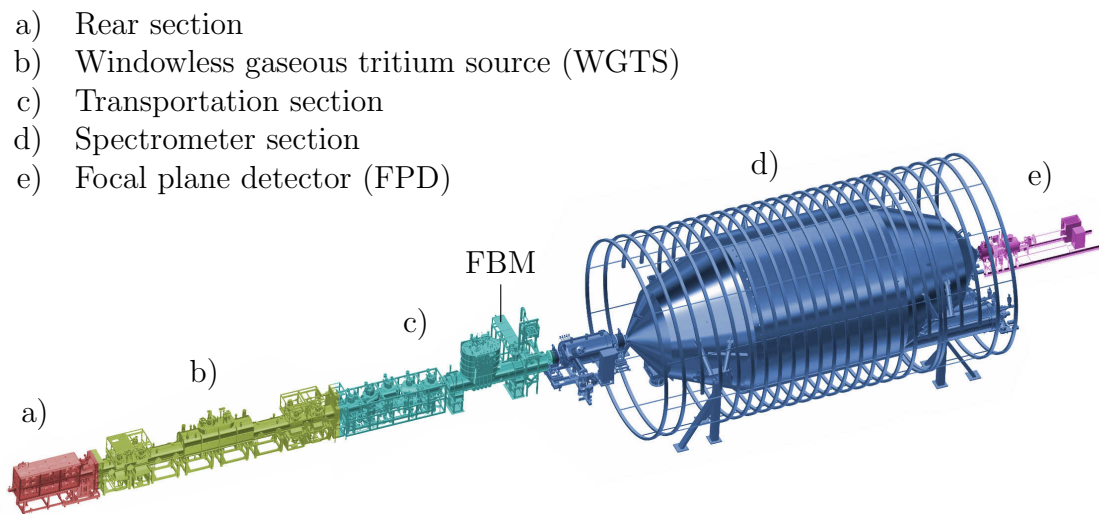
a) Rear section
b) Windowless gaseous tritium source (WGTS)
c) Transportation section
d) Spectrometer section
e) Focal plane detector (FPD)

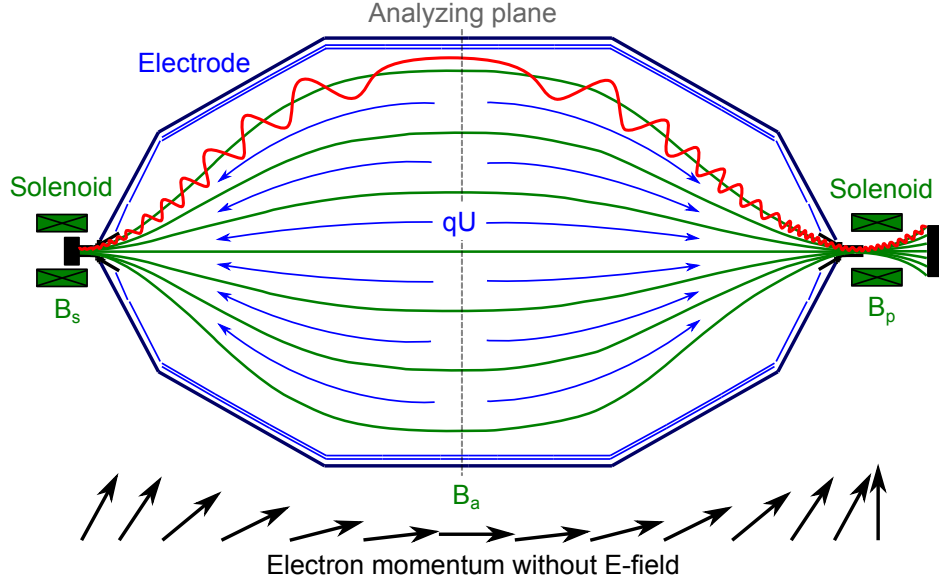**Figure 1.4.:** Overview of the KATRIN beam-line

Figure 1.5.: Scheme of a MAC-E filter. The magnetic field (green) is minimal at the analyzing plane. The trajectory of an electron is shown in red. Adapted from [15].

fined tritium molecules. A closed tritium loop system cleans the pumped tritium gas and feeds it back to the injection capillary. The WGTS is designed to have a T_2 column density of $5 \times 10^{17}\,\mathrm{cm}^{-2}$ leading to a total activity of around $10^{11}\,\mathrm{Bq}$.

Transportation section The transportation section magnetically guides the β-electrons inside the beam tube to the spectrometer section. It is equipped with two pumping sections, where the amount of tritium in the beam tube is further reduced. The first pumping section uses turbo molecular pumps. Then follows a cryogenic pumping section (CPS), which traps residual tritium molecules with an argon frost layer surface operated below $4\,\mathrm{K}$. Furthermore parts of the beam line in the transport section are tilted by 20°, which prevents a direct line of sight between source and spectrometer and helps to stop ions.

Spectrometer section KATRIN uses the MAC-E (Magnetic Adiabatic Collimation combined with an Electrostatic filter) principle to only allow electron above a certain energy to reach the detector. By measuring the rate at different thresholds the integral β-electron spectrum is obtained.

In the large spectrometer vessel (compare figure 1.5) an electrostatic retarding potential rejects all electrons that have a longitudinal kinetic energy $E_\parallel$[1] lower than the set potential. The plane perpendicular to the beam, where the potential reaches its max-

---

[1]In this section an E in a formular corresponds to the kinetic energy, not to be confused with the electric field.

Table 1.2.: Magnetic fields along the KATRIN beam line

Source	$B_{\mathrm{s}} = 3.6\,\mathrm{T}$
Transportation section	$B_{\mathrm{ts}} = 5.6\,\mathrm{T}$
Analyzing plane	$B_{\mathrm{a}} = 3 \times 10^{-4}\,\mathrm{T}$
Pinch magnet	$B_{\mathrm{p}} = 6.0\,\mathrm{T}$

imum is called the analyzing plane. To achieve a good energy resolution on the total kinetic energy $E_{\mathrm{kin}} = \sqrt{E_\perp^2 + E_\parallel^2}$ of the β-electrons, one has to convert their transversal energy to longitudinal energy. This is done by magnetic adiabatic collimation, which is based on the conservation of the magnetic moment μ of each electron along the beam line:

$$\mu = \frac{E_\perp}{B} = \mathrm{const} \tag{1.11}$$

This holds as long as the electrons are guided adiabatically, which means that the gradient of the magnetic flux is small within the cyclotron motion of the electrons. Table 1.2 summarizes the magnetic fields along the beam line[2]. The ratio of the maximum magnetic field in the beam (pinch magnet B_{p}) to the field at the analysis plane B_{a} defines the energy resolution of the filter

$$\frac{\Delta E}{E_{\mathrm{kin}}} = \frac{B_{\mathrm{a}}}{B_{\mathrm{p}}}, \tag{1.12}$$

where ΔE is the maximal $E_\perp$ at the analysis plane. With the magnetic fields stated in table 1.2 an excellent energy resolution of only $0.93\,\mathrm{eV}$ is achieved.

With the conversion from $E_\perp$ to $E_\parallel$ the angle of the electrons $\theta = \arctan\sqrt{\frac{E_\perp}{E_\parallel}}$ changes:

$$\frac{\sin^2\theta_A}{B_A} = \frac{\sin^2\theta_B}{B_B}, \tag{1.13}$$

where A and B are two positions along the beam line. In case of an increasing magnetic field $(B_B > B_A)$ this equation has no solution for a certain $\theta_A > \theta_{A\,\mathrm{max}}$:

$$\theta_{A\,\mathrm{max}} = \arcsin\sqrt{\frac{B_A}{B_B}} \tag{1.14}$$

All electrons with a starting angle larger than $\theta_{A\,\mathrm{max}}$ will be reflected by the magnetic mirror effect. For the KATRIN beam line this means that all electrons in the source created with an angle larger than $\theta_{\mathrm{WGTS\,max}} = 50.8°$ will be reflected by the pinch magnetic field. As the electrons are created isotropically the fraction ϵ of electrons that are magnetically transmitted can be calculated by the solid angle:

$$\epsilon = \frac{\Omega}{4\pi} = \frac{1 - \cos\theta_{\mathrm{WGTS\ max}}}{2} = 0.19 \tag{1.15}$$

---

[2]This is the nominal setting of KATRIN, the values used during the measurement phase later presented in this thesis are slightly different.

1. Introduction

Due to the huge ratio $\frac{B_\mathrm{p}}{B_\mathrm{a}} = 20\,000$ the flux tube of electrons broadens to around $10\,\mathrm{m}$ at the analyzing plane. Therefore the spectrometer vessel in KATRIN has an inner diameter of $9.8\,\mathrm{m}$ and a length of $23\,\mathrm{m}$. The volume of $1400\,\mathrm{m}^3$ is under ultra high vacuum of $10^{-11}\,\mathrm{mbar}$. This is necessary to reduce the detected background, as any electron created by ionization of a residual gas atoms close to the analysis plane will not be distinguishable from a tritium electron.

The KATRIN experiment has two MAC-E filters: The above described main spectrometer and a much smaller pre-spectrometer. The pre-spectrometer is in front of the main spectrometer and rejects most of the low energy electrons. Only electrons close to the interesting endpoint region are entering the main spectrometer, which also reduces the measured background.

Focal plane detector   After the spectrometer section the focal plane detector (FPD) counts how many electrons pass the main spectrometer. By measuring the rate at different retarding potentials in the spectrometer, the integral tritium spectrum is obtained. This procedure requires a very stable source activity, as the different points in the integral spectrum are measured at different times.

Source activity monitoring   An unaccounted shift of the column density ρd during the KATRIN measurements in the order of 10^{-3} can have a significant influence to the measured neutrino mass [14]. Several devices monitor the column density ρd of the WGTS:

- A throughput sensor measures the gas throughput in the injection capillary of the WGTS. With a model for the gas flow in the WGTS tube one can infer the column density.

- The BIXS (Beta Induced X-Ray Spectroscopy) detector measures the X-ray spectrum of the rear wall, which is the rear termination of the flux tube in KATRIN. It is hit by the huge flux of β-electrons of the WGTS. The amount of electron induced X-rays created in the gold surface scales with the source activity of the WGTS.

- An electron gun can shoot a mono-energetic beam of electrons longitudinally through the WGTS. The spectrum, measured using the very precise main spectrometer, gives information about the amount of scattering at T_2 molecules in the WGTS. This way the column density can be calculated.
  For a measurement with the electron gun the tritium measurement of KATRIN has to be paused. Therefore the eelectron gun cannot be measured permanently, but e.g. every week during data taking.

- The Forward Beam Monitor (FBM) is a small silicon detector, which can be moved into the flux tube in the CPS. It directly detects the rate of electrons per area. The FBM is described in more detail in the following section.

1.2.2. Forward Beam Monitor

The FBM measures the electron flux in the beam tube of the transportation section in KATRIN. The concept of the FBM is illustrated in figure 1.6. The flux tube at the FBM position has a diameter of around 15.6 cm. A small silicon detector is inserted to the outer brim of the flux tube, which will not be mapped to the FPD. This detector captures the β-electrons on an event by event basis. By counting the number of detected electrons per detector area the source activity can be estimated. The aimed statistical uncertainty for the measured activity is $1\%_0$[14]. To reach this uncertainty within a reasonable time of e.g one minute, a count rate of 20 kcps is necessary. At full column density the β-electron flux at the FBM is expected to be $1.4 \times 10^6\,\mathrm{s}^{-1}\,\mathrm{mm}^{-2}$, which leads to a required area of the FBM detector of only $0.02\,\mathrm{mm}^2$.
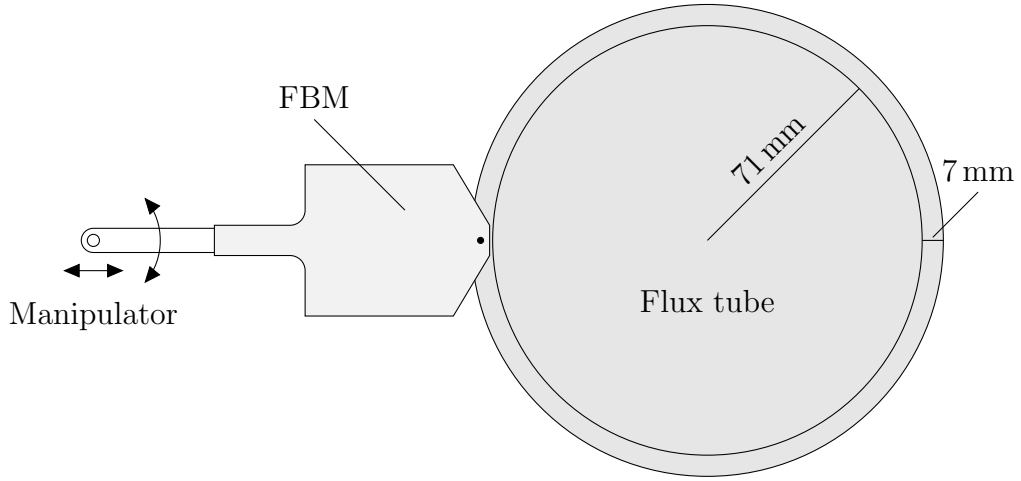

Figure 1.6.: The FBM detector is placed in monitoring position at the outer 7 mm rim of the flux tube. For 2D flux tube scans, the FBM can move to any position in the flux tube by a manipulator. The FBM silicon detector is shown as a small dot.

The FBM detector is mounted on a manipulator which allows to move the detector in x- and y-direction across the flux tube. The y-movement is achieved by rotating a lever arm, as shown in figure 1.6. In addition to the movement in the flux tube a linear guide in x-direction can pull the FBM out of the CPS to its parking position, where the detector is accessible from outside to be maintained or exchanged. Due to the complex CPS environment, the distance between the flux tube and the parking position is about 1.6 m. The movement is controlled by stepper motors outside vacuum and a long bellow in the FBM vacuum chamber allows to move the inside vacuum components. The whole setup of the FBM is shown in figure 1.7. More details about the vacuum and positioning mechanics can be found in [16].

The silicon detector will not be able to measure the low energy part of the continuous β-spectrum, due to a detection energy threshold, which is usually at a few keV. To get a stable rate calculation, a software cut above the hardware threshold is necessary,

as the hardware threshold can depend a lot on e.g. the noise situation on the signals. With a fixed software energy cut, the observed rate is still very sensitive to changes of the detector characteristics, e.g. the gain. Another approach besides the software cut is to fit a modeled differential tritium spectrum to the measured data. In this case the flux is a free parameter in the fit. For both approaches a good energy resolution and well known detector characteristics are very advantageous, for the fit approach a valid model for the detector response is mandatory.

Another possibility to make the measured rate more independent of the detector characteristics would be a post acceleration of the detected electrons. In this case the detector has to be set to a potential of several kV, to make every electron hit the detector with an energy above the threshold. But due to the small form factor and complex technical environment this is not feasibly for the FBM at the moment.
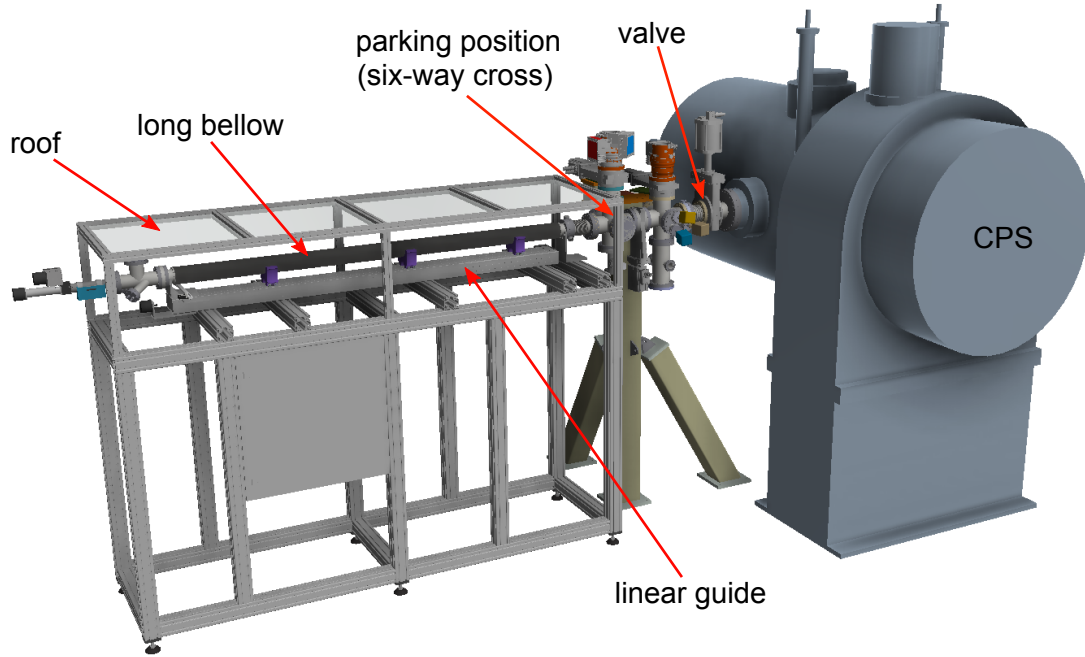

Figure 1.7.: The setup of the FBM. The KATRIN beam tube is axialy inside the CPS. The FBM arm with a length of around 2 m is perpendicular to the beam tube. The long bellow allows to move the FBM detector from the parking position in the 6-way cross all the way into the CPS to the flux tube. The figure shows the setup in parking position. Adapted from [16].

1.2.3. The TRISTAN Project: Searching for Sterile Neutrinos with KATRIN

The TRISTAN (TRitium Investiagtion for a STerile to Active Neutrino mixing) project aims to search for sterile neutrinos with the KATRIN experiment. To detect the possible signature of a sterile neutrino (compare figure 1.3) a large energy range of the tritium spectrum has to be investigated. Instead of an integral spectrum measurement using the MAC-E spectrometer of KATRIN, the differential spectrum over a large energy range can be measured with a silicon detector, which has a good intrinsic energy resolution. The measurement deep into the spectrum comes with a challenge for the detector: By lowering the retarding potential of the main spectrometer, the rates in the detector will increase drastically. To meet these requirements, a new detector setup for KATRIN is currently developed within TRISTAN [13].

The TRISTAN detector The TRISTAN detector is optimized for high resolution ($\Delta E_{\mathrm{FWHM}} < 300\,\mathrm{eV}$) and high rate (total $\mathcal{O}(10^8\,\mathrm{cps})$) β-spectroscopy. The technology behind the new detector is a multi-pixel Silicon Drift Detector (SDD). The final system will consist of several thousand pixels, grouped into modules of 166-pixels each. Each of the pixels has a diameter of 3 mm. The SDD technology is addressed in more detail in section 2.1.

Several 7-pixel prototype detectors, as shown in figure 1.8a, have been produced and characterized with X-rays and electrons. An very good energy resolution[3] of $\Delta E_{\mathrm{FWHM}} = 150\,\mathrm{eV}$ was measured for the 5.9 keV K$_\alpha$ line of Mn [13]. The trapezoidal shaping time for this measurement was below 1 μs, which shows the high rate capability of the detector. Next to X-rays performance, also the detector response to electrons was measured using monoenergetic electrons from either a radioactive conversion electron source or the very defined electron beam of a scanning electron microscope (SEM). The detector response to electrons is dominated by the effects of the entrance window of the detector. Electrons entering the detector will lose some energy in a thin, but not avoidable, not sensitive dead layer. By comparing the measurement with simulations, an effective thickness of the entrance window dead layer was determined to be around 50 nm. With this thin dead layer an energy resolution of 300 eV for 20 keV electrons is achieved [17][18].

The 7-pixel prototype detectors have been successfully used in the MAC-E spectrometer in Troitsk to search for sterile neutrinos. The results were recently published [19]. Currently the first 166-pixel detector module (compare figure 1.8) is under construction. This module will in 2020 be installed in the MAC-E spectrometer of the former Mainz experiment, which is now set up next to the KATRIN spectrometer to monitor its high voltage system. The Mainz and Troitsk spectrometers were the two technical predecessors of the KATRIN experiment. They provide a very realistic environment

---

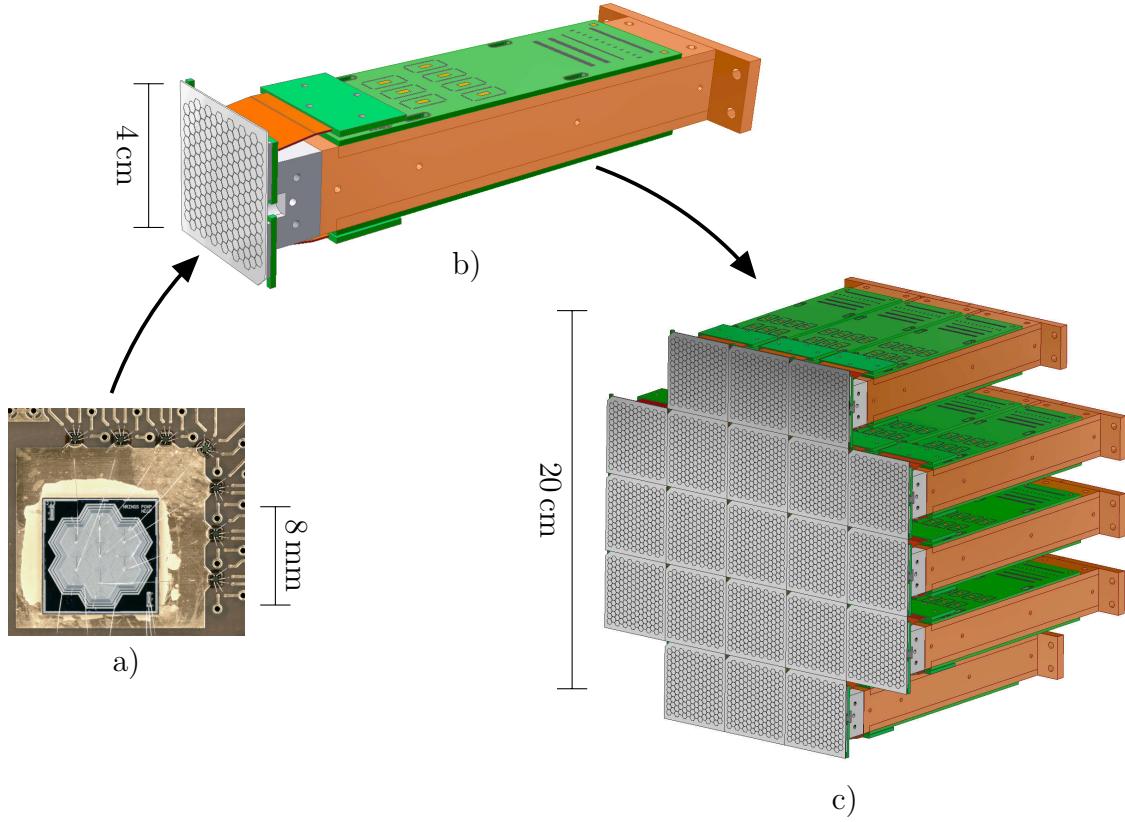[3]The energy resolution is always stated in FWHM in this thesis.

Figure 1.8.: The TRISTAN detector development: **a)** shows a 7-pixel prototype detector. The preamplifiers, which are bonded to the detector pixels, are also visible. **b)** shows a CAD model of one 166-pixel detector module, which is currently under construction. The amplification happens on two PCB boards behind the detector. **c)** shows a CAD model of the final detector, consisting of 21 modules.

for the TRISTAN detectors with respect to its final destination in the KATRIN beam line.

TRISTAN FBM Upgrade   Another application of the 7-pixel TRISTAN prototype detector is the Forward Beam Monitor (FBM) in KATRIN. With its high rate capability and a good energy resolution the TRISTAN detector fits to the requirements of the FBM. The previous detector consisted of two silicon PIN-diodes, with an energy resolution of around $2\,\mathrm{keV}$. The main advantages of the new TRISTAN FBM detector are:

- The entrance window is much thinner, which is favorable to measure electrons.

- The SDD technology achieves better energy resolutions especially at very high rates.

- The hexagonal seven pixel design helps to track partial charge collection at the

border of pixels. This charge sharing effect, which is addressed in section 3.3, has a big influence to the measured spectrum.

The smallest version of the prototype detectors is used, which has an effective pixel diameter of $250\,\mu m$ corresponding to an area of $49 \times 10^{-3}\,mm^2$. With the current KATRIN settings a rate of around $56\,kcps$ per pixel is expected and the aimed statistical uncertainty of $1\,\text{\textperthousand}$ is reached after around $20\,s$, assuming all electrons are detected. This thesis focuses on the design and implementation of this 7-pixel TRISTAN prototype detector into the FBM setup.

2. Design of the TRISTAN FBM Detector

For the implementation of the new SDD detector system as Forward Beam Monitor, several hardware components were replaced. These entail the detector itself, the Printed Circuit Board, the front-end electronics, the bias system, and the DAQ system. To minimize the technical difficulties, the original vacuum feedthrough connector and outside vacuum cables were kept. As a consequence, only two of the seven signal lines are realized with coaxial cables, and the operation of a Hall sensor on the FBM board was no longer possible. In the following the main FBM components are described in detail.

2.1. Silicon Drift Detector

The TRISTAN FBM detector uses one of the prototype Silicon Drift Detectors developed within the TRISTAN project, produced by the Semiconductor Laboratory of the Max Planck Society[20] (HLL). The detector has seven pixels in a hexagonal shape, as shown in figure 2.2.

Working principle of SDDs SDDs are using the depleted volume of a silicon pn-junction to detect ionizing particles. A pn-junction is the interface of two differently doped regions in the silicon: n-type silicon is usually doped with phosphorus, and

Figure 2.1.: Photo of the TRISTAN FBM detector. The small black area between the two bond wires is the entrance window of the seven pixels.
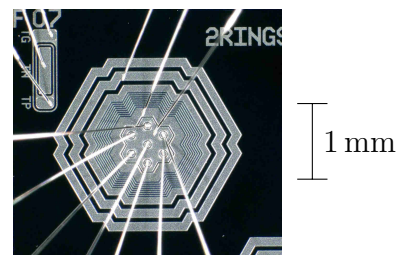

Figure 2.2.: Microscopic image of the anode side of a 7-pixel SDD with 250 μm pixel diameter. Bond wires connect the anodes to the preamplifiers, not shown in this image.

serves as a electron donator. Very simplified, this can be understood as the fifth valence electron of phosphorus not fitting very well into the four-valence structure of the silicon crystal. p-type silicon on the other hand is usually doped with boron, which has only 3 valence electrons and therefore serves as a electron acceptor. At a junction of p- and n-type silicon, the available electrons of the n-type silicon will move to the p-type region. This will build up a space charge region around the junction, until the electric field of the space charge compensates the exchange of more electrons (see figure 2.3). The region near the junction where each atom of phosphorus has donated an electron and each atom of boron has accepted an electron is called depleted area. In this region an electric field is present.

Such a pn-junction can be used as particle detector. When energy is deposited in the depleted area local electron-hole pairs are created. Due to the electric field the electrons and the holes are separated, and cannot recombine, but move to the not depleted regions and can be measured as a reverse current in the diode.

The detector is only sensitive to charge depositions in the depleted region, which is usually very small. The thickness $D_N + D_P$ of the depleted area depends on the donator and acceptor densities in the silicon, and can also be enlarged by reverse biasing the diode with an external voltage. PIN (positive, intrinsic, negative) diode detectors uses these effects to deplete a large silicon volume. They consist of a bulk of very pure intrinsic silicon, which usually is of n-type with a very low donator density. On the top and bottom of the bulk, thin layers of p- and n-type silicon with a high acceptor and donator density are added by doping. By applying a reverse bias voltage of $\mathcal{O}(100\,\text{V})$, the bulk can be fully depleted for a typical waver thickness of $\mathcal{O}(500\,\mu\text{m})$ [22].

A silicon drift detector adds the principle of sideward depletion to this kind of diode: In this case the n-type anode is only a very small spot on the top of the detector volume. The negative biased p-type silicon extends not only on the opposite (entrance window) side of the detector, but also on several drift rings surrounding the anode (compare figure 2.4). By choosing the voltages of the drift rings accordingly, a radial component of the electric field can be achieved in a way that all electrons generated in the depleted
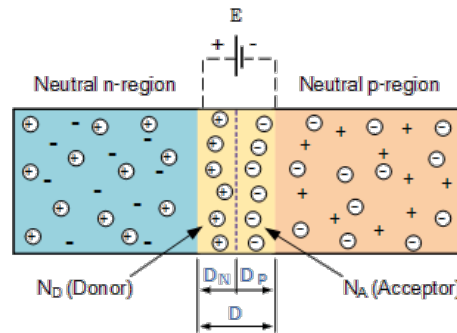

Figure 2.3.: Sketch of a pn-junction. The yellow region at the junction is the depleted area. From [21].
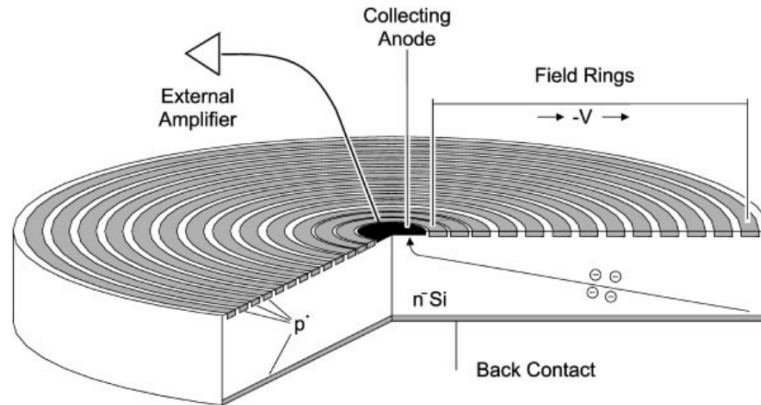
Figure 2.4.: Cross section of a circular SDD detector with 13 drift rings. Electrons are guided by an electric field to the collecting anode in the center. Taken from [23]

volume of the detector are guided to the very small anode [23]. Because of its small sized anode the SDD has a smaller value of the output capacitance compared to a PIN diode of the same format. The small capacitance allows for low noise and high rate operation of the SDD. A drawing of an SDD is shown in figure 2.4.

SDDs can have an area of many mm^2 or even cm^2. The final TRISTAN detector will consist of several thousands of SDD pixels with 3 mm diameter and many drift rings each. The TRISTAN FBM detector on the other hand will only have two drift rings per pixel due to its small pixel diameter of only 0.25 mm. A small size was chosen because of the high electron flux at the FBM position in the KATRIN beamline. On the pixel area of $0.049\,mm^2$ already 5×10^4 incoming electrons are expected per second. A sketch of the electric fields inside the FBM detector is shown in figure 2.5.

Entrance Window The opposite side to the anode is in the following called the entrance window of the detector, as this is the side on which the particles enter the detector volume. In an ideal detector the sensitive volume would start at the entrance window, so that every energy deposition is captured. As it is not possible to deplete the whole p-type silicon layer at the entrance window, a small field-free, not depleted layer remains. This layer is often called dead layer, as energy which is deposited in this layer is not or only partially detected. The thickness of the dead layer is an important property if electrons are the primary particle, like in TRISTAN, because all detected electrons lose some of their energy when passing the dead layer.

The implantation process of the boron at the entrance window of the SDDs for the TRISTAN project was optimized concerning the thickness of the resulting dead layer. The thickness of the dead layer was measured to be around 50 nm for the TRISTAN prototype detectors[17].
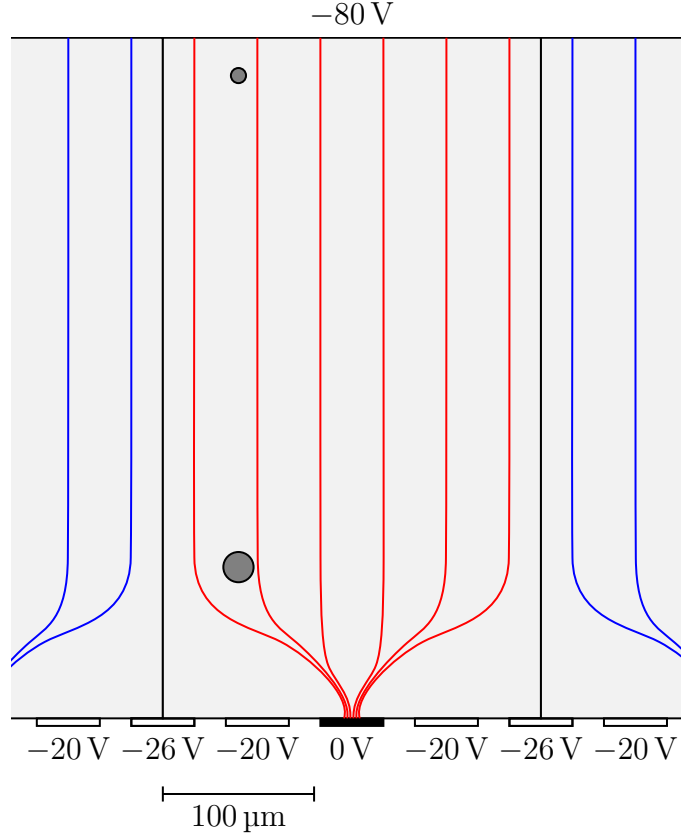
Figure 2.5.: Cross section of the central region of the FBM SDD detector. The red lines qualitatively show the electric field lines starting at the entrance window and reaching the central pixel. The blue lines correspond to field lines reaching the neighboring pixels anode. A charge cloud (grey circle) created close to the entrance window drifts along the electric field lines to the anode. During the drift the size of the charge cloud increases due to diffusion.

Bias Voltages   The TRISTAN FBM SDD detector has four bias voltages for the detector:

- $V_{\mathrm{BC}} = -80\,\mathrm{V}$ (Back Contact) is the voltage applied to the entrance window of the detector. This is the depletion voltage relative to the anode which is at zero potential.

- $V_{\mathrm{BF}} = -90\,\mathrm{V}$ (Back Frame) is the voltage of a ring surrounding the p-type silicon of the entrance window. It helps to define the electric field at the outer border of the outer pixels. It has no influence on the central pixel.

- $V_{\mathrm{R1}} = -20\,\mathrm{V}$ (Ring 1) is the voltage of the innermost drift ring.

- $V_{\mathrm{RX}} = -26\,\mathrm{V}$ (Ring X) is the voltage of the outermost drift ring. It is called ring X to have a independent syntax for different number of drift rings. For the FBM it could also be labeled ring 2.

2.2. Electronics

The electronics that are necessary to run the SDD can be categorized into two main tasks: One is the analog amplification of the detector signals for each of the seven pixels. After the amplification and transmission to outside vacuum the analogue signals are fed into the data acquisition system (DAQ). The second important task of the electronics is the voltage supply. This includes the detector voltages (explicitly $V_{R1} = -20\,\text{V}$, $V_{RX} = -26\,\text{V}$, $V_{BC} = -80\,\text{V}$, $V_{BF} = -90\,\text{V}$), which are necessary to deplete the detector volume and to define proper drift fields, as well as the supply for the amplifiers. All these DC voltages should be supplied with very low noise and ripple. A distortion on the V_{R1} for example, which is only a few micrometers away from the anode, couples strongly to the anode signal, and is amplified by the whole amplification chain.

These tasks are physically placed on two boards, the detector board and the bias board, which will be described in the next two sections.

2.2.1. Detector Board

The detector board is at the very front end inside the vacuum. The SDD is glued onto this board, and the preamplification happens here, as it is important to amplify the signal as close to the detector as possible. On the other hand the board is kept as small and simple as possible, to reduce outgasing in the vacuum and thermal heating of the electronics.

Amplification   The amplification is done by CUBE amplifiers. These are specially developed for the purpose of low-noise charge preamplification for SDDs [24]. The input of these is bonded directly to the anode of the SDD pixels to minimize the capacitance, which is very important to achieve a low noise level. Any current at the anode is integrated at an internal 25 fF capacitor in the CUBE. A typical deposition of 15 keV leads to around 4200 electrons reaching the anode[1]. The voltage increase at the capacitor is then $V = \frac{Q}{C} = 27\,\text{mV}$ which is reasonably large, so that no other main amplification stages are necessary.

The CUBE amplifiers do not operate in the very common continuous reset mode, but in a pulsed reset mode. This means that the output of the integrating amplification is monotonously increasing with the accumulated charge of many events in the detector. After a certain time a reset pulse is necessary to reset the amplifier before it reaches the limit of its output range.

Buffers and cables   The output of the CUBE amplifier should not drive more than around 30 pF. A typical 50 Ω coax cable has a capacitance of $100\,\text{pF}\,\text{m}^{-1}$. This means that the cables to the bias board, which are around 7 m long, cannot be driven by a

---

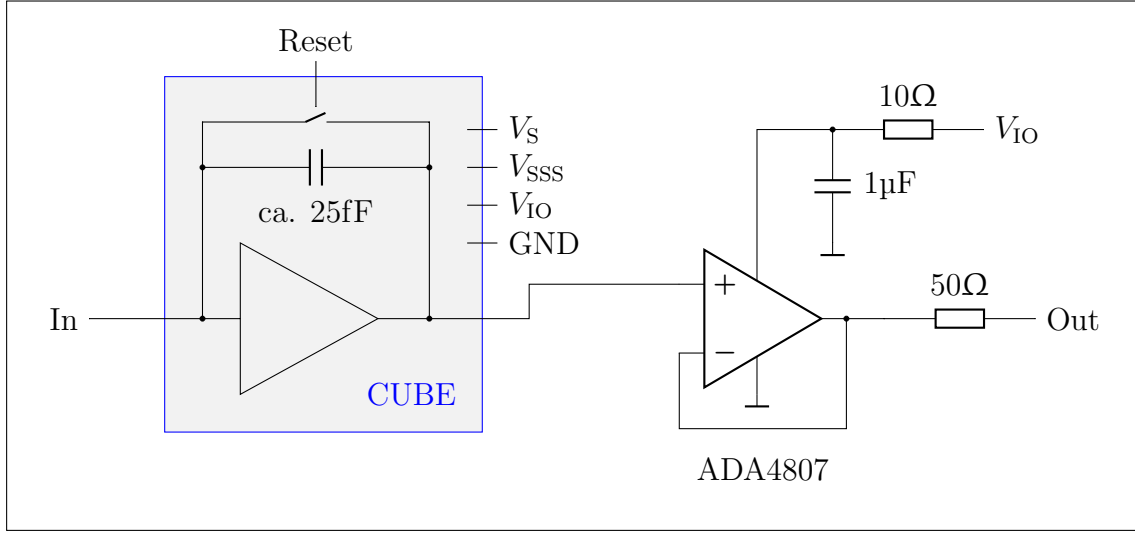[1]Assuming a pair-creation energy $\epsilon = 3.6\,\text{eV}$ [25].

Figure 2.6.: Schematic of the amplification for one pixel on the detector board. The ADA4807 is a double amplifier in a MSOP8 package.

CUBE directly, but a buffer amplifier is needed. This is done by industrial operational amplifiers, which have a low noise, high bandwidth (around 100 MHz is sufficient) as well as a small form factor and low power consumption. These buffers are used only to drive the cables and do not add an amplification. The whole schematic of the signal amplification on the detector board is shown in figure 2.6.

The detector board has a 22-pin custom-made connector. This connector consists of PEEK plastic with a 2×11 array of pogo pins, which are small pins equipped with a spring each, to press a gold plated contact onto the PCB with a defined force. The 22 pads on the detector board can be seen on the left part of the detector board in figure 2.7. This connector and the attached cables in vacuum are part of the already existing FBM setup. An exchange of the cables would be very difficult, as big parts of the vacuum setup would have to be disassembled. Therefore the 22 pins are a constraint for the TRISTAN FBM detector board. As the former FBM had two pixels, there are only two coax lines installed. It is planned that the cables in vacuum are exchanged in the future, to have a coax cable for each pixel of the TRISTAN FBM. Until then only two pixels can be used with coax lines, while the signals of the other five pixels have to be transmitted through non-shielded wires. This has some disadvantages, as there may be cross talk, induced noise, varying line capacitances et cetera. A comparison of the performance of the pixels can be found in section 3.2.

Outgasing measurement   One main constraint for the detector board is the outgasing rate. The FBM is positioned after the pumping sections of KATRIN, directly before the two spectrometer vessels. In these a very low vacuum is mandatory to measure a low background in the detector. For this reason the pressure in the spectrometer is kept at 10^{-11} mbar. The compatibility with the vacuum restricts the allowed materials in
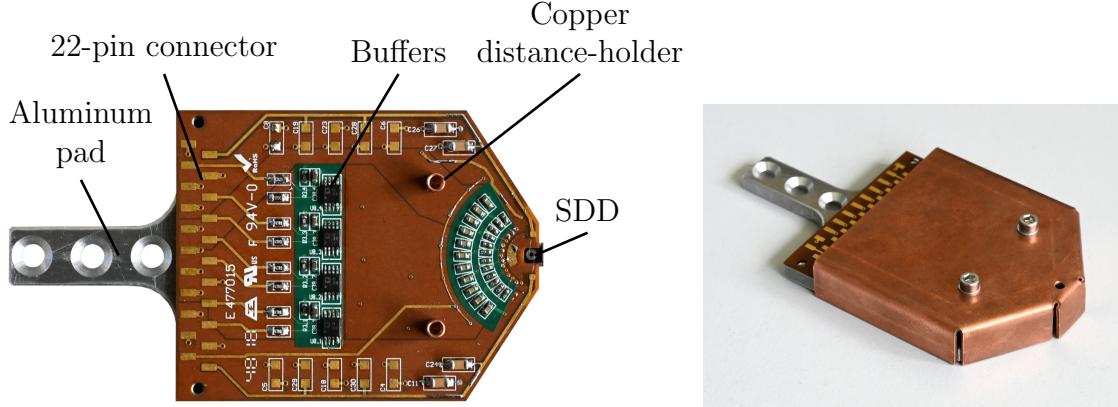
Figure 2.7.: Left: Photo of the detector board, screwed onto the aluminum pad. The entrance window is on the visible side, while the CUBE preamplifiers are on the not shown back side of the board. **Right:** The FBM detector including the copper cover.

the FBM setup. The detector board is not made of FR4, which is the standard material for non-vacuum applications, but polimid (also known as Kapton®). As the outgasing scales with the surface of the material, as few and small SMD parts as possible were used. Furthermore solder resist and paint was used as little as possible.

To check if the used materials are compatible with the high vacuum requirements a measurement of the outgasing rate was performed. For this a dedicated setup in the KIT lab was used [26], which consists of a vacuum chamber with a pump, a heating and precise pressure sensors. The following procedure was followed to estimate the outgasing of the detector board in the final setup:

1. First the chamber is baked out at $90\,°C$ for $120\,h$. The baking reduces the outgasing significantly and is also done at the final setup. During the baking the chamber is pumped.

2. After baking the chamber is cooled to stable room temperature.

3. The valve to the pump is closed and the increase of pressure in this closed system is used to calculate the outgasing rate q of the chamber[2].

4. Repeat steps 1 to 3, this time with the investigated sample inside.

As test sample the plain polimoid detector board together with two of the dual operational amplifiers in a MSOP8 plastic package was used. These components were assumed to be most critical for outgasing. By comparing the rates in the measurement of only the chamber with the measurement with the samples inside the outgasing of the samples can be estimated.

The results shown in table 2.1 are not conclusive, as the outgasing rate with the sample

---

[2]The outgasing rate, which describes the number of particles leaving the suface per second is usually written in the unit $mbar\,L\,s^{-1}$, as $mbar\,L$ corresponds the number of particles according to the ideal gas law.

Table 2.1.: Result of the outgasing measurement. The outgasing of the empty chamber is compared to the outgasing of the chamber with the kapton PCB and two plastic double amplifier packages inside.

	Outgasing rate q
Empty chamber	$1.23 \times 10^{-7}\,\mathrm{mbar\,L\,s^{-1}}$
Sample inside	$0.42 \times 10^{-7}\,\mathrm{mbar\,L\,s^{-1}}$

in the chamber is even lower than the outgasing rate of the empty chamber. This means that the measurement has reached a systematic limit and the two measurements seem to be not reproducible. Nevertheless an upper limit to the outgasing of the samples can be given, which is the measured total outgasing rate with the samples inside:

$$q_{\text{samples FBM}} < 4.2 \times 10^{-8}\,\mathrm{mbar\,L\,s^{-1}} \tag{2.1}$$

To assess this value in terms of the reachable vacuum one has to divide it by the pumping capability installed at the setup. The turbo molecular pump installed at the FBM has a pumping speed of $300\,\mathrm{L\,s^{-1}}$ so that a pressure of around $10^{-10}\,\mathrm{mbar}$ can be reached. This is an acceptable value, considering the much higher pumping speed of the CPS and prespectrometer setups.

2.2.2. Bias Board

The detector board is connected the so-called bias board as shown in figure 2.8. This board is placed outside of vacuum in a closed aluminum box. The bias board is connected to a high voltage (ISEG THQ) and low voltage (HM8040) power supply and to the DAQ system, as shown in figure 2.8. The tasks of the bias board are:

- Supplying the detector voltages. These are obtained from an external DC voltage supply by high ohmic voltage dividers and RC low-pass filters with time constants of several seconds to get rid of all high frequency noise. The output impedance is above $100\,\mathrm{k\Omega}$, which is acceptable as the currents in the FBM detector are below $1\,\mathrm{nA}$. The four detector voltages can independently be adjusted by potentiometers.

- Providing the amplifier supply voltages by linear voltage regulators

- Biasing the temperature sensor with a small forward current. This is simply implemented by a $1\,\mathrm{M\Omega}$ resistor connected to a $5\,\mathrm{V}$ regulated voltage.

- Amplifying the detector signals by a factor of four. The outputs are provided to SMA connectors towards the DAQ.

- Generating the reset pulse. As the detector is operated in pulsed reset mode, a reset signal has to be sent to the CUBEs whenever the output voltage exceeds
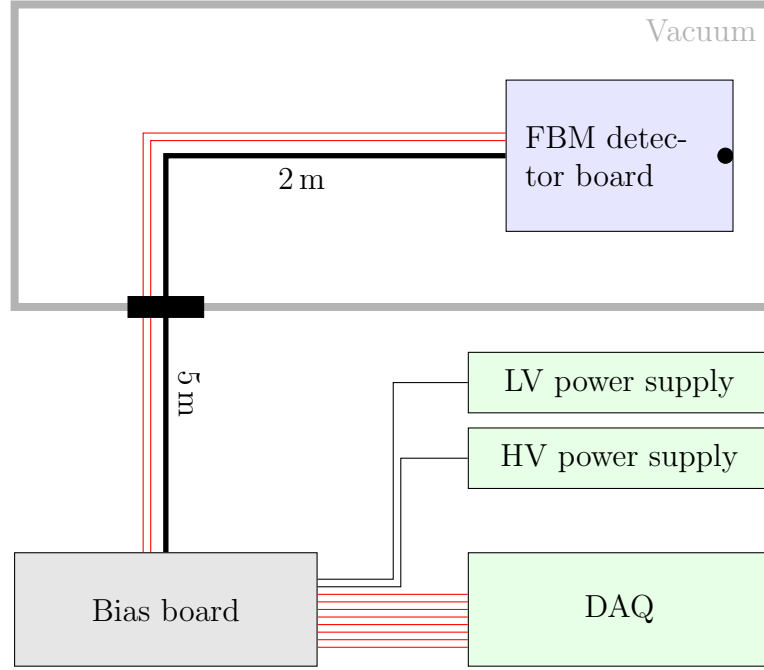
Figure 2.8.: Electric connections in the FBM setup. The red lines are coax cables and the thick black line is a cable with 18 wires.

> a certain voltage threshold. After detecting the need of reset by a comparator for each pixel, an OR logic generates a global reset pulse for all seven pixels simultaneously. This signal is provided to the CUBEs as well as to the DAQ, to track the precise time stamps of the resets.

The bias board was not developed for the FBM but was already used for many characterizations and measurements of the 7-pixel TRISTAN SDD prototypes. A photo of the used bias board is shown in the appendix figure A.2.

2.3. Geometry: Pad, Cover, Cables

The FBM detector is mounted on a manipulator inside the vacuum setup of KATRIN. This is a mechanical arm, which can control the position of the detector in x- and y-direction.

Pad The interface from the manipulator to the detector board where the SDD is mounted is a pad made from aluminium. The detector board and the cover are screwed onto the pad. As the bonds from the detector anodes to the CUBEs are on the bottom side, a recess is necessary in the pad around the detector (compare figure 2.10). The front part of the manipulator and the TRISTAN FBM detector are illustrated in figure 2.9.
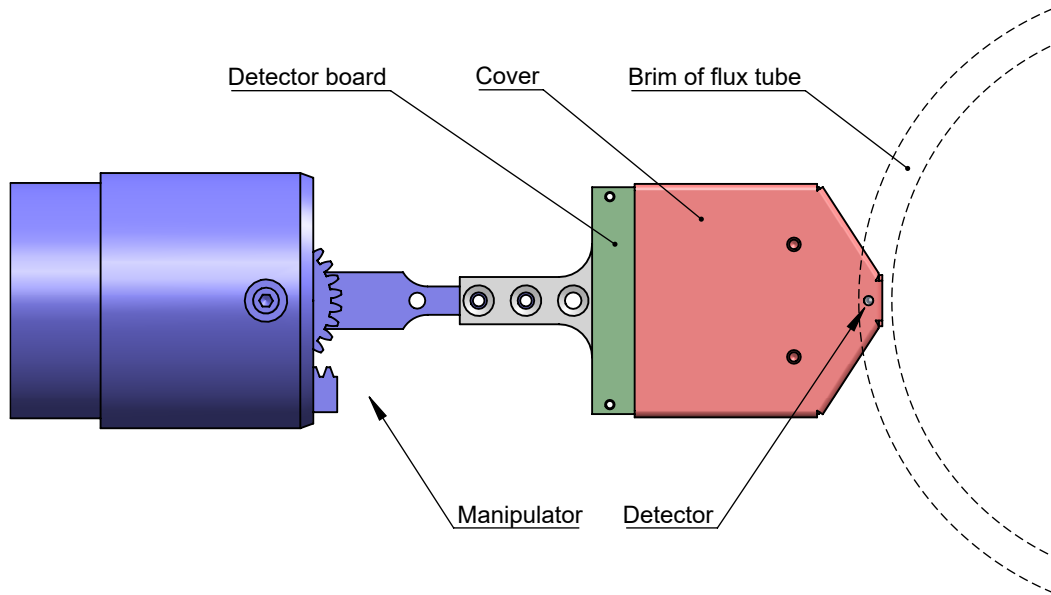
Figure 2.9.: CAD drawing of the front end of the TRISTAN FBM. The visible part of the detector board (green) is where the connector will be attached.
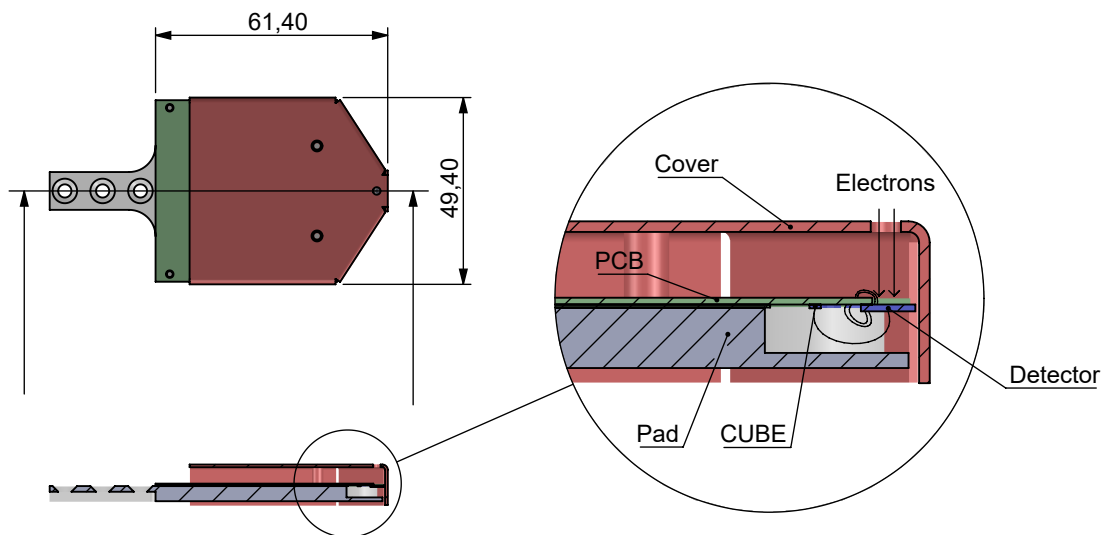

Figure 2.10.: CAD drawing of the TRISTAN FBM detector board, pad and cover. The bonds that connect the detector chip with the bias voltages and CUBE amplifiers on the detector PCB can be seen in the cross section drawing on the right.

Cover To shield the detector board electronics from the environment, and especially from the electrons in the flux tube, a cover is added above the detector board. The used material should have a high X-ray attenuation, as the incoming electrons will produce X-rays in this material. For light materials these X-rays may leave the cover and lead to an X-ray contribution in the detected spectrum or disturb the electronics. The produced X-rays have energies below 18 keV. For aluminum the attenuation length of X-rays in this energy range is up to 0.5 mm. For copper on the other hand the attenuation length in this X-ray energy range is below 2.9 μm [27] Therefore a copper sheet with a thickness of 0.7 mm was chosen. Another advantage of copper is the vacuum compatibility, as well as the good electrical properties.

2.4. Digitizers

The task of the DAQ system is to detect pulses in the analog signal of each pixel and determine their pulses height, which is correlated to the energy of the detected particle by the detector response.
The used DAQ for the TRISTAN FBM is based on full waveform digitization. The analog signal is digitized continuously with a high sampling rate and processed by a FPGA, which applies digital filters to the signal. For pulse height analysis a trapezoidal filter is used, which is described in the following section.

2.4.1. Pulse Height Analysis

An sketch of a typical digitized input signal is shown in the upper plot of figure 2.11. It consists of several pulses, and each pulse has an exponentially decaying tail. A pure pulsed reset signal has no decaying tail, but the DAQ system has a built-in AC-coupling with a time constant of 10 μs at each input, which removes the DC components from the signal.

Trapezoidal filter To determine the pulse height one applies a Finite Input Response (FIR) filter. Practically this means to convolve the time discrete input signal with a finite array of filter coefficients a_k. The coefficients a_k for a trapezoidal filter are shown in figure 2.12.

The filter consists of two main regions where the coefficients are non-zero: The first integrates over the samples after the rising edge of the pulse, and the second integrates over the samples before the rising edge of the pulse. The second integration window has a different sign than the first, therefore the filter output signal has the shape of a trapezoid, which height corresponds to the height of the input pulse (compare figure 2.11). The trapezoidal filter has 3 parameters: T_{shaping}, T_{gap} and $T_{\text{pole zero}}$:
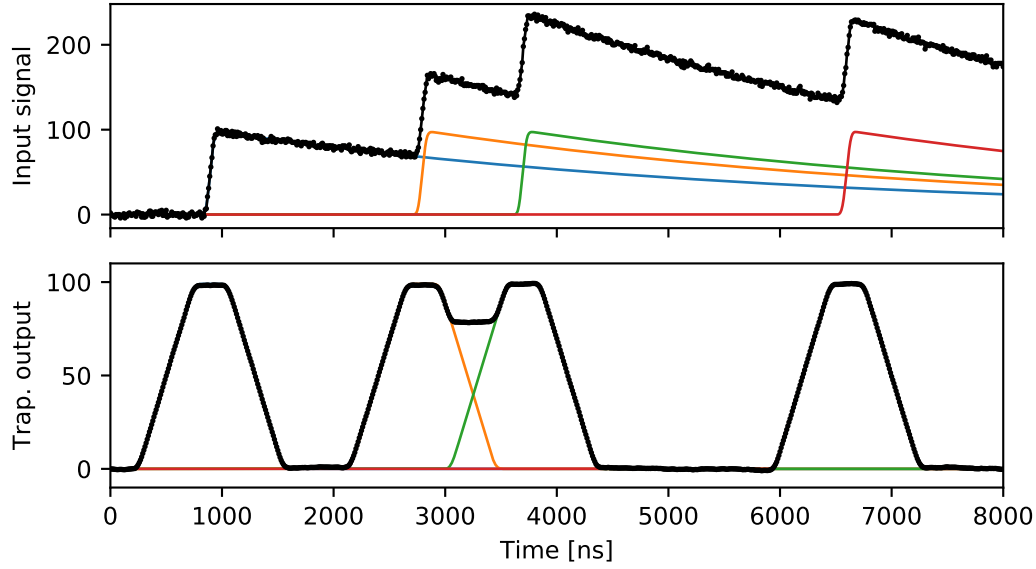
Figure 2.11.: Top: Sketch of a typical digitized input signal of the DAQ. The signal contains four pulses (shown in color) with an amplitude of 100 each. The resulting input signal (shown in black) is the sum of the individual pulses.
Bottom: Output of the trapezoidal filter. This is calculated by convolving the input signal shown in the top with the filter coefficients shown in figure 2.12. As a convolution is a linear operation this can also be seen as the sum of the trapezoidal filter outputs of the individual pulses.
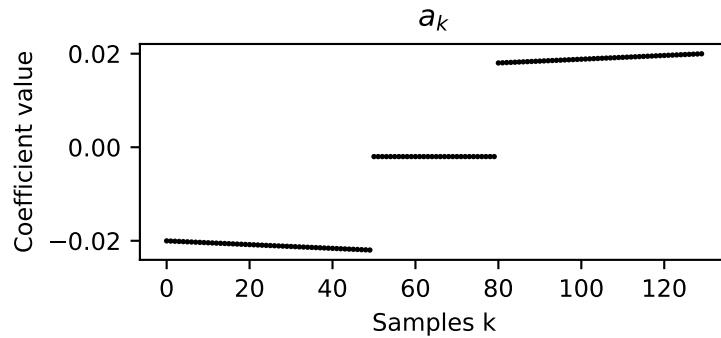
Figure 2.12.: The filter coefficients of a trapezoidal filter. In this case $T_{\text{shaping}} = 50$ samples and $T_{\text{gap}} = 30$ samples
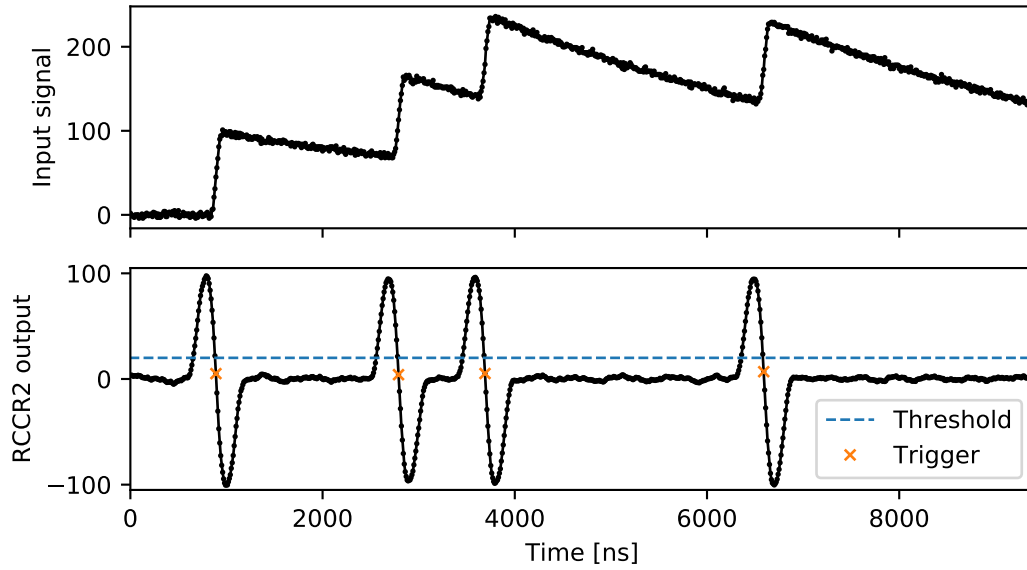
.

Figure 2.13.: The trigger filter (RCCR2) for the same input signal as in figure 2.11. The timestamps of the triggers (orange crosses) are determined by the first zero crossing after the threshold is exceeded.

$T_{\textbf{shaping}}$ The length of each of the two integration windows. This corresponds to the length of the rising edge of the trapezoidal output shown at the bottom of figure 2.11. Often this number is also called T_{rise} or T_{peaking}. This is can be qualitatively compared to the shaping time of a traditional analogue signal shaper.

$T_{\textbf{gap}}$ This is the length of the gap between the two integrating windows. The whole rising edge of a input pulse should fit into the gap. The samples within the gap are excluded, as the filter coefficients are zero.

$T_{\textbf{pole zero}}$ This parameter is the time constant of the decay of the pulses. The exponential decay can be taken into account in the filter, so that every waveform that exponentially decays to zero with the given time constant is giving an output of zero. This parameter leads to a small slope in the two integration windows in figure 2.12.

Timing and energy filters   The DAQ system feeds the input signal into two filters in parallel: One to determine the energy of a pulse, and another to determine the timestamp of a pulse. Typically the energy filter is a trapezoidal filter with a long shaping time, as this averages white noise on the waveform to give a good energy resolution. The timing filter on the other hand has a short time constant, and therefore is optimal to precisely determine when the rising edge of a pulse.
The DAQ processes an event by the following procedure: As soon as the timing filter triggers an events at a certain timestamp, the energy filter is evaluated at the corre-
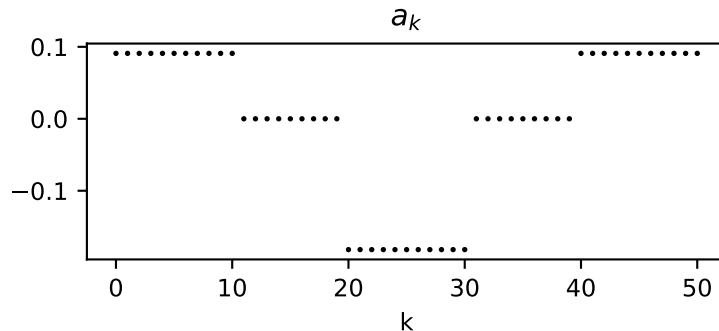
Figure 2.14.: The filter coefficients of a RCCR2 timing filter. In this case the everaging window is $T_{av} = 10$ samples and the time constant for the double differentiation is $T_{diff} = 20$ samples.

sponding position. The event is then saved as a tuple of time stamp and energy into the RAM.

2.4.2. Used DAQ Systems

CAEN system The main DAQ system used for the TRISTAN FBM is the CAEN v1781 card. It is a 8 channel, 100 Msps digitizer. For each channel a pulse height analysis as described above is performed on-board on FPGAs. The card uses a trapezoidal energy filter and a so-called RCCR2 timing filter: This filter gives a bipolar output for a pulse, as illustrated in figure 2.13 and 2.14. After the filter exceeds a certain threshold, the time stamp is determined by the next zero crossing of the filter. This corresponds to the point where the rising edge in the input signal is the steepest, and therefore is independent of the pulse height. The energy filter also provides a baseline reconstruction and other additional features. The card has a 2U wide VME form factor, which means that a VME crate is needed for power supply. The communication to the PC is realized by an optical fiber. This has the advantage of being electrically not coupled to the PC and provides a high data throughput rate of up to 80 MB/s. The BNC signal inputs have a high impedance ($1\,\mathrm{k\Omega}$) and an AC-coupling with a time constant of $10\,\mathrm{\mu s}$. With the used setting the 32k ADC bins are mapped to a 500 mV input dynamic range, leading to 15 µV per ADC least significant bit (lsb).

DANTE system For some of the first measurements with the TRISTAN FBM the DANTE box produced by XGlab was used. This box was also used for previous measurements with the TRISTAN prototype SDD detectors. The DANTE box is also a 8 channel digitizer with 125 Msps sampling rate. The onboard FPGA applies a trapezoidal energy filter and, different than CAEN, a trapezoidal timing filter. In this case the time stamp of a pulse is defined when a fast trapezoidal filters output crosses a cer-

tain threshold. One has to be aware that in this case the times tamp depends slightly on the energy of the pulse. The input is not AC coupled, so that the whole ramp is seen in the digitized signal. Further details about full waveform digitizing DAQs and especially the DANTE box can be found in [28].

3. Characterization of the TRISTAN FBM Detector

Several measurements were performed before the final installation of the TRISTAN FBM detector in the KATRIN beam line. The main results of these characterization measurements are described in the following.

3.1. Temperature Calibration

There are several temperature dependent effects in a silicon detector. For example, the noise component introduced by the leakage current of the detector depends on temperature, with the leakage current doubling roughly every $10\,\mathrm{K}$. Furthermore, the gain of the preamplifiers can be temperature dependent. While the effect of the leakage current is suppressed for the FBM detector due to its small size, a stable gain of the preamplifiers is very important: As the FBM has to define a cut for integrating the count rate in the spectrum, a change in the gain is reflected in the measured rate. Therefore, it is important to monitor the temperature, and to operate the detector at a stable temperature.

The temperature of the operating TRISTAN FBM is expected to be around $-15\,°\mathrm{C}$, as this is the temperature observed on the previous detector installed at the setup [16]. There is no active cooling or control of the temperature. The temperature is defined by radiative coupling to the cold CPS environment (ca. $80\,\mathrm{K}$) and the thermal conductance in the long stainless steel arm where the FBM is mounted, which is at room temperature on the far end.
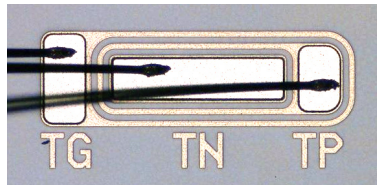

Figure 3.1.: Microscopic picture of the temperature sensor. The p- and n-type silicon of the diode is labeled *TP* and *TN* respectively. There is an additional guard around the diode labeled *TG*.
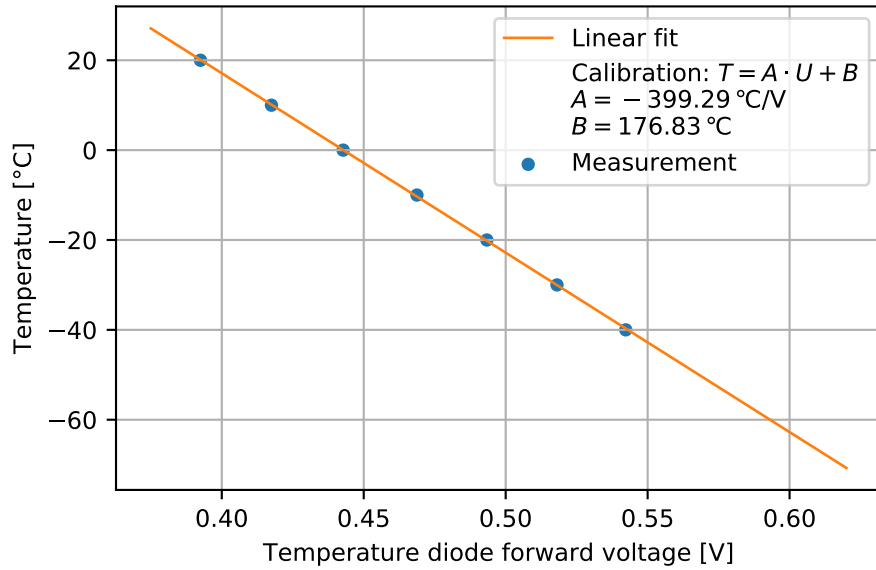
Figure 3.2.: Temperature calibration of the temperature diode on the TRISTAN FBM detector chip. The resulting slope of the diode voltage is $-2.5\,\mathrm{mV/K}$

.

The TRISTAN FBM detector is equipped with a temperature sensor directly on the SDD silicon chip. The sensor is implemented as a diode, which is biased with a small forward current of $5\,\mu\mathrm{A}$. The forward voltage of the diode depends on the temperature with a linear relation with a slope of about $-2\,\mathrm{mV\,K^{-1}}$ [29]. The exact parameters of the linear dependence are determined by a calibration measurement, shown in figure 3.2. The systematic uncertainty of the temperature calibration is estimated to $\pm3\,\mathrm{K}$, which is sufficient for the FBM.

3.2. Characterization with X-rays and Electrons

Several measurements were performed with radioactive sources at a test bench in the TRISTAN laboratory at MPP in order to characterize the detector. The length and type of the cables was chosen similar to the setup at KATRIN where the FBM will finally be installed. This resulted in $2\,\mathrm{m}$ of cable in vacuum and another $3\,\mathrm{m}^1$ of cable after a feed through until the bias board is reached. The detector voltages which were provided by the bias board are stated in table 3.1. The used DAQ system was the DANTE box, the settings can be found in table 3.2. This section focuses on a measurement with a ^{83m}Kr source, emitting together X-rays and mono-energetic electrons.

---

^{1}This was only a guess. It turned out that the FBM setup has $5\,\mathrm{m}$ of cable length outside vacuum (see figure 2.8).

3.2.1. Krypton Calibration Source

To characterize the detector response to electrons, conversion electrons from a ^{83m}Kr source were used. The source has a substrate of rigid graphite on which a small amount of ^{83}Rb is evaporated. ^{83}Rb serves as a generator for ^{83m}Kr, as ^{83}Rb decays with a half-live of 86 d by electron capture to ^{83m}Kr. 500 keV γ-rays are produced by that process. This ^{83m}Kr is an isomeric state which decays by a cascade of two low energy transitions (32.2 keV and 9.4 keV) with a high conversion coefficient. The half live of ^{83m}Kr is 1.82 h. One challenge is that the gaseous krypton will often leave the graphite substrate before it decays, however a sufficient fraction decays still in place [30].
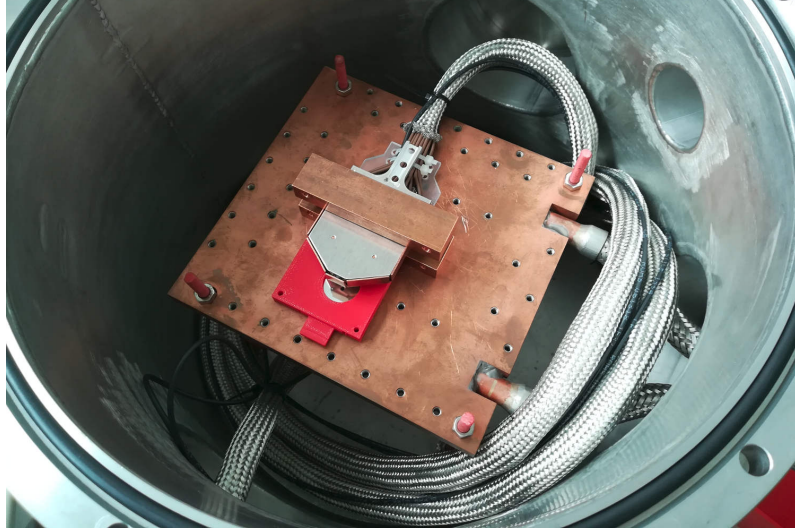

Figure 3.3.: Setup for the measurement in the MPP laboratory. The 2 m of cable inside vacuum are rolled up in the vacuum chamber. The source (in this case ^{55}Fe) is place below the detector. This way the chance for dust to deposit on the entrance window is decreased.

Table 3.1.: Detector voltages at the MPP teststand

$V_{\mathrm{BC}} =$	$-89.7\,\mathrm{V}$
$V_{\mathrm{BF}} =$	$-99.5\,\mathrm{V}$
$V_{\mathrm{R1}} =$	$-20.0\,\mathrm{V}$
$V_{\mathrm{RX}} =$	$-26.0\,\mathrm{V}$

Table 3.2.: DANE DAQ settings used in the krypton measurement

Energy filter	$T_{\mathrm{shaping}} =$	$1014\,\mathrm{ns}$
	$T_{\mathrm{gap}} =$	$320\,\mathrm{ns}$
Fast filter	$T_{\mathrm{shaping}} =$	$160\,\mathrm{ns}$
	$T_{\mathrm{gap}} =$	$80\,\mathrm{ns}$

3.2.2. Measured Spectrum

The count rated in the measurement with the krypton source was about $50\,\mathrm{cps}$ per pixel and the duration of the measurement was $12\,\mathrm{h}$. The measurement was performed at a vacuum lower than $10^{-4}\,\mathrm{mbar}$ and distance between the SDD and the krypton source was about $1\,\mathrm{cm}$, so that the scattering of electrons in the remaining gas can be neglected.

Table 3.3.: X-ray lines of krypton, used for calibration. Only the lines contributing to the main peaks of K_α and K_β are listed. Values taken from [31].

Line	Position	Intensity	Weighted mean position
$K_{\alpha 1}$	$12\,648\,\mathrm{eV}$	$34\,\%$	$12\,630\,\mathrm{eV}$
$K_{\alpha 2}$	$12\,595\,\mathrm{eV}$	$66\,\%$	
$K_{\beta 1}$	$14\,113\,\mathrm{eV}$	$66\,\%$	$14\,110\,\mathrm{eV}$
$K_{\beta 3}$	$14\,105\,\mathrm{eV}$	$34\,\%$	
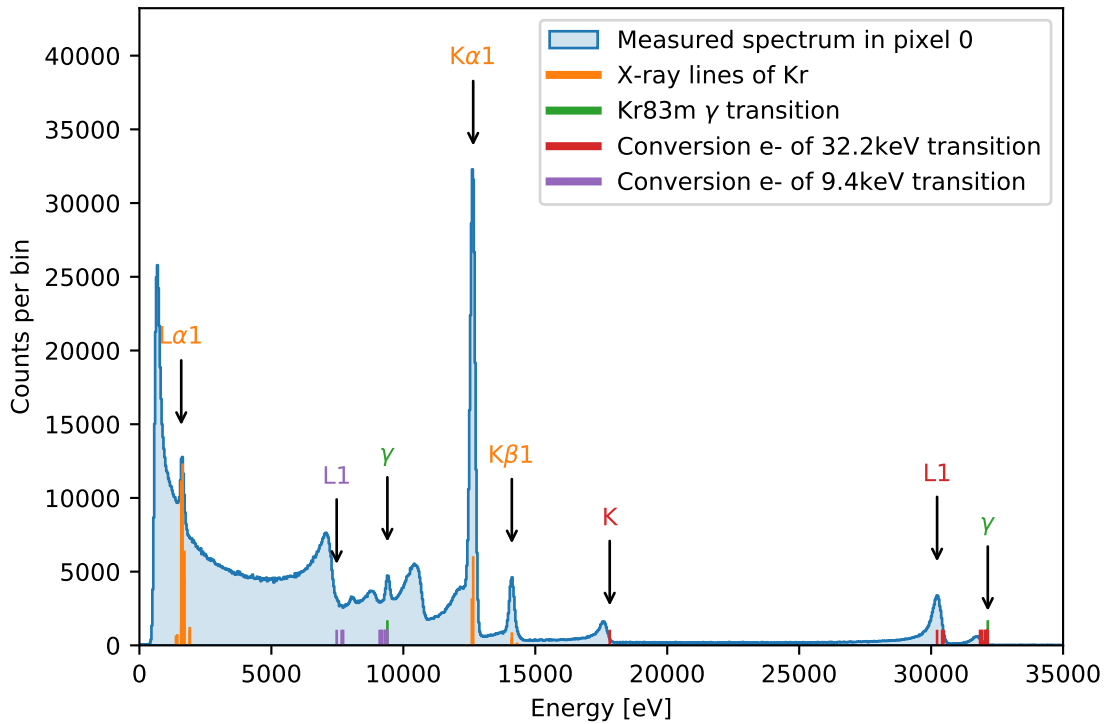
Figure 3.4.: Measured spectrum of the krypton source which contains photon and electron peaks. The intensities of the X-ray lines plotted for comparison should only show the order of magnitude of the line. For the conversion electron and γ lines only the positions are shown for comparison.
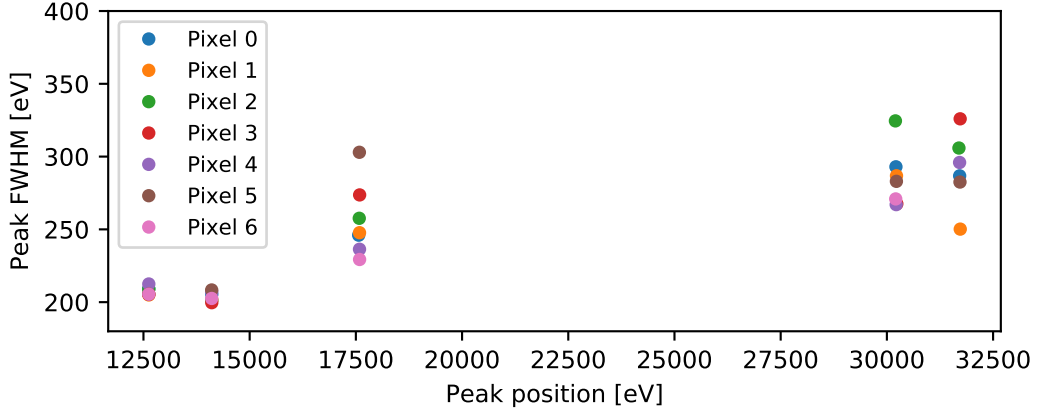
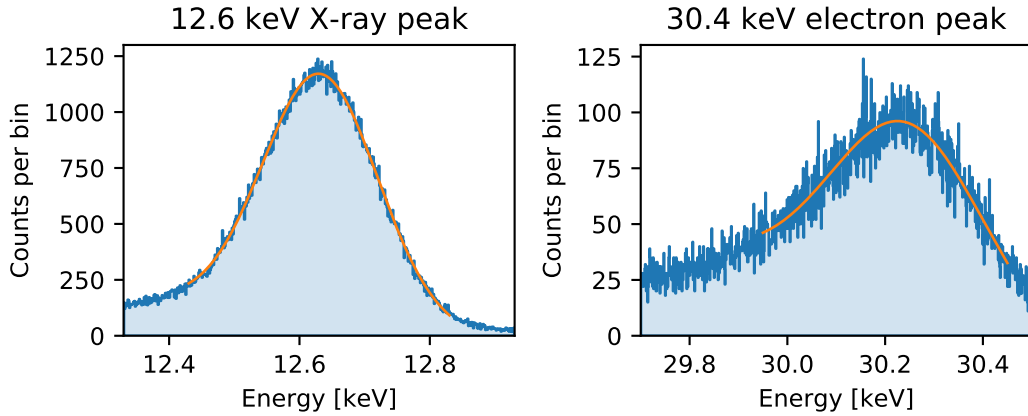**Figure 3.5.:** Fitted FWHM for peaks in the krypton spectrum. A simple Gaussian model was used.

Figure 3.6.: Zoom to the K_α X-ray peak (left) and electron peak from L conversion of the 32 keV transition. The peaks are both fitted with a Gaussian allowing a linear background.

To calibrate the spectra the two most intense X-ray peaks were used, which are the K_α and K_β peaks of krypton. The X-ray lines contributing significantly to the fitted peaks are listed in table 3.3. For calibration the weighted mean positions are used, as the individual lines cannot be resolved with the detector resolution of around 200 eV. The calibrated spectrum measured in the central pixel is shown in figure 3.4. In addition to the mono-energetic electron and γ lines from the decay there are several X-ray lines and also Auger electrons present in the spectrum.

The FWHM of different peaks in the spectrum is shown in figure 3.5. For X-ray peaks the FWHM is lower than 220 eV, which is close to the Fano resolution of 170 eV at 12.6 keV. The width of electron peaks is expected to be larger compared to X-rays,

due to the effect of the entrance window of the detector. In the measurement a FWHM lower than 350 eV is observed for the electron peaks. Figure 3.6 shows a comparison of an X-ray and an electron peak. The electron peak is widened and shifted with respect to its line position due to the effect of the dead layer [17]. For the same reason the electron peaks are also less symmetric than the X-ray peaks.

The peaks in the spectrum have tails towards lower energies. For electron peaks the effects of back scattering and the dead layer contribute to this tail, where only part of the electrons energy is deposit in the sensitive volume of the detector. The main contribution to the tail comes from charge sharing happening at the pixel border, which effects electrons and X-rays. The effect of charge sharing will be discussed in detail in section 3.3. In the measurement an energy threshold lower than 1 keV was achieved on all pixels.

3.2.3. Waveforms

Waveforms of events from each pixels are shown in figure 3.7. The rising edge is shorter than 100 ns. The signals of pixels 0 and 6, which have coax lines, can clearly be distinguished from the other pixels without coax lines. On these non-coax pixels an overshoot, probably caused by the improper termination of the long lines, is observed. This overshoot is not very critical for the energy determination of the pulse, if the gap time of the applied trapezoidal filter is long enough to cover the overshoot. For the FBM a gap time of 300 ns is chosen, which should lead to very little influence of the overshoot.

3.2.4. Noise Performance

An important characteristic of a silicon detector is its **noise curve**. It describes how the energy resolution of the detector depends on the shaping time of the used filter for the pulse height determination. To calculate the noise curve, one can repeat the same measurement with different shaping times, and evaluate the FWHM of a certain peak in the received spectrum. Alternatively the digitized waveforms of each pulse can be saved, so that the pulse height determination can be done offline with any filter setting. This second approach was done for the Krypton measurement.

The shape of the curve is influenced by different contributions:

- The **serial noise** on the waveform is noise with a flat power spectral density. This noise is independent on each digitized sample so that by averaging one gets $\sigma_{\text{serial noise}} \propto \frac{1}{\sqrt{N_{\text{average}}}}$. This leads to a straight line with negative slope in the double logarithmic plotted noise curve.

- The **pink noise** has a power spectral density $\propto f^{-1}$. This leads to a amplitude $\propto \sqrt{f^{-1}}$. Together with the averaging of the filter one gets a flat contribution

independent of the shaping time. Many electronic components add some pink noise to the waveform, for example the effect of capture and release of charge in a FET.

- The **Fano noise** is the contribution of the statistical process of charge creation in the silicon detector. As it describes the amount of created charge in the detector, it does not depend on the shaping time. This means it also has a flat contribution in the noise curve.

- Usually there is another component, often called **parallel noise**. In the double logarithmic noise curve plot this usually leads to a line with positive slope, meaning that long shaping times lead to worse energy resolution. This is caused by the leakage current of the detector diode, and is therefore very suppressed by the small area of the FBM detector. It is not visible in the measured noise curve.

The FWHM of these effects can be added in quadrature to get a combined FWHM which can be compared to the measurement, as shown in figure 3.8. To optimize shaping time for the FBM detector, not only the energy resolution is relevant, but also the effect of pile-up should be minimized, for which short shaping times are preferable. The count rate for the FBM is in the order of 50 kcps, where pile up will have a very relevant effect on the measured spectrum. Considering both energy resolution and pile-up, an optimal shaping time of 300 ns was determined. In this case the 12.6 keV X-ray resolu-
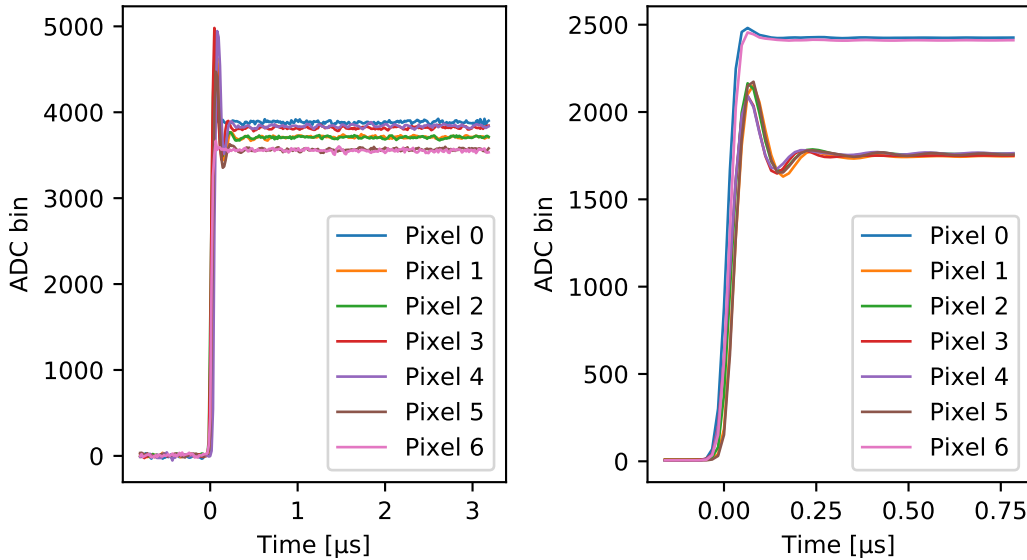

Figure 3.7.: Left: Waveforms of pulses captured with the krypton setup. The pulses correspond to the 30 keV peak in the spectrum.
Right: Zoom into the rising edge. To get rid of noise on the waveform a lot of pulses from the spectrum are averaged. The amplitude of the shown pulses is an artifact of the chosen pulses for averaging and is not of interest.
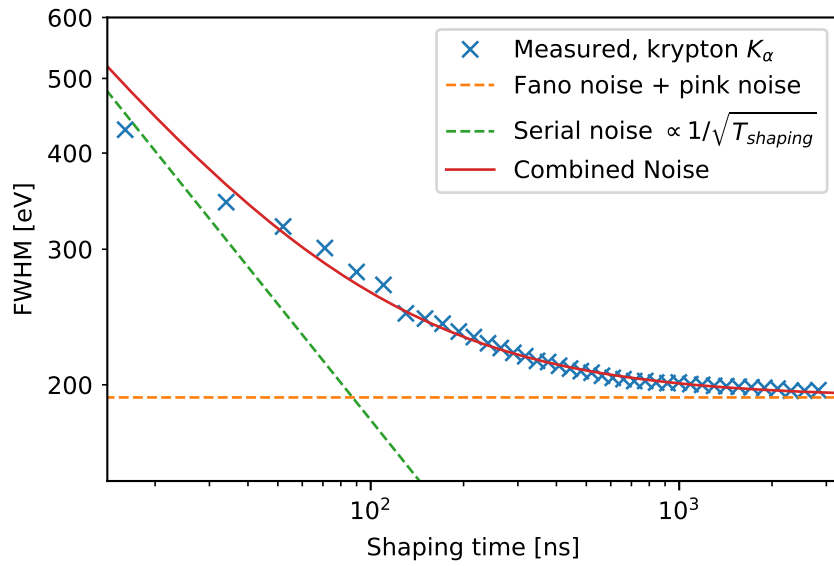
Figure 3.8.: Noise curve of the $12.6\,\mathrm{keV}$ K_α X-ray peak of Krypton. The trapezoidal gap time is fixed to $T_{\mathrm{gap}} = 320\,\mathrm{ns}$. The shown data points belong to the pixel 0 of the FBM. The slightly smaller energy resolution at very low shaping times compared to the serial noise expectation can be explained by the input bandwidth of the amplifiers and the DAQ.
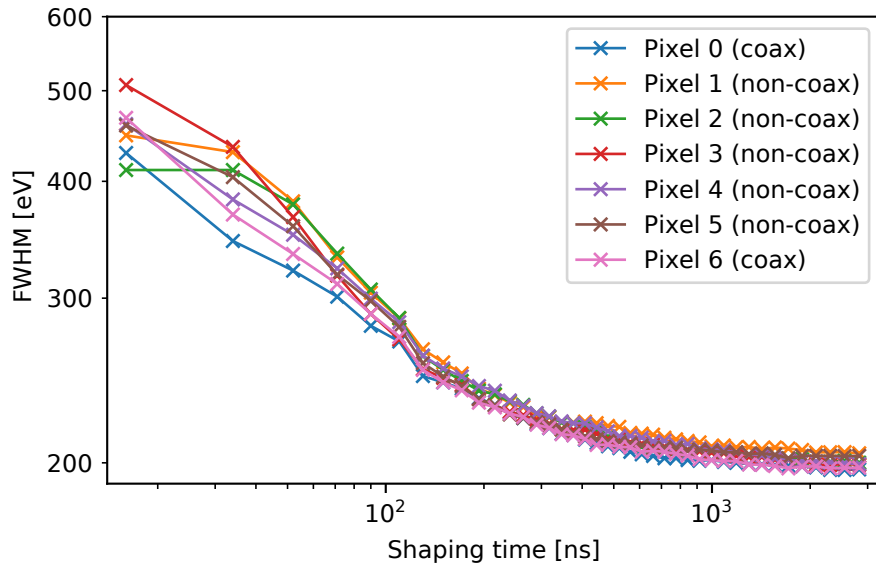

Figure 3.9.: Comparison of the noise curves as shown in figure 3.8 of all the seven pixels.

tion is around $220\,\text{eV}$, consisting $170\,\text{eV}$ from Fano noise and $140\,\text{eV}$ from electronics noise added in quadrature. This corresponds to a ENC_rms[2] of around $16\,$electrons.

The noise curves for all seven pixels are shown in figure 3.9. The curves look similar, despite the fact that only two of them are operated with coaxial cables. The overshoot observed in the waveforms has no significant influence to the energy resolution.

3.3. Charge Sharing

A very important effect that influences the detector response of the TRISTAN FBM detector is the so-called charge sharing. Compared to the "standard" TRISTAN detectors, which have diameters of $2\,\text{mm}$ to $3\,\text{mm}$ this effect is strongly enhanced by the small size of the FBM detector.
Multi-pixel detectors have no physical borders between pixels. One pixel is only defined by the region where the created charge is collected by one anode. If an event happens in the middle of two anodes, its charge cloud is shared between two pixels. In this case both anodes trigger an event with a fraction of the initial amount of charge. The number of pixels (or anodes) which share the charge of an event is called the multiplicity of the event (see figure 3.10).

3.3.1. A Simplified Model

To estimate the expected amount of charge sharing, a model is necessary, that gives the probability to split the charge of an event by a certain fraction at the border of the pixel.

For this model, a simplified geometry of the region close to the border between two pixels A and B is considered, as shown in figure 3.11. For every event the fraction η of
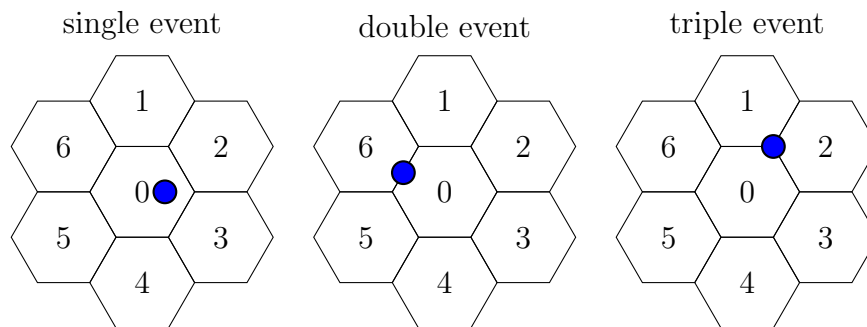

Figure 3.10.: Three different possibilities of multiplicity of an event. The charge cloud (blue) can be split between one, two or three pixels.
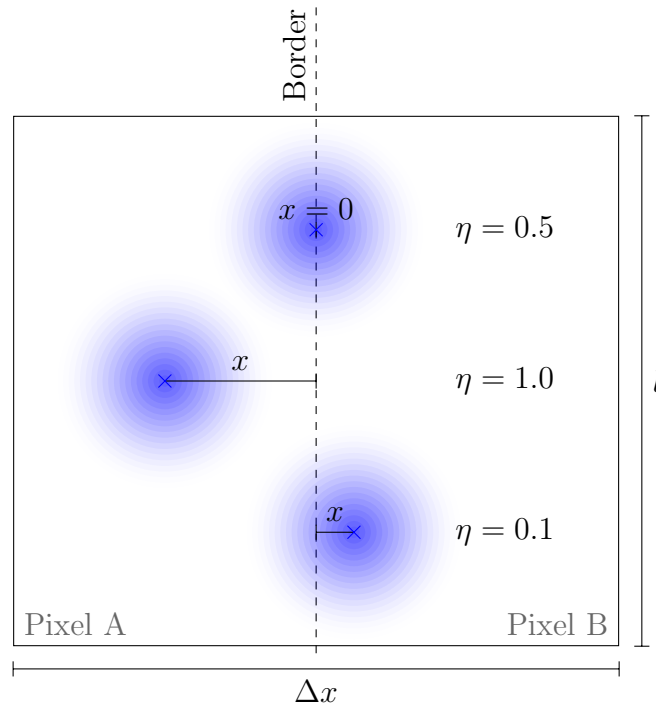
---

[2]Equivalent Noise Charge

Figure 3.11.: Sketch of the geometry for the charge sharing model. Three exemplary events (blue crosses) are assumed with different interaction coordinates x relative to the border. η is the relative amount of charge in pixel A.
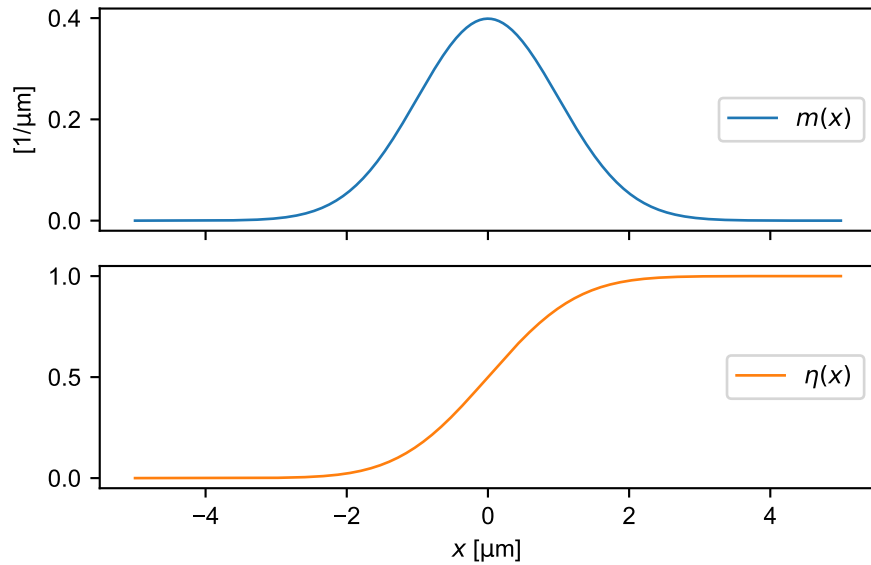

Figure 3.12.: Exemplary Gaussian charge cloud density function $m(x)$ with a width $w = 1\,\mu\text{m}$. The fraction of charge η which reaches pixel A is the integral of $m(x)$.

charge that is collected by pixel A is defined by

$$\eta = \frac{Q_A}{Q_A + Q_B},$$ (3.1)

where Q_A and Q_B are the charges in the pixels A and B respectively. To calculate η the coordinate x of the event relative to the border and the one-dimensional charge cloud density profile $m(x')$ has to be known. η is then obtained by integrating over the x' coordinate

$$\eta(x) = \frac{Q_A}{Q_A + Q_B} = \int_{-\infty}^{x} m(x')\,\mathrm{d}x'.$$ (3.2)

In figure 3.12 $m(x')$ and $\eta(x)$ are plotted for a Gaussian charge cloud density profile.

The aim of the model is to predict the probability density function (PDF) of η, called $P(\eta)$. As η is a function of the interaction coordinate x, the PDF of x, called $P(x)$, has to be known. If a homogeneous illumination of the area is assumed, the distribution of x is flat

$$P(x) = \frac{1}{\Delta x}.$$ (3.3)

Now, a variable transform from x to η can be applied:

$$P(\eta) = P(x) \cdot \frac{\mathrm{d}x}{\mathrm{d}\eta}$$ (3.4)

To calculate this, $\frac{\mathrm{d}x}{\mathrm{d}\eta}$ is needed at a certain η, which can be calculated numerically from equation 3.2. For a Gaussian charge cloud density profile with width w the PDF of η becomes

$$P(\eta) = \frac{w}{\Delta x} \cdot \frac{1}{g(\eta)}$$ (3.5)

where $g(\eta)$ is a numerically calculated function independent of w. The shape of $\frac{1}{g(\eta)} = P(\eta)\frac{\Delta x}{w}$ is plotted in figure 3.13. Up to now $P(\eta)$ is normalized to one incoming event
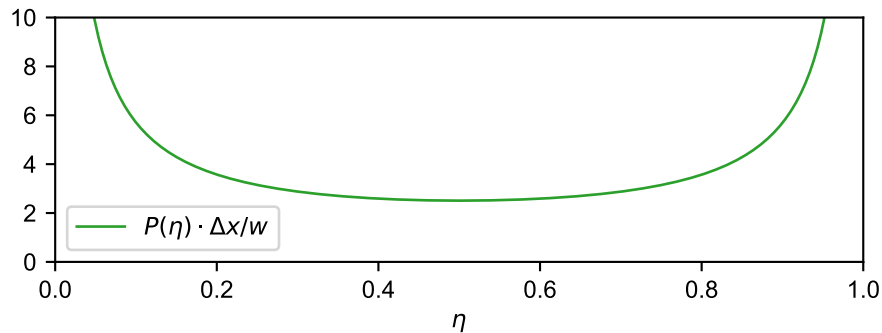

Figure 3.13.: Probability density function for the fraction of charge accumulated in one pixel. This curve assumes a Gaussian charge cloud density profile with a width w and a flat distribution of the interaction position with width Δx.

in the area shown in figure 3.11. If one incoming event is assumed within one detector pixel, Δx can be replaced by $\frac{A}{l}$, where A is the area of the pixel and l the total length of the pixel border. This is only valid if the pixel radius is big compared to the width of the charge cloud w, otherwise $P(x)$ is not flat anymore. Assuming this is the case, the PDF for η is

$$P(\eta) = \frac{wl}{A} \cdot \frac{1}{g(\eta)}. \tag{3.6}$$

This probability for charge sharing scales with the size of the charge cloud w and the fraction of the pixel border to pixel area $\frac{l}{A}$, as expected.

3.3.2. Charge Sharing in the Krypton Measurement

With the help of the krypton calibration source, charge sharing could be investigated for X-ray and electron signals. To this end all events in the measurement are categorized by their multiplicity. The time interval to detect the multiplicity was chosen to be 200 ns. Figure 3.14 shows the number of single and double events in the detector. Single events are associated to the pixel where they happened, double events are associate to the border between the two pixels where the two events happened. As the number of triple events is low, they are discarded in this analysis. 34 % of all events that were detected in the central pixel were charge sharing events. The energy threshold, which has an influence on the number of detected charge sharing events, was 800 eV in the measurement.

On the border areas in figure 3.14 not only charge sharing events are present. There
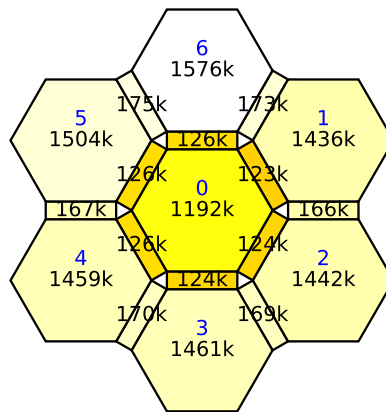

Figure 3.14.: Number of single and double events in the krypton measurement. The color corresponds to the event density in each area. The width of the border, where events with multiplicity two happen, is set to 30 μm.

are also events that happen by coincidence in the two pixels, but are really two physical events. These events are called random coincident events in the following. The expected number N_{AB} of random coincident events between the pixels A and B can be estimated to

$$N_{AB} = \frac{2 \cdot N_A \cdot N_B}{T} \cdot 200 \, \text{ns}, \tag{3.7}$$

where N_A and N_B are the total number of events in the two pixels, T is the live time of the measurement and 200 ns corresponds to the time window for coincidence detection. Plugging in the numbers, the expected number of random coincident events between two pixels is $N_{AB} \approx 44$. This small number of random coincidence events can be neglected compared to the number of charge sharing events, which is $\mathcal{O}(10^5)$.

The energy distribution of the double events is plotted in figure 3.15. As expected, there are clearly visible diagonal lines in the histogram, where the energy of the events in pixels A and B sum up to the physical energy of a line in the spectrum. Within each line of the histogram a structure is visible: There are more events towards both ends of the line. The position on each line corresponds to the fraction $\eta = \frac{E_A}{E_A + E_B}$, which is zero on the upper left (all energy in pixel B) and one at the lower right (all energy in pixel A). For each line, a histogram of η can be drawn. Figure 3.16 shows this histogram of η for the krypton K_α line.

This measured distribution of η is now compared to the expected distribution, that was obtained from the simplified model in section 3.3.1. In figure 3.16, the expectation from equation 3.6 is plotted, where A and l were plugged in for the FBM pixel geometry. The only free parameter is w. For $w = 15.5 \, \mu\text{m}$ the expected distribution of η agrees very well with the measured distribution of η for the K_α line. This implies, that the Gaussian shaped charge cloud, that was used to derive the model, is a valid assumption. The Gaussian shape of the charge cloud has a physical motivation: If a small charge cloud is created in the detector by ionization due to the incoming particle, diffusion over time will lead to a Gaussian charge cloud with width

$$\sigma = \sqrt{2Dt}, \tag{3.8}$$

were t is the time and D is the diffusion constant. For silicon near room temperature D is $6831 \, \text{mm}^2 \, \text{s}^{-1}$ [22]. Within an estimated drift time of 20 ns the charge cloud has a size of around $\sigma = 12 \, \mu\text{m}$. This is in the same order of magnitude as the measured $15.5 \, \mu\text{m}$ for events of around 12.6 keV energy.

The same procedure was also applied to the whole range of energies in the spectrum. The resulting charge could sizes are shown in figure 3.17. The width w is close to $20 \, \mu\text{m}$ for most energies. There are two interesting features:

1. The K_α and K_β lines both have smaller widths. This can be related to the depth of interaction in the detector: Electrons and low energetic photons interact very close to the entrance window of the SDD. Therefore the charge cloud always has the same time to diffuse until it reaches the saddle point between pixels. With higher energy, photons start to penetrate the SDD deeper. In this case there is
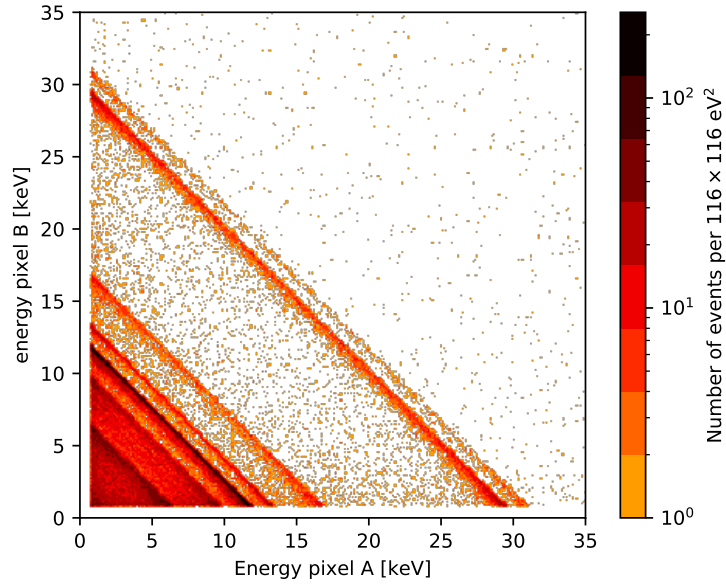
Figure 3.15.: Histogram of the two observed energies of double events. For this plot all double events in the 12 h krypton measurement were used.
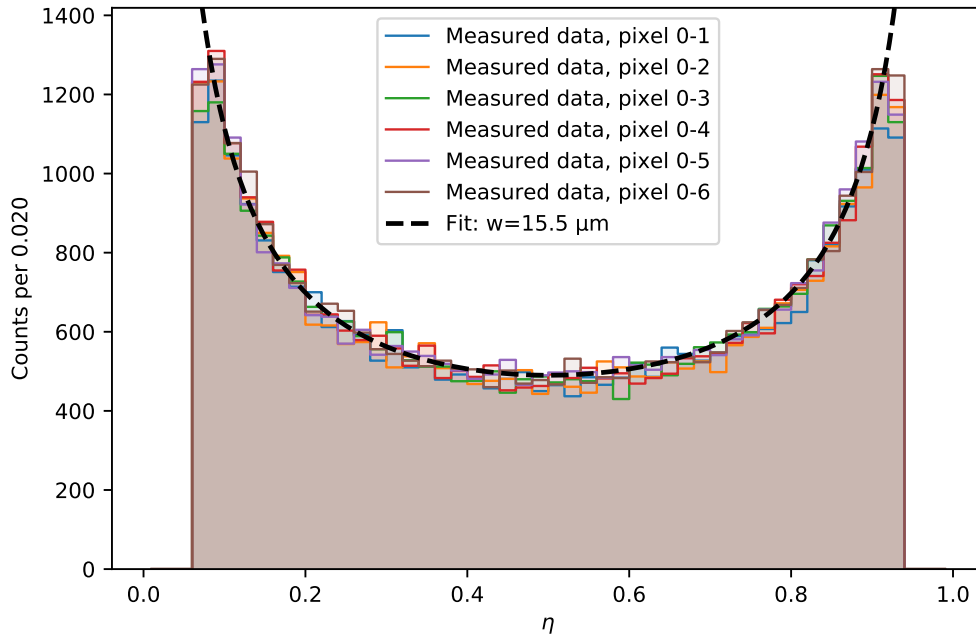

Figure 3.16.: Histogram of η for the six neighboring pixel regions of the central pixel. The event energy region of interest is around the K_α line at (12.6 ± 0.5) keV.
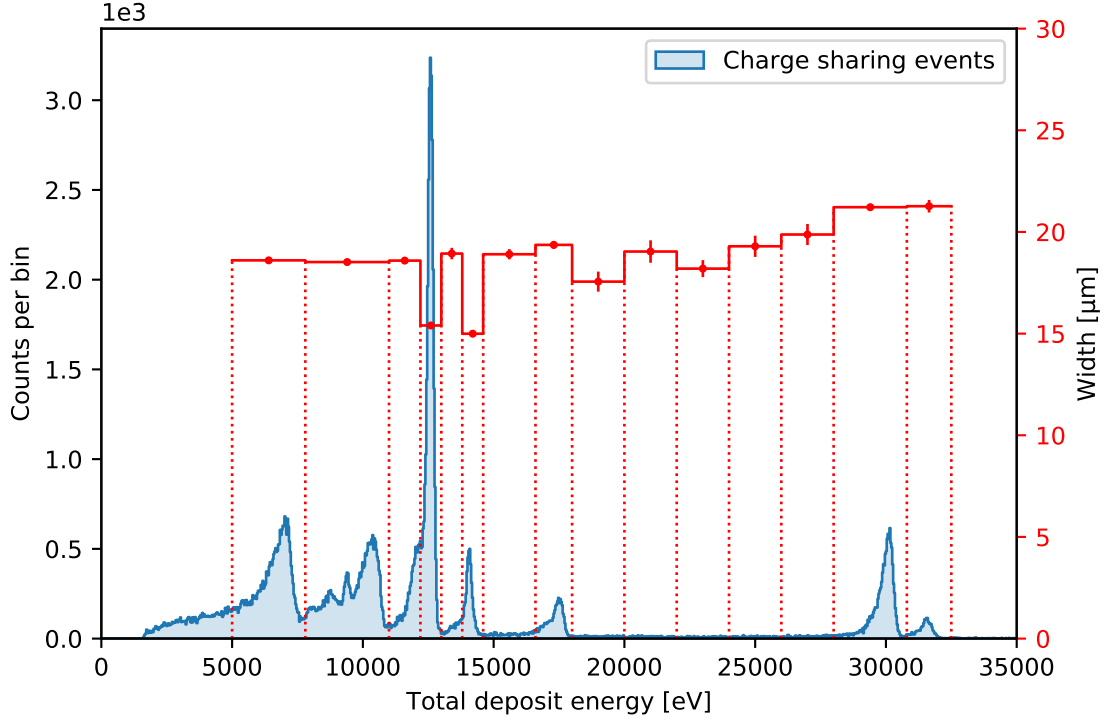
Figure 3.17.: The best fit width (red) of the Gaussian charge cloud density profile for different energy regions of interest. The blue spectrum shows the total energy of the charge sharing events, which is the sum of the energies of the two participating pixels.

less time for the drifting charge cloud to reach the saddle point and the charge cloud is smaller. This effect is illustrated in figure 3.18. According to this plot the mean width of K_α and K_β X-rays is lowered by about 25 % compared to electrons. This fits to the measured K_α and K_β charge cloud widths in figure 3.17, where the surrounding regions are assumed to be electron events.

2. All events above 15 keV are electron events. The width of these events is expected to increase slightly with energy, as a bigger charge cloud is created at higher energies. This effect is small, as the primary electron rarely travels more than 4 μm [18] and the width is dominated by diffusion. Electrostatic repulsion can also contribute to the size of the charge cloud. This effect is also energy dependent, and is expected to be small for charge clouds containing less than $\mathcal{O}(10^4)$ electrons [32].

Conclusion The new TRISTAN FBM detector system was tested successfully in the MPP laboratory. A very good energy resolution of less than 350 eV for electrons was observed on all seven pixels, regardless if a coax line or a non shielded wire is used for the signal transmission. In the laboratory environment, an energy threshold of 0.8 keV was achieved. Furthermore a simplified model for charge sharing events was

introduced. This model explains the amount and energy distribution of charge sharing events, by assuming the Gaussian shaped charge cloud due to diffusion during the drift in the detector.
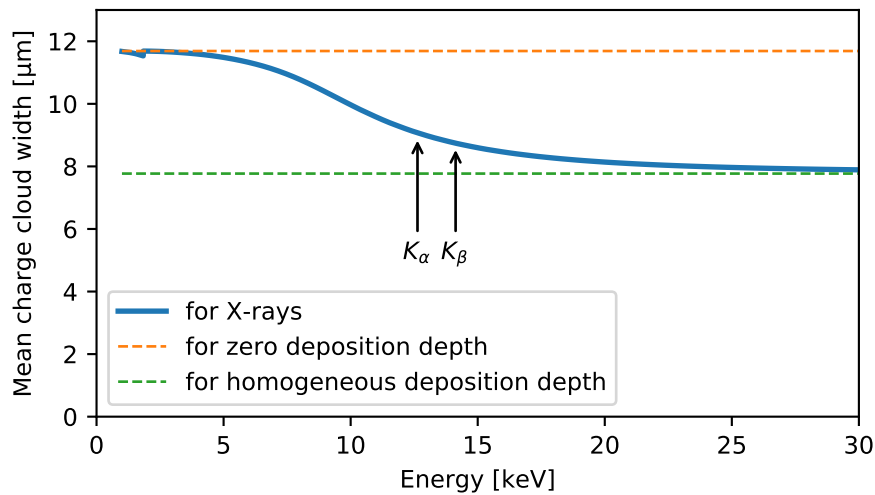

Figure 3.18.: Mean width of the charge cloud by diffusion. The distribution of deposition depths is calculated as exponential distribution with attenuation constant from the NIST database [27]. For each depth, the drift time is determined assuming a drift with constant velocity to the anode side of the detector. With this distribution of drift times the diffusion widths can be calculated with equation 3.8. As electrons do not penetrate the detector significantly they correspond to the orange dotted line. X-ray with energies above 20 keV have a low chance to get detected at all in 450 μm of silicon, the distribution of interaction depths is flat in this case. This limit of homogeneous illumination is shown by the green dotted line.

4. Implementation and Commissioning

In July 2019 the TRISTAN FBM detector was installed at its final place of use in the KATRIN experiment. The following chapter will first summarize the procedure of installation and will give an overview of the technical implementation of the software.

Finally, the first results of the calibration measurements prior to the rate-monitoring during the neutrino mass campaign are presented.

4.1. Installation in the KATRIN Beamline

The installation includes the components shown in figure 2.8. Besides the detector itself two power supplies as well as a VME crate holding the DAQ card and an aluminim box holding the bias board were installed.

To exchange the FBM detector the vacuum system of KATRIN had to be opened. When the detector is at parking position a valve towards the beam line can be closed to separate the FBM vacuum chamber from the KATRIN vacuum chamber. After venting the FBM vacuum chamber the flange at the 6-way cross at parking position can
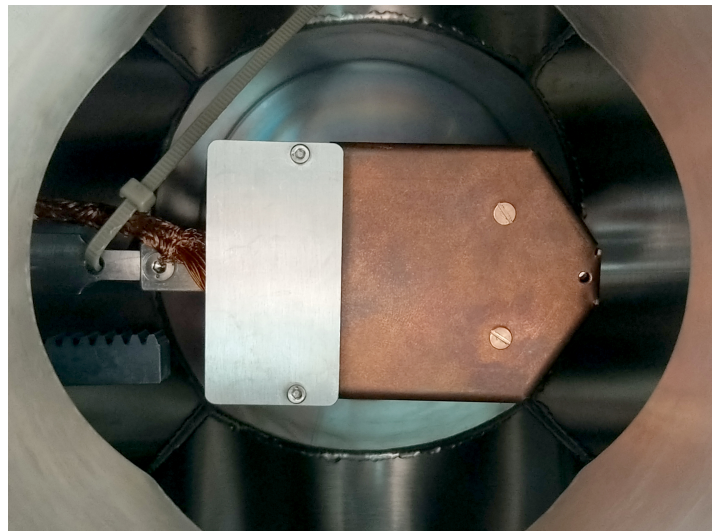

Figure 4.1.: The TRISTAN FBM after mounting on the manipulator in the 6-way cross at parking position. The cable is fixed with a cable tie made of vacuum compatible PEEK plastic, which still needs to be cut in length.

be opened through which the detector is accessible. The already mounted TRISTAN FBM can be seen in figure 4.1. In this configuration measurement with an ^{241}Am photon source were performed. These measurement is described in chapter 4.3. After successful completion, the vacuum was restored. To ensure the vacuum requirements, the system was first baked out for 5 days and simultaneously pumped down for 7 days. When a sufficient vacuum level of P $= 2 \times 10^{-8}$ mbar was reached, the valve to the CPS was opened.

4.2. DAQ and Data Flow

The data acquisition at the FBM comes with some challenges compared to the test measurements done in the lab: First, for monitoring the tritium source the acquisition has to run continuous for several months. Furthermore the rate is expected to be large, with up to 60 kcps per pixel. Additionally the hardware is difficult to maintain, as the whole setup is inside the controlled area of the Tritium Laboratory Karlsruhe (TLK). In this section the technical solutions to address these challenges are summarized.

The combination of high rate and long continuous acquisition makes it impossible to save all listmode data (energy and time stamp for each event) for later processing and analysis. With a maximum count rate of 60 kcps per pixel and an event memory size of 11 byte (8 byte time stamp, 2 byte energy, 1 byte channel) the total data rate reaches 400 GB per day. To reduce the amount of data, the events are histogrammed in real time. This implies that also the multiplicity analysis, for which the listmode data is necessary, has to be performed in real time. Ideally, such analysis could be performed on the FPGA level. However, the corresponding infrastructure on the FPGA is not yet available. Instead, an event-based analysis was performed on a desktop PC. An overview of connections and applications on this computer is shown in figure 4.2. The three applications that are running during data acquisition are the following:

CoMPASS GUI This is the official software provided from CAEN to interface the CAEN v1781 card. It takes care of the configuration and optical fiber communication to the card. During acquisition this application receives the listmode data from each of the eight channels of the card and saves them as binary files on the local disk.

COMPASSConverter This custom software reads the binary files created by CoMPASS GUI and performs real time processing on the data:

1. During the resetting of the preamplifiers, which happens up to 1000 times per second, it can happen, that the DAQ falsly triggers. These events have to be removed from the data. To do that the time stamps of the resets are determined using the inhibit signal of the bias board and the 8th channel of the DAQ card. The COMPASSConverter compares all time stamps of all events in the seven pixels to the time stamps of the resets and removes all events which happened simultaneously to a reset. The time window relative to a reset within which events have to be removed was determined to be $-1\,\mu s$ to $50\,\mu s$.

2. In the binary files created by the CoMPASS GUI all events are sorted by time within their channel only. The COMPASSConverter sorts the events of all channels by their time stamp into one list. This makes it later very easy to determine the multiplicity of an event, because it only has to be compare it to its neighbors in the sorted list.

   The cleaned and sorted list of events is again saved on the local disk.

Run Control GUI This software reads the sorted listmode data provided by the COMPASSConverter and histograms it. Each histogram contains the data of a certain selectable duration. The histograms are then grouped and saved into **runfiles**. A typical runfile contains 3 h of data, where every 5 s a new histogram is created. The Run Control GUI saves a separate histogram for each pixel, and one additional where
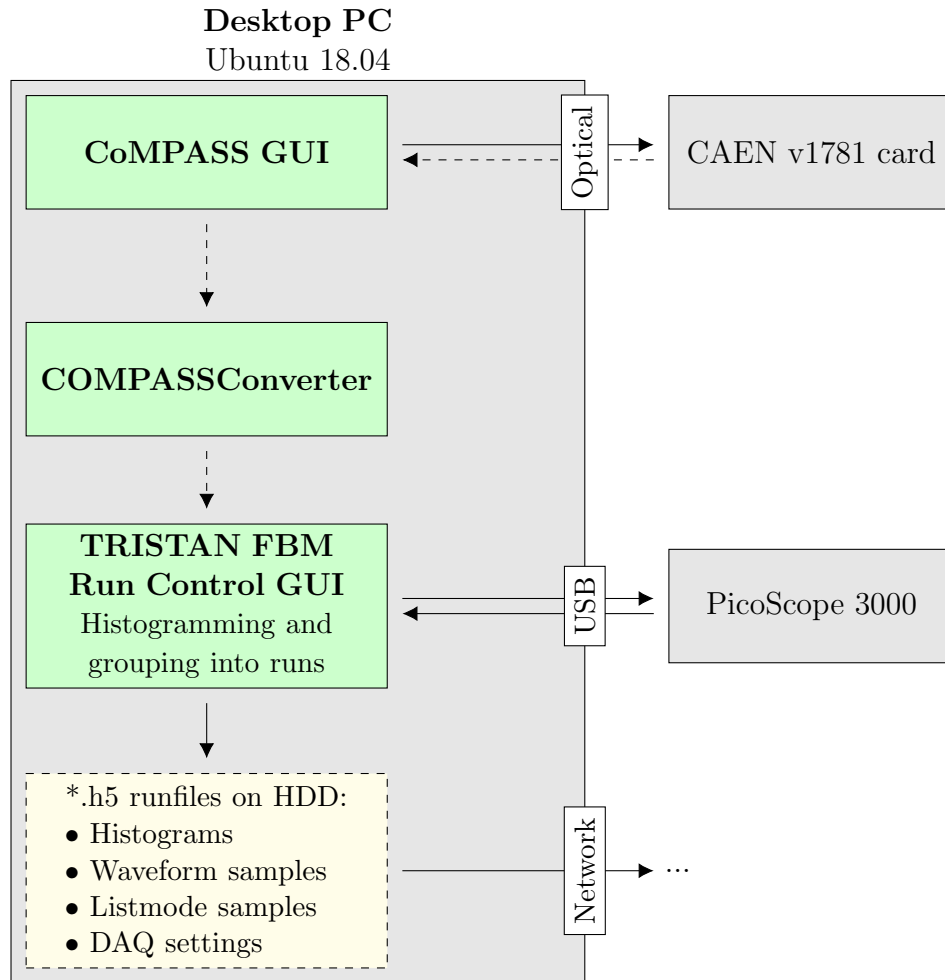

Figure 4.2.: The data flow on the desktop PC which is processing the FBM data. The dashed arrows corresponds to listmode data (energy and time stamp for each event). The throughput of this data is too big to save the data continuously, so it has to be deleted after reading.

a multiplicity cut is performed: In this histogram only events with multiplicity zero that happened in the central pixels are summed. The runfiles also contain additional information, like a short sample of listmode data for debugging and a waveform sample captured by a digital oscilloscope (PicoScope) to monitor the noise on the waveforms during the aquisition. Each runfile should contain all information necessary to interpret and analyze the run afterwards.

To verify the high rate capability of the above described system it was tested with noise triggered events with a rate of around $100\,\mathrm{kcps}$ per pixel. During the test the computer did not get close to the limit of CPU usage or memory.
One drawback of this processing chain is the time delay due to the CoMPASS GUI. This software saves the data on the local disc only when around $1\,\mathrm{MB}$ of new data is available in the channel. For low rates (e.g. if the tritium source is ramped down) it can take several minutes or hours until the data is written. The COMPASSConverter has to wait until data on all channels (including reset) is available to do the cleaning and sorting. One possibility to overcome this issue is to not use CoMPASS GUI, but the C/C++ interface libraries provided by CAEN. This is planned to be implemented in the future.

4.3. Calibration Measurement with ^{241}Am

Before pumping down the FBM chamber, a calibration measurement with ^{241}Am was performed. The goal of the measurement was to obtain a calibration that can later be used for the measured continuous tritium spectrum. Furthermore, the measurement is also important to test the performance of the TRISTAN FBM in its TLK environment for the first time.
The used source contains the radioactive isotope ^{241}Am which decays via α-decay to ^{137}Np with a half live of $433\,\mathrm{a}$. After the α-decay two main γ lines ($59.54\,\mathrm{keV}$ and $26.34\,\mathrm{keV}$) and a huge spread of X-ray lines from ^{137}Np occur. [33]
The source was placed in front of the detector inside of the vented 6-way cross at parking position.

The measured spectrum is shown in figure 4.3. It shows the mentioned γ and X-rays, and also a small contribution of the K_α and K_β lines of copper, probably created by γ-rays interacting in the cover of the detector, which is made from copper. The spectrum with no cut is compared to the spectrum where a multiplicity cut is applied, which removes all events with multiplicity greater than one. This removes most of the lower energy tails of each peak, which are caused by charge sharing events. The peaks itself are not influenced significant by the multiplicity cut, as expected.

For the calibration the peaks at $13.95\,\mathrm{keV}$, $17.75\,\mathrm{keV}$, $20.78\,\mathrm{keV}$, $26.34\,\mathrm{keV}$ and $59.54\,\mathrm{keV}$ are used, which includes the big lever arm of the $59.54\,\mathrm{keV}$ peak. The energy resolution of each peak in the seven pixels is shown in figure 4.4. The FWHM of the $26.3\,\mathrm{keV}$ γ peak is $350\,\mathrm{eV}$ to $400\,\mathrm{eV}$. This worsened resolution compared to the
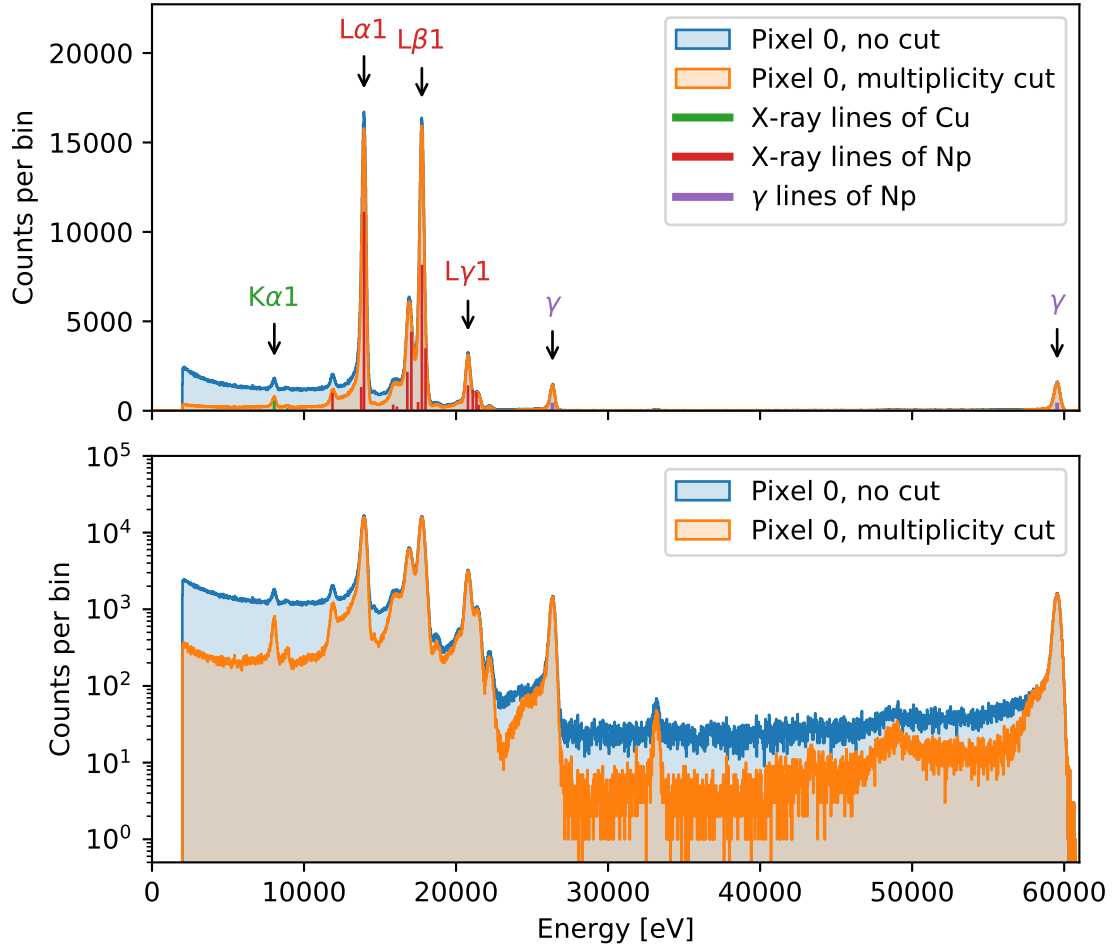
Figure 4.3.: Measured spectrum of the ^{241}Am source in linear and logarithmic scale. The orange histogram contains only events with multiplicity one, so that charge sharing events are removed. The intensities of the shown red and green X-ray lines are only for a rough comparison of the order of magnitude [34].

krypton calibration (see section 3.2) can be explained by larger electronic noise contribution, which can be expected in the TLK environment. The energy resolution of 380 eV for 26.4 keV gives a ENC_{rms} of around 35 electrons, which is significantly larger than in the krypon laboratory measurement with $ENC_{rms} \approx 16$ electrons.

4.3.1. Waveform

The electronic noise can be directly seen in the plot of the digitized waveforms of pulses in the left plot of figure 4.5: A lot of ripple is overlaying the pulses. To investigate the noise, the frequency spectrum of the waveform without pulses is shown in figure 4.6. A lot of structures are obtained in the spectrum, such as excesses at around 5 MHz
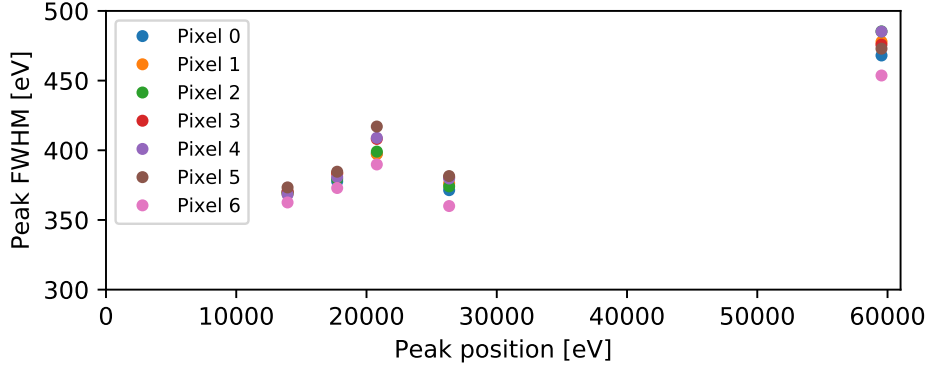
Figure 4.4.: Fitted FWHM of peaks in the ^{241}Am spectrum. A simple Gaussian model was used. The three X-ray peaks (13.9 keV, 17.7 keV and 20.9 keV) may be broadened not only by the detector resolution, but also by the overlap of more than one X-ray transition. However, the γ peaks (26.34 keV and 59.54 keV) are single lines and represent the photon energy resolution of the detector.
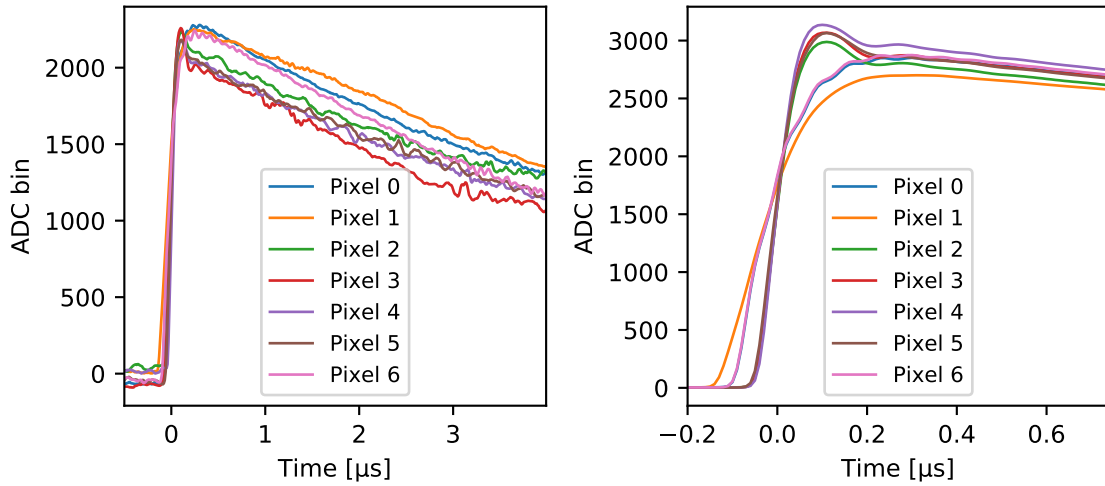

Figure 4.5.: Left: Waveforms of pulses in the ^{241}Am source at the final FBM setup. This should be compared to figure 3.7. The decaying of the pulses comes from the 10 μs AC-coupling at the input of the DAQ card.
Right: Zoom into the rising edge, averaged for many pulses

and 10 MHz. These excesses may not have a big influence to the energy resolution of the detector, as they are suppressed by the trapezoidal filter frequency response, which is also shown in the plot. Frequencies, where the trapezoidal filter frequency response is low, are attenuated by the energy filter and have a reduced influence to the energy resolution. The excesses at 60 kHz and 300 kHz, which have a large amplitude, contribute significantly to the energy resolution. There are different possibilities where
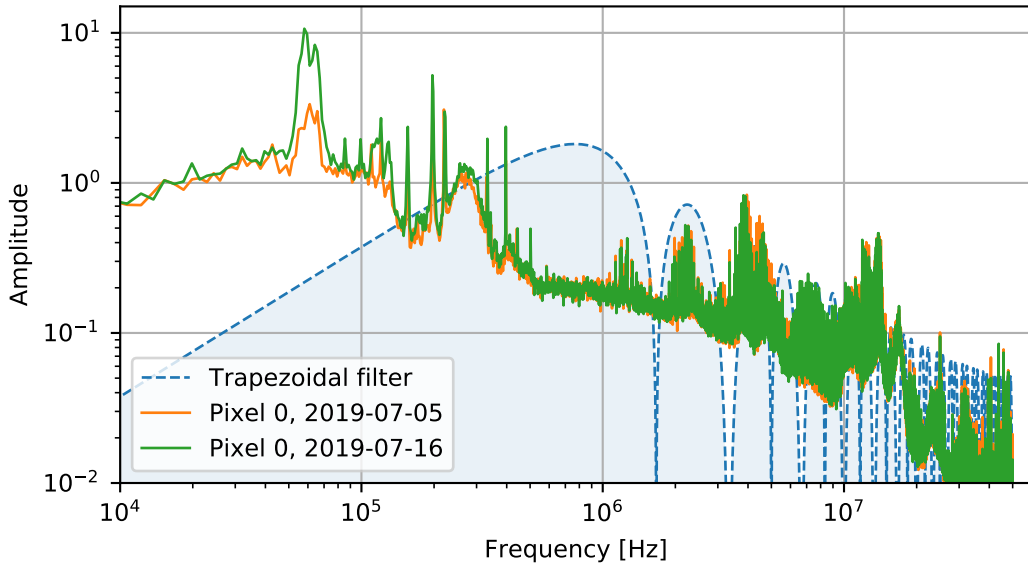
Figure 4.6.: Frequency spectrum of the waveform of pixel 0 in the final TLK setup, measured at two different dates. No pulses were present in the input waveform. The frequency response of a trapezoidal filter ($T_{\text{shaping}} = 300\,\text{ns}, T_{\text{gap}} = 300\,\text{ns}$) is also shown.

noise with these frequencies may come from. An obvious origin is the interference from electric devices nearby, where for example a lot of modern switched mode power supplies operate at frequencies of $50\,\text{kHz}$ to $1\,\text{MHz}$. Another possibility could be the microphonic effect of electrical parts: Most capacitors translate a vibration to a capacitance or voltage ripple. If this happens for example at the $V_{\text{ring 1}}$ voltage filter capacitor on the detector board, the ripple is coupled to the detector anode and be amplified by the whole amplification chain. A third option could be that the anode bond wires itself vibrate and introduce some ripple. Finally also improper ground connections or loops can lead to a ripple on the waveform. Up to now the reason is unknown and should be investigated further.

Besides the ripple on the waveform, also the shape of the rising edge has changed compared to the MPP lab measurement. On the right plot of figure 4.5 many waveforms are averaged to get rid of the noise and ripple. The remaining shape of the rising edge of the pulses has a significant lower slope for pixels 0, 1 and 6 compared to the other pixels. The overshoot, which was also observed in all non-coax pixels in the MPP lab measurement, is still present in pixels 2, 3, 4 and 5, but not in the non-coax pixel 1. The observed shape looks like an over-sized capacitance of the signal line of pixels 0, 1 and 6, or an over-sized resistance on the amplifiers output. One practical explanation could be an increased contact resistance in the pogo pin connector for these pixels. If the contact has a resistance of $\mathcal{O}(100\,\Omega)$ in these pixels, the slope can be explained. Regardless of the shape of the rising edge of the pulses, all seven pixels show a similar performance in the ^{241}Am measurement.
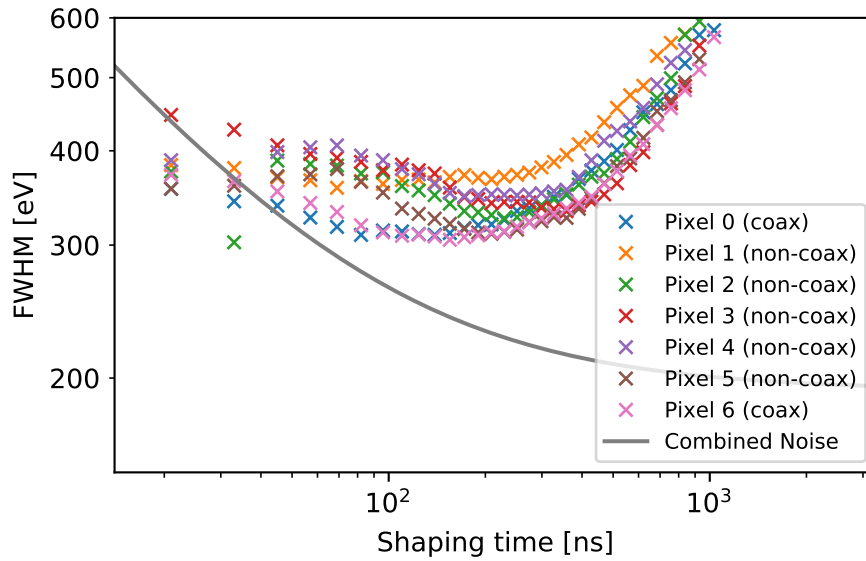
Figure 4.7.: Noise curves for all seven pixels in the final TLK setup, based on the 14 keV X-ray peak in the ^{241}Am spectrum. For comparison the *combined noise* line shows the line which fitted the noise curve quite well in the MPP lab measurement (figure 3.8).

4.3.2. Noise Curve

With the changed noise situation, also the noise curve (compare section 3.2.4) looks different. Figure 4.7 shows the noise curve, based on the 14 keV peak in the ^{241}Am spectrum. There is now clearly a component of noise that disfavors long shaping times, which was not present in the MPP lab measurement. Both measurements were performed at room temperature. This fits to the excesses at 60 kHz and 300 kHz in the frequency spectrum, as a bigger shaping time shifts the trapezoidal filter response towards these lower frequencies.

4.3.3. Time Evolution

As the objective of the FBM is to measure the stability of the WGTS activity, it is important to have stable detector characteristics. To this end, a long duration measurement (around 10 d) with the ^{241}Am source was performed. For this measurement a longer trapezoidal shaping time of 1 μs was chosen.

By fitting a Gaussian to the peaks in the spectrum, the positions and widths of the peaks are determined for every subsets of 5 h in the measurement. The parameter evolution is plotted in figure 4.8. The stability of the calibration of the detector is seen in the position of the 59.5 keV line in the spectrum. The observed position drifts

slightly downwards by around 1‰ within ten days, which is acceptable. The energy resolution on the other hand, shown in the bottom plot in figure 4.8, has a clearly visible step during July 9, 2019. This step can also be seen in the frequency spectra in figure 4.6, which were measured before and after the long-term measurement. The main difference between the two spectra is the excess at 60 kHz, the amplitude of which increased by a factor of 3. Such a step in the energy resolution could be a problem for the tritium activity measurement. To keep track of the noise on the waveform an additional digital oscilloscope was installed in parallel to the DAQ at pixel 6. A short snippet of the waveform is saved every 3 h, which allows to monitor the evolution of noise on the waveform during the activity measurement.
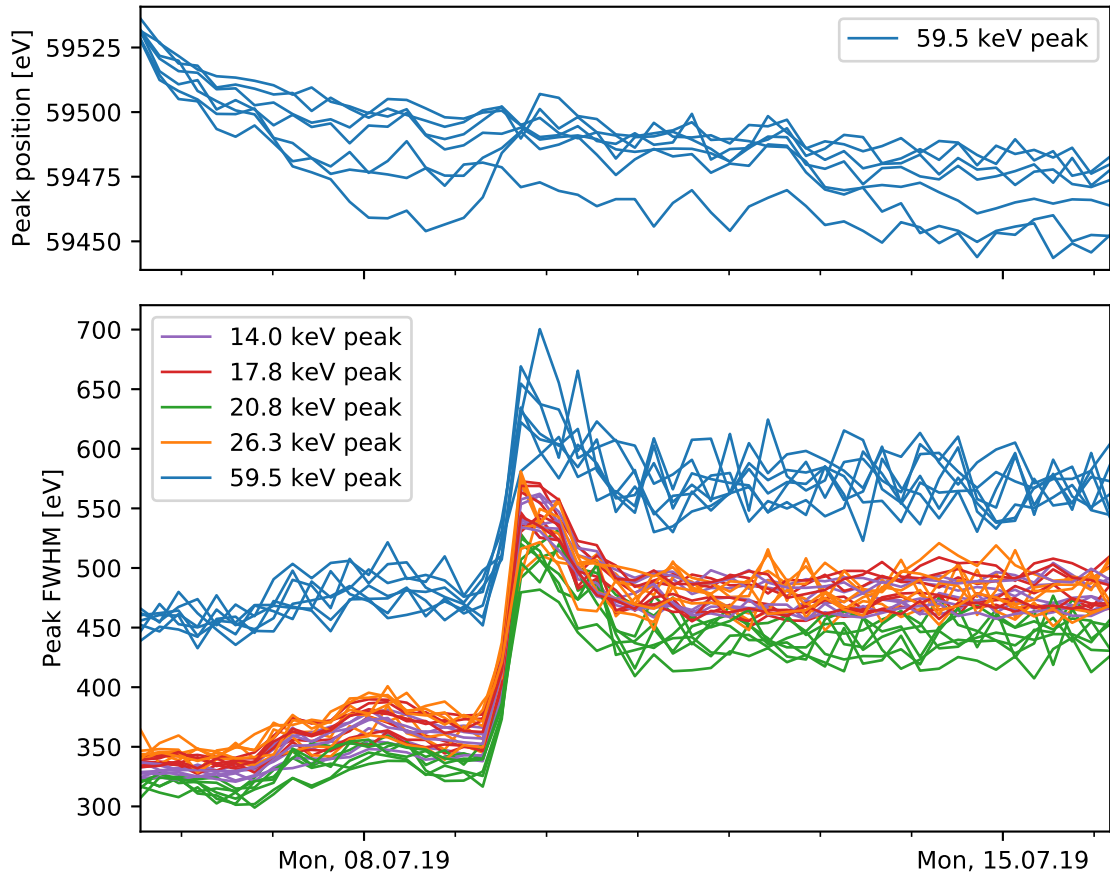

Figure 4.8.: Time evolution of the position and resolution of peaks in the 10 d measurement with ^{241}Am. For each peak seven lines in the same color are plotted, which correspond to the seven pixels.

Conclusion

The TRISTAN FBM was installed successfully in the KATRIN beam line. All seven pixels show a similar performance in the ^{241}Am photon measurement. Some notable effects were observed:

First, the noise on the signals has excesses at 60 kHz and 300 kHz, which dominate the energy resolution of the detector. These noise components shifts the optimal trapezoidal shaping time to short times, the best resolution is observed for only $T_{\text{shaping}} = 300$ ns. Furthermore the noise is not stable over time, a step in the energy resolution of around 200 eV was observed on July 9, 2019. While this was measured at $T_{\text{shaping}} = 1000$ ns, the influence of the time dependent noise is expected to be smaller at $T_{\text{shaping}} = 300$ ns.

Second, pixels 0, 1 and 7 have a significant lower slope of the rising edge of the pulses. This may be caused by a contact resistivity of the vacuum connector to the detector board. Fortunately, with a long enough trapezoidal gap time $T_{\text{gap}} \geq 300$ ns this seems to not influence the performance significantly.

While these two topics should be further investigated, they are not crucial for the rate-monitoring for KATRIN. Despite the increased noise situation an energy resolution of around 500 eV is expected, which is a significant improvement compared to the previous PIN diode detector with an energy resolution above 2 keV.

5. The TRISTAN FBM during the KATRIN Measurement Phase

In Autumn 2019 the KATRIN experiment started its second neutrino mass measurement campaign, called KNM2 (KATRIN Neutrino Mass 2) with the goal to take two months of tritium data with the nominal source activity. The following chapter shows and discusses the performance of the TRISTAN FBM during the measurement phase. Next to that the shape of the measured tritium spectrum is addressed, which is a first step towards the full tritium spectrum investigations for TRISTAN.

5.1. Deployment and First Light

During test measurements after installation (section 4.3) the TRISTAN FBM detector was in its parking position outside of the KATRIN beamtube. After the following bake-out and pumping the valve to the beam line was finally opened and the detector was deployed into the beam tube at 13. August 2019.

At its final position in the beam tube the FBM cools down due to thermal radiation, as the surrounding part of the CPS has a temperature of around 70 K. With a time constant of several hours the detector finally reaches an equilibrium temperature of
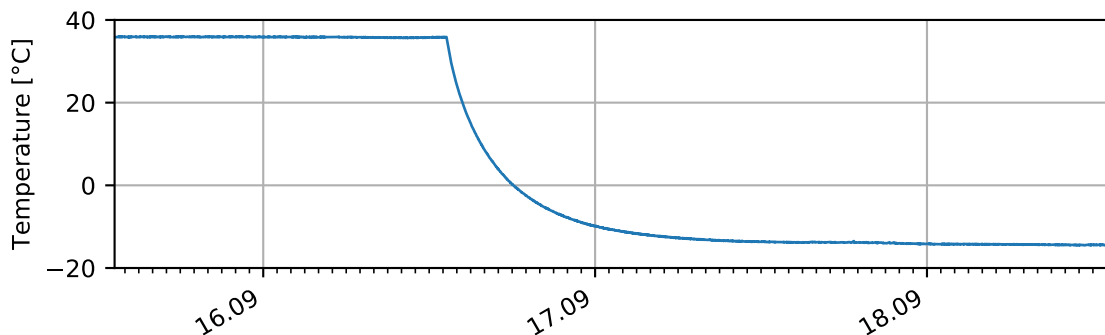

Figure 5.1.: Temperature evolution of the TRISTAN FBM detector during the deploying. Due to the heating of the electronics the detector had a temperature of 35 °C before deployment and reached an equilibrium of around −15 °C in the cold CPS environment.
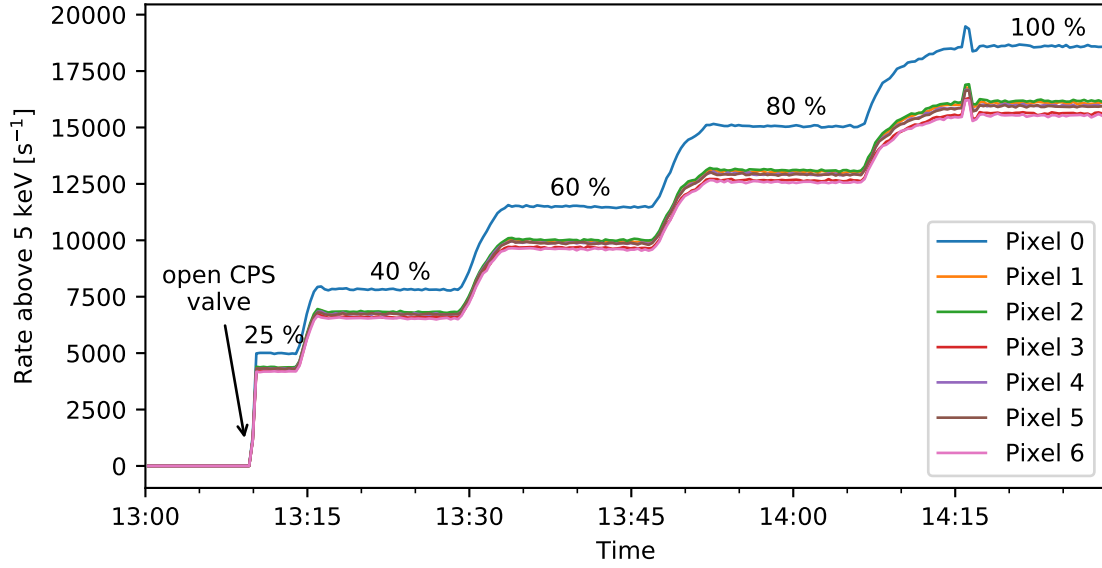
Figure 5.2.: The count rate in the seven pixels of the FBM during the ramp-up of the WGTS. At 13:10 the valve in the CPS towards the WGTS was opened.

around $-15\,°C$, as shown in figure 5.1.

At 18. September 2019 the WGTS of KATRIN was ramped up in steps to the nominal column density. The TRISTAN FBM was at its monitoring position at the outer brim of the flux tube during the ramp-up and measured the step-like increase of the electron flux, as shown in figure 5.2. The shown rate is calculated by summing all events in the spectrum above a threshold of $5\,keV$. For a proper rate calculation, besides the number of counts, also the live time T_{live} has to be known. For each data point in the rate plot it is calculated by

$$T_{\mathrm{live}} = T_{\mathrm{aquisition}} - n_{\mathrm{resets}} \cdot T_{\mathrm{dead\ resets}} - n_{\mathrm{trigger}} \cdot T_{\mathrm{trigger\ holdoff}} \qquad (5.1)$$

$T_{\mathrm{dead\ resets}}$ corresponds to the $51\,\mu s$ during each reset where events are discarded by the COMPASSConverter software. $T_{\mathrm{trigger\ holdoff}}$ is the dead time of $5\,\mu s$ introduced by the trigger holdoff setting in the DAQ card[1]. The number of triggers n_{trigger} is obtained by summing over the whole histogram of counts without any energy cut.

The observed rates in the seven pixels agree within $5\,\%$, except for the central pixel which sees a rate increased by around $15\,\%$ compared to the surrounding pixels. This can be caused by a different effective area of the outer pixels due to the detectors border, which is the back frame.

---

[1]This large trigger holdoff is currently necessary, as the DAQ card crashed otherwise during movement of the FBM stepper motors due to the high amount of noise triggered events. The trigger holdoff limits the throughput of noise triggered events to $200\,kcps$. In the future it is planned to pause the acquisition automatically during movement, then the large trigger holdoff can be omitted.

The final settings for the DAQ that were used during KNM2 are stated in table A.3. After the ramp up of the KATRIN source, several test measurements were done, for example a scan to find the best monitoring position. These measurements are not addressed in this thesis.

5.2. Measured Tritium Spectrum

After the ramp up the TRISTAN FBM measured the tritium electron spectrum for the first time. The obtained spectra are shown in figure 5.3 for 3 h of data. The following features are obtained in the spectra:
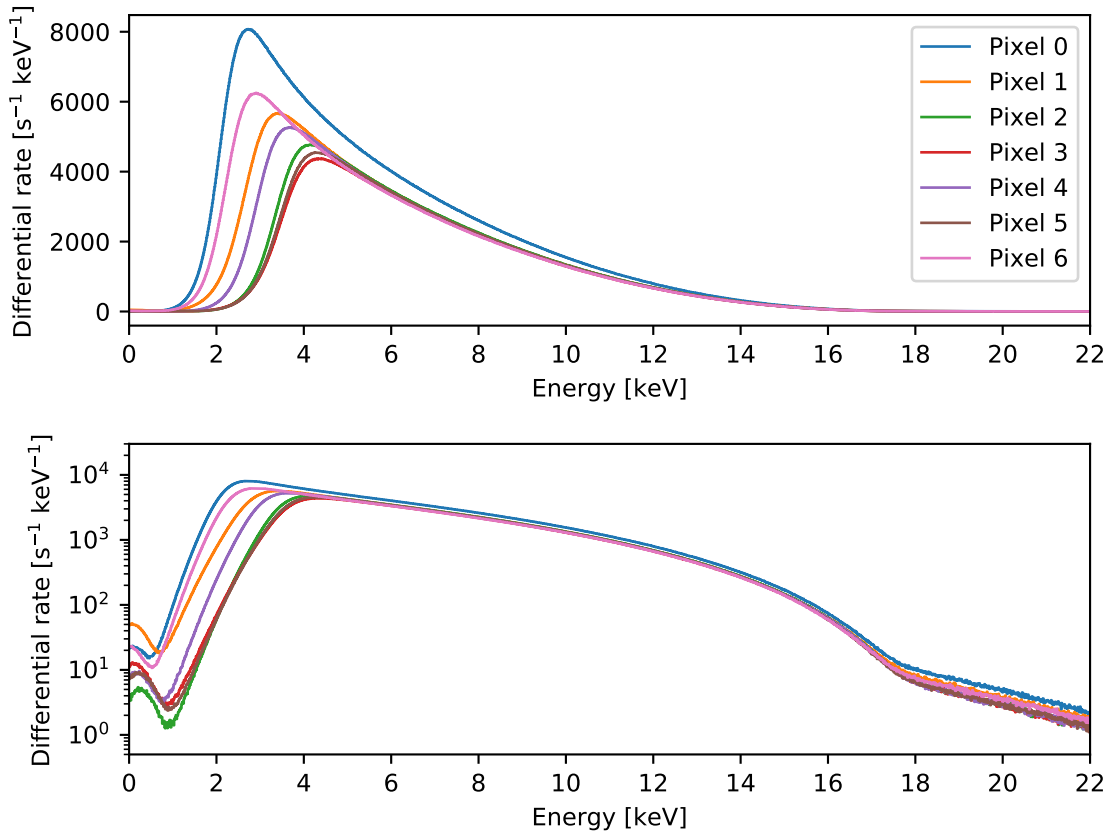

Figure 5.3.: Tritium β-spectrum measured with the TRISTAM FBM detector in linear (top) and logarithmic (bottom) scale

- The region below $5\,\mathrm{keV}$ is dominated by the threshold that is set in the DAQ card. For the individual pixels different thresholds were chosen due to the different noise situations on the pixels. The threshold was determined with respect to the amount of noise-triggered events. These correspond to the small peak around zero, only visible in the logarithmic plot. The thresholds were chosen conservatively, to have a very low contribution of non-physical noise-triggered events to the spectrum. Even if the noise situation changes during the measurement phase, as observed in the $^{241}\mathrm{Am}$ test measurement, the amount of noise-triggered events stays acceptably low.

- Between $5\,\mathrm{keV}$ and $17\,\mathrm{keV}$ the differential tritium spectrum is observed. The detector response has a huge influence on the observed shape. Details on a model for the observed shape can be found in section 5.2.1.

- Close to and above the endpoint of the β-spectrum pile up becomes visible. The most dominant pile up of two events leads to a continuous spectrum up to double the endpoint energy, which is far outside of the shown energy range.

The observed spectra of the seven pixels agree well with each other. The pile up is slightly increased on pixels 0, 1 and 6. These are the pixels where the waveforms of pulses have a significant different shape (see figure 4.5).

5.2.1. Model of the Detector Response

To further investigate the shape of the observed spectrum a model for the detector response is necessary. The detector response is a function $F(E_{\mathrm{in}}, E_{\mathrm{detected}})$, which describes for a given incoming particle energy E_{in} the probability density for the detected energy E_{detected}. This detector response is a delta function in E_{detected} for an ideal detector. In practice several effects broaden and change the shape of the detector response: There are physical effects like backscattered electrons, escaping X-rays or charge sharing, as well as electronics and DAQ related effects like noise or pile up, only to name a few. In the following a model for the detector response for the FBM is developed, which includes the most important effects.

Charge sharing As discussed in section 3.3 charge sharing is very important for the FBM due to its small pixel size. The detector response due to charge sharing can be obtained from the probability distribution of η (equation 3.2). As η describes the amount of charge collected in one pixel, the amount of detected energy E_{detected} in this pixel is

$$E_{\mathrm{detected}} = \eta \cdot E_{\mathrm{in}} \tag{5.2}$$

The resulting response function is plotted for different incoming energies and charge cloud widths w in figure 5.4.
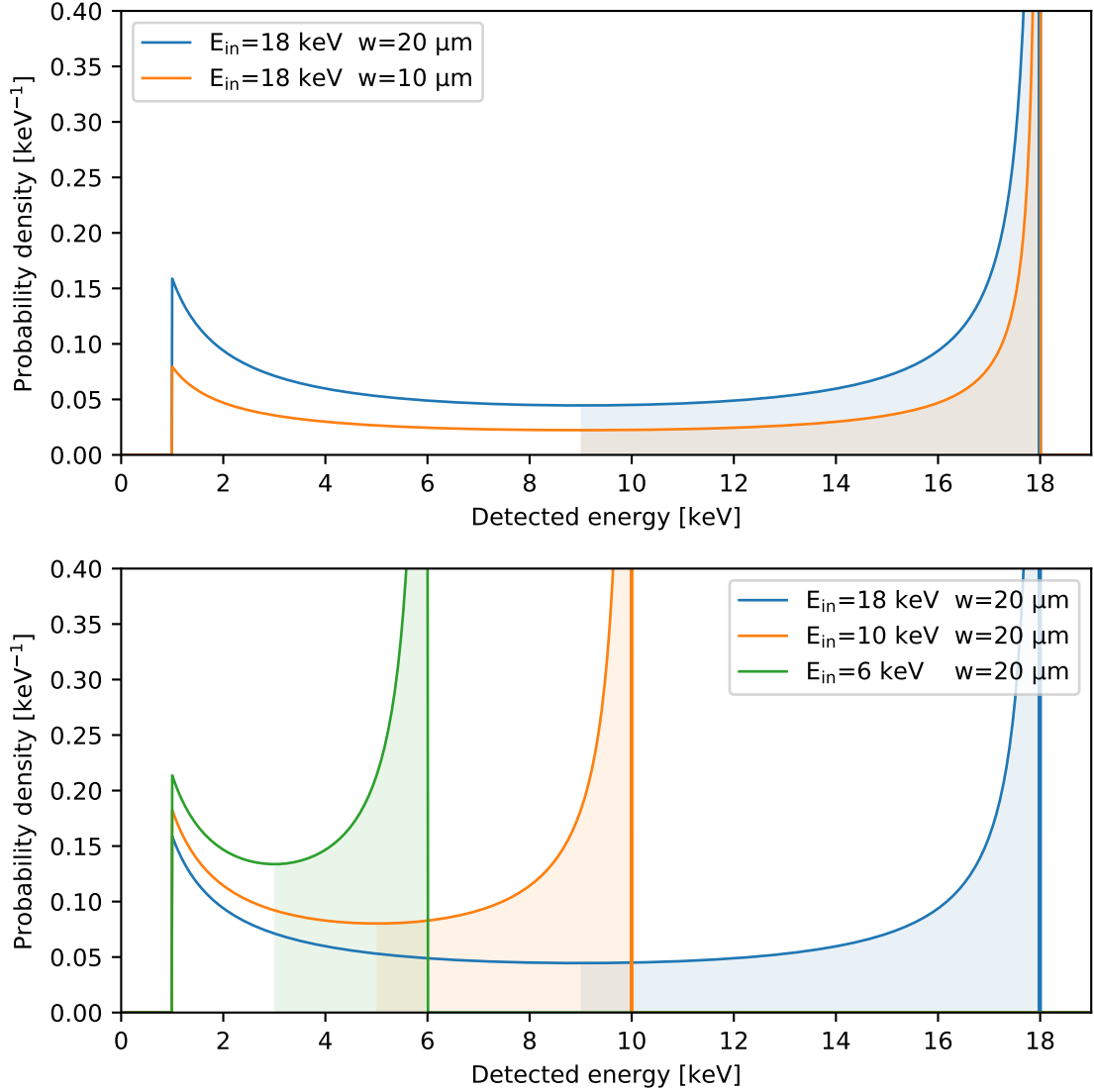
Figure 5.4.: Detector response due to charge sharing for different energies and charge sharing widths w. The shaded areas of the responses are normalized to one. A detector threshold of $1\,\mathrm{keV}$ is assumed.

The correct normalization of the response is important. All incoming events that hit the area within the borders of the pixel have a $\eta > 0.5$ and the resulting E_{detected} is shaded in figure 5.4. This shaded area has to be normalized to one, as the response is normalized to one incoming electron on the pixel area. This is not trivial, as the PDF of η written in equation 3.2 is not normalizable, but its integral goes to infinity for $\eta \to 1$. This is related to the simplification in the model, that assumed a linear but not circular pixel geometry. Fortunately, the imprint of this simplification is only present at η very close to 1 and therefore will be washed out by the detector resolution. The
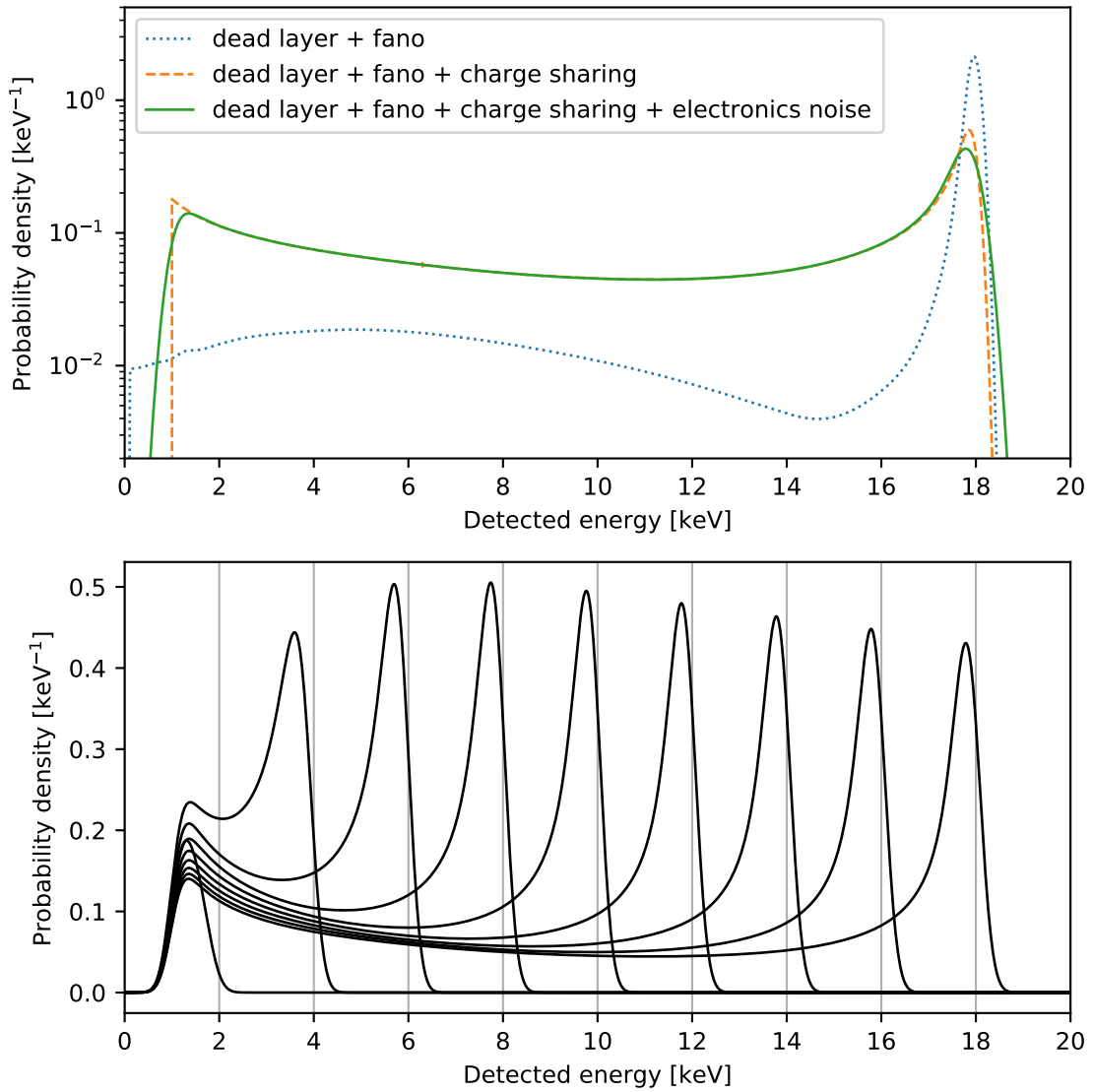
Figure 5.5.: Top: The detector response for $E_{\mathrm{in}} = 18\,\mathrm{keV}$. The considered effects in this thesis are included one after the other. **Bottom:** The total detector response for $E_{\mathrm{in}} = 2\,\mathrm{keV},\ 4\,\mathrm{keV},\ ...,\ 18\,\mathrm{keV}$.

shown responses in figure 5.4 are normalized correctly, which means that the integral over the shaded areas is one.

Other response contributions   Besides the effect of charge sharing three more effects were included to the detector response:

- The effects from the energy loss in the detectors dead layer and back scattering is summarized in the detector response labeled **dead layer**. The used response was obtained from a database setup by Marc Korzecheck[18] based on KESS[35] simulations. For simplicity it was assumed that the electrons hit the detector perpendicular and the dead layer is step-like with a thickness of 50 nm.

- The **Fano** noise was added as a Gaussian broadening with $\sigma = \sqrt{F E_{\text{in}} \epsilon}$

- The **electronics noise** was added as a Gaussian broadening with $\sigma = 200\,\text{eV}$.

To combine all the four mentioned contributions to the detector response one has to apply them one after the other. Numerically each response can be expressed as a matrix M where the rows correspond to E_{detected} and the columns to E_{in}. For the calculations in this theses an energy binning of 10 eV from 0 keV to 20 keV was chosen resulting in a size of 2000×2000 for each response matrix. The total response M_{tot} can be calculated by:

$$M_{\text{tot}} = M_{\text{electronics noise}} \times [M_{\text{charge sharing}} \times [M_{\text{fano}} \times M_{\text{dead layer}}]] \tag{5.3}$$

As the matrix multiplication is not commutative it is important to do the calculation in its physically correct order. Figure 5.5 shows the total detector response after combining the four contributions. The integral of the response for $E_{\text{in}} = 18\,\text{keV}$ is around 1.4. This value, bigger than one, is a result of the normalization to one incoming event per pixel area: Due to the Gaussian charge cloud also events outside of the pixel area can lead to an event. This normalization changes a lot with the threshold, which was chosen arbitrarily to 1 keV in this case. If the threshold was chosen to be at 9 keV for the response for $E_{\text{in}} = 18\,\text{keV}$, only events within the pixel border are detected. The resulting response integrates to 0.84, which fits roughly to loss of events due to back-scattering [35].

Next to the detector response there are many more influences to the measured spectrum: There are effects of the tritium source like scattering of the electrons in the tritium gas and back-scattering at the rear wall. Electrons that are back-scattered by the FBM detector may also be magnetically back-reflected onto the detector by the magnetic mirror effect. These effects are not yet taken into account, but will be included in the future to get a more precise model.

5.2.2. First Fit

The detector response for the FBM, derived in the previous section, is now used to model the measured tritium spectrum. The β-electron spectrum from the tritium decay

is calculated according to equation 1.10 with $m_\nu = 0$:

$$\frac{d\Gamma}{dE} = C \cdot F_C(E) \cdot \sqrt{(E + m_e)^2 - m_e^2} \cdot (E + m_e)(E_0 - E)^2 \tag{5.4}$$

Figure 5.6 shows the resulting spectrum, without and with the detector response applied. The detector response has a huge impact to the shape of the observed spectrum, and shifts a lot of events to lower energies.

To compare this spectrum, in the following called model(E), to the measured spectrum a χ^2 fit was performed. The fitted function R that describes the measured differential rate is:

$$R(E, \text{gain}, A, A_{\text{pu}}) = \quad \text{model}\left(\frac{E}{\text{gain}}\right) \cdot \frac{A}{\text{gain}} \quad + \quad \text{model}_{\text{pu}}\left(\frac{E}{\text{gain}}\right) \cdot \frac{A_{\text{pu}}}{\text{gain}} \tag{5.5}$$

The second term $\text{model}_{\text{pu}}(E)$ is a simplified model for pile up and is obtained by convolving model(E) with itself. The three free parameters in the fit are the detectors energy gain, the amplitudes A of the spectrum and the amplitude A_{pu} of the pile up spectrum. The gain changes the scales both in x and y direction, as the gain should not change the integral over the spectrum. The performed fit should be seen as a comparison of the model to the measured data, but not as an advanced fit to obtain physics parameters like the charge cloud width w. The result of the fit is shown in figure 5.7. Only a small amount of data, corresponding to one minute of measurement time, and the spectrum above $10\,\text{keV}$ was used in the fit.

The model can also be fitted to lower energies or more data than one minute of measurement time. In both cases the fit is soon dominated by shape distortions. This is
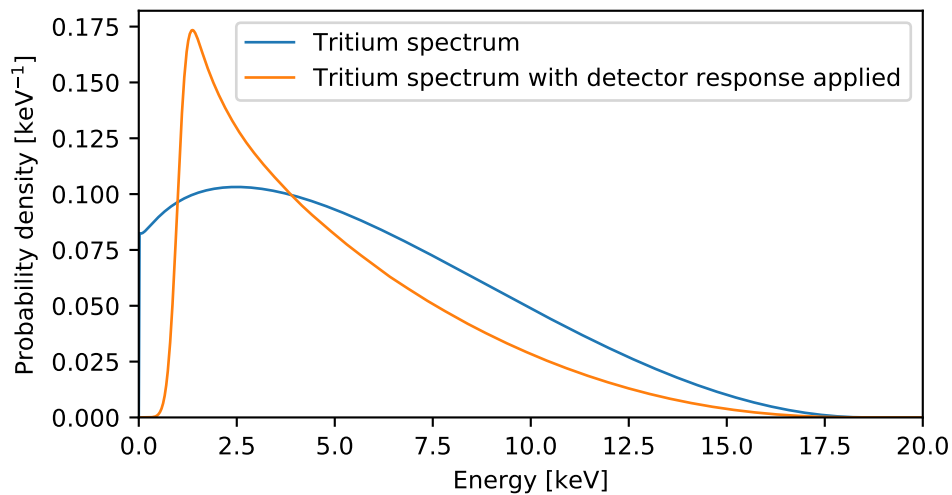

Figure 5.6.: Tritium β-spectrum, without and with the detector response applied. The blue spectrum is calculated with equation 5.4.
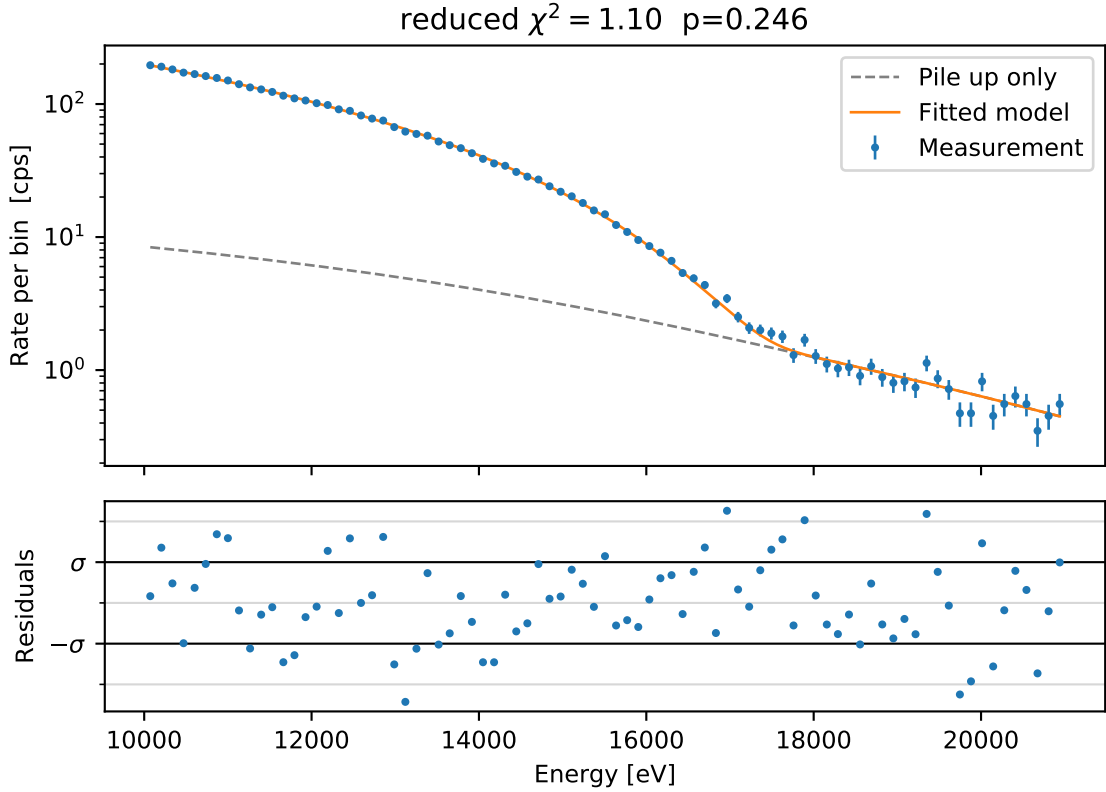
Figure 5.7.: Fit to one minute of measured data. Only the data of the central pixel is used. Around 2×10^5 events were captured in the shown range.

expected, as the model is not complete, and many parameters in the model were only estimated. But the fit shows that the general shape of the obtained spectrum matches the expectation. Besides the shape, also the absolute amplitude of the observed spectrum fits: The best-fit value of the parameter A is 52 kcps. This is close to the expected rate per pixel area, which is around 50 kcps.

5.3. Rate Evolution

The primary task of the FBM is to monitor the activity of the tritium source of KA-TRIN over time. The standard way to determine the FBM rate is to integrate all events above a certain energy cut. While this measures the rate in the spectrum, it is also sensitive to a change of the gain of the detector system. An alternative way to determine the FBM rate is to fit the model described in the previous section to each spectrum. As, besides the rate (or amplitude A), also the gain is a free parameter in the fit, this disentangles the measured rate from the detector gain.

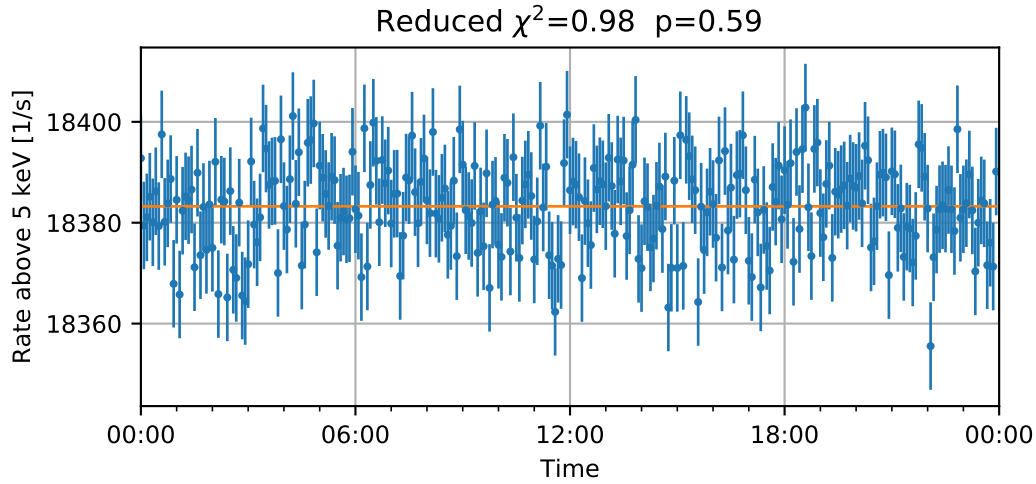Figure 5.8 shows an example of the measured rate over 24 hours, obtained by summing

Figure 5.8.: The rate in the central pixel during one day (Novemver 17, 2019). Each data point corresponds to five minutes. The statistical error on the data points, calculated form counting statistics, is only $0.47\,\text{‰}$.

over the spectrum, with a cut at $5\,\text{keV}$. The statistical uncertainty is dominating in the plot, and the observed rates are compatible with a constant source activity. This on the one hand shows the time stability of the tritium source of KATRIN, but also of the FBM detector.

With an energy cut at $5\,\text{keV}$ the aimed statistical uncertainty of 10^{-3} is reached after one minute of measurement time. If all pixels are summed, this uncertainty is already reached after $10\,\text{s}$. This fulfills the design goal to measure the source activity to a precision of 10^{-3} within one minute.

Long term drift The long time evolution of the FBM rate is not dominated by statistics. As shown in figure 5.9, there are several steps and features in the rate. The fluctuations of the tritium source are also observed with other monitoring devices like the throughput sensor or the BIXS detector. One explanation for the fluctuations are slight temperature variations on the long tritium injection capillary, when the corresponding liquid nitrogen vessel is refilled. With the changing temperature the conductance and also the tritium throughput changes. This is only one example of an effect leading to a slight activity fluctuation in the very complex windowless gaseous tritium source.

Not only fluctuations, but also a general downwards trend is visible in the FBM rate. This trend is not observed in the other monitoring devices. Within one month, the FBM rate decreased by about $1.5\,\%$ and there is also a pixel dependence.

Besides the rate obtained by the cutting method, the evolution of the fitted parameters rate and gain is also shown in figure 5.9. The fitted gain stays within $1\,\text{‰}$ over one
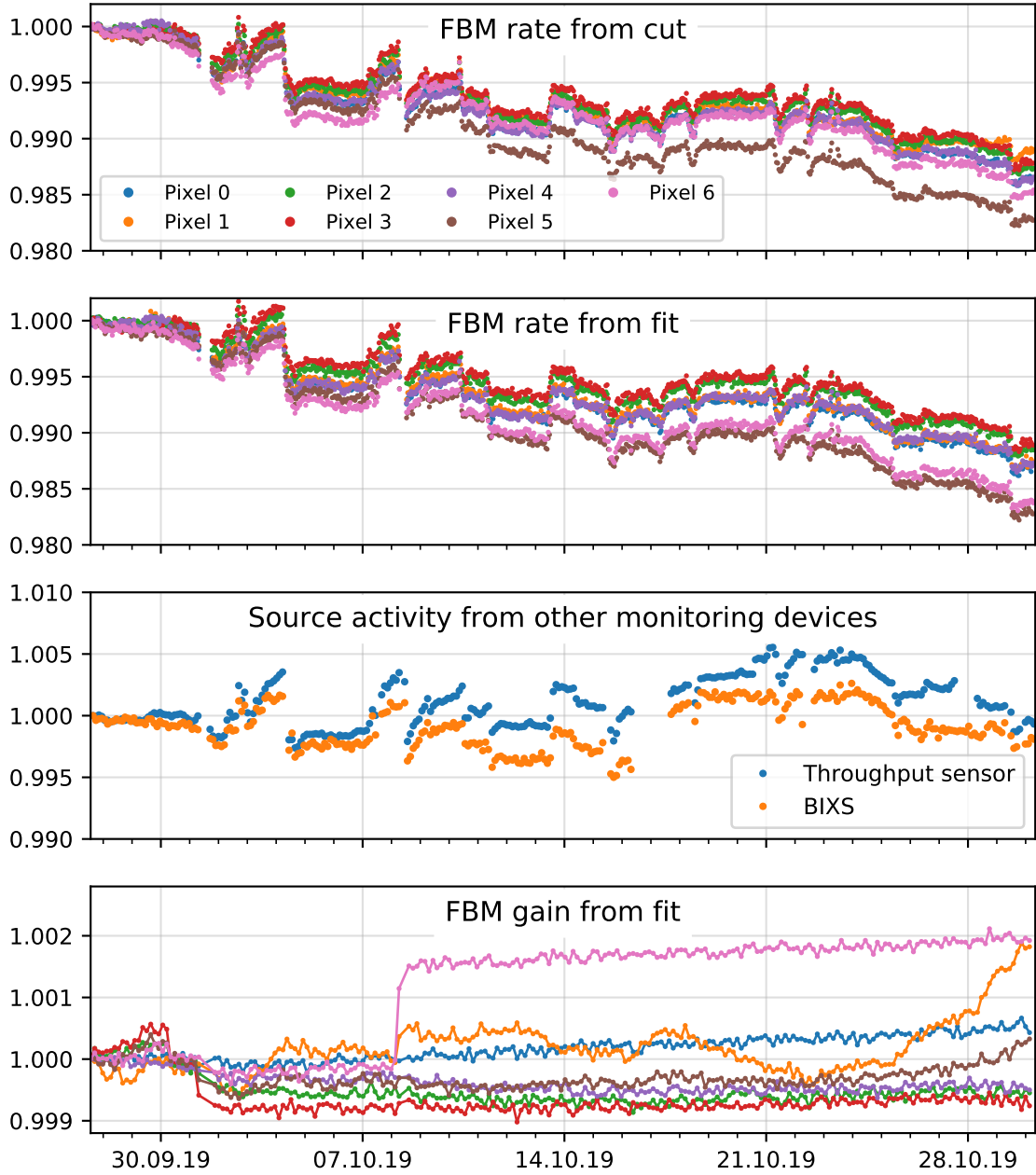
Figure 5.9.: Evolution of different observables during one month of the tritium measurement phase. On the y-axis the value relative to the first data point of each data set is plotted. If not stated differently, each color in a plot belongs to one pixel of the FBM.

month for most pixels. Pixel 1 and pixel 6 show more structure. The step of 1.5 ‰ in pixel six can be explained by a change of the termination of the transmission line to the DAQ, when the pico scope (see section 4.3.3) was added in parallel to the DAQ at

October 8, 2019.
The increase of the gain of pixel one in the last two days can not yet be explained. The gain is reflected in the evolution of the FBM rate from cut, where the rate of pixel one increases within the last two days compared to the other pixels.
The fitted FBM rate on the other hand is not sensitive to the gain. As the overall downwards trend is still present in the fitted FBM rate, the gain can be ruled out to cause the drift. In the evolution of the fitted rate a very interesting feature becomes visible: The drift seems to be categorized into three groups. Pixels two and three have the smallest drift, pixels zero, one and four drift a bit more and pixel five and six have the biggest downwards trend. This fits to the radial coordinate of the pixels in the flux tube, as shown in the appendix figure A.1. This may be a hint that there is a time dependent radial drift in the electron flux. The pixel and time dependent downwards drift of the FBM rate is currently under investigation.

5.4. FBM Sensitivity to Sterile Neutrinos

By measuring the tritium β-decay spectrum with high statistics, the FBM has the potential to search for sterile neutrinos. During KNM2 already around 1.7×10^{12} β-electrons reached the sensitive area of the FBM detector. This leads to a theoretical statistics-only sensitivity for the sterile neutrino mixing $\sin^2 \theta$ of $\mathcal{O}(10^{-5})$, as shown in figure 5.10. Besides the sensitivity assuming an idealized detector response (only including a $300 \, \text{eV}$ energy resolution), also the sensitivity assuming a realistic response is shown. For the realistic response, a model similar to figure 5.5 is used. It includes the effect of a $50 \, \text{nm}$ step-like dead layer and charge sharing in the small $250 \, \mu\text{m}$ pixel-diameter detector. Furthermore an electronics noise of $\Delta E_{\text{FWHM}} = 480 \, \text{eV}$, the Fano noise and an energy threshold of $5 \, \text{keV}$ is assumed. This detector response has a significant influence on the observed spectrum (compare figure 5.6). The accessible parameter range for m_{sterile} decreases to $13 \, \text{keV}$ due to the $5 \, \text{keV}$ threshold. For low sterile masses up to around $10 \, \text{keV}$ the mixing sensitivity decreases by a factor of two. This is a small effect on the sensitivity due to its logarithmic nature.

The study assumes, that the detector response and the incoming electron spectrum are perfectly known. Unknown parameters in the model, or features in the observes spectrum that are not understood, will worsen the sensitivity significantly.

The statistical sensitivity of the FBM supersedes current laboratory-based limits for the sterile neutrino mixing amplitude by almost two orders of magnitude, already with a measurement time of $50 \, \text{d}$. The limiting factor to probe this parameter space currently is the missing model to describe the measured spectrum well enough. This gives motivation to further improve the first simplified model, which was developed in this thesis.
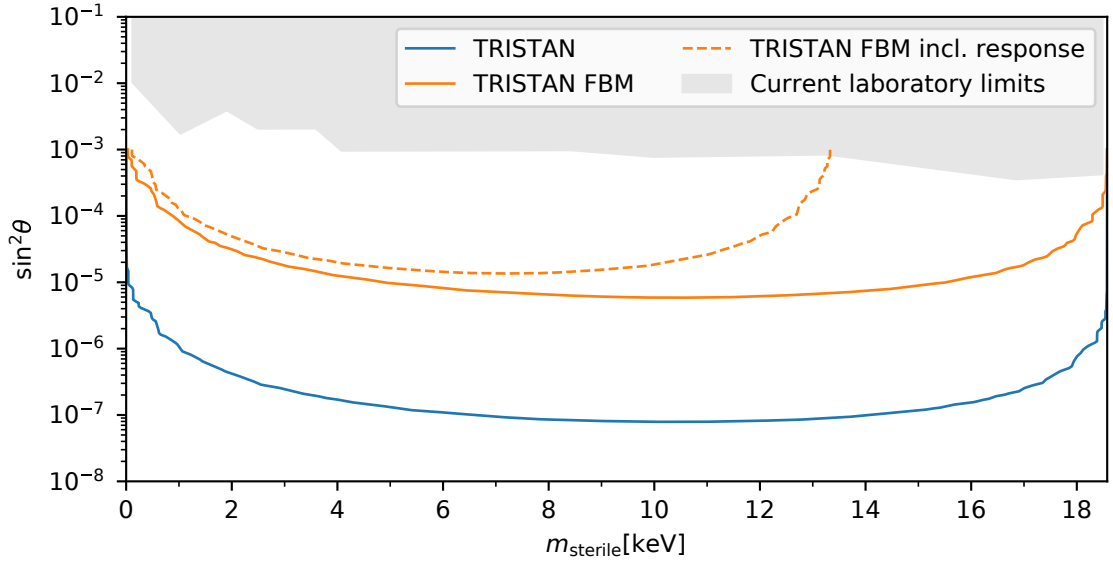
Figure 5.10.: The 95 % C. L. statistics only sensitivity to the sterile neutrino parameters m_{sterile} and $\sin^2\theta$ for different scenarios: The *TRISTAN* sensitivity assumes 3 yeas of measurement time with a total rate of 10^8 cps. No detector response was taken into account, except for a energy resolution of $\Delta E_{\text{FWHM}} = 300\,\text{eV}$ over the whole energy range. The *TRISTAN FBM* sensitivity assumes $50\,\text{d}$ of measurement time with a total of $7 \times 55 \times 10^3$ cps, similar the altready taken data in KNM2. The *TRISTAN FBM incl. response* sensitivity additionally assumes the FBM detector response similar to section 5.2.1 with a detector threshold of $5\,\text{keV}$. The current laboratory limits are adopted from figure 3 in [13].

6. Conclusion

In this thesis the KATRIN Forward Beam Monitor was successfully upgraded with a 7-pixel Silicon Drift Detector System, developed in the context of the TRISTAN project. The novel system entails the SDD chip, a newly designed, vacuum-compatible Printed Circuit Board with low-noise preamplifiers, holding and shielding structure, a bias system, and a DAQ system. Most of these components were designed, procured, and assembled in the context of this work. The integrated system was first tested in a dedicated test stand at MPP with a krypton calibration source, providing both X-rays and mono-energetic electrons.

Despite the 5 m long, partially unshielded cables, an excellent energy resolution of $\Delta E_{\mathrm{FWHM}} < 220\,\mathrm{eV}$ for 14 keV X-rays was achieved, which corresponds to a noise performance of $\mathrm{ENC}_{\mathrm{rms}} \approx 16$ electrons. For electrons an energy resolution of $\Delta E_{\mathrm{FWHM}} < 350\,\mathrm{eV}$ at energies up to 32 keV was observed.

A main focus of this work was put on the characterization of charge sharing. This effect plays a major role for the detector response, due to the small pixel diameters of 250 µm. In this work a model for charge sharing, based on a Gaussian-shaped charge cloud was developed. The comparison of charge sharing for X-rays and electrons with the model supports the assumption of Gaussian-shaped charge clouds dominated by diffusion.

In Summer 2019 the system was successfully integrated in the KATRIN beamline. In the new environment noise components with frequencies of 60 kHz and 300 kHz were observed on the analogue signals of all pixels, which increased the electronic noise contribution to around $\mathrm{ENC}_{\mathrm{rms}} \approx 35$ electrons. Up to now the origin of this noise is not yet found, further investigations are planned for the next maintenance phase of the experiment.

For the continuous operation at high rates of up to 50 kcps per pixel a software for real time multiplicity analysis and histogramming was developed. This reduces the produced amount of data from 130 GB/d to less than 1 GB/d. The full system was successfully operating during the second KATRIN science run from September until November 2019. A rate stability of 0.1 % for time periods of 24 h could be demonstrated, which meets the KATRIN specifications. Over longer periods a drift of 1.5 % per month was observed, which is still under investigation.

To fully exploit the high-resolution of the SDD system, additional information can be extracted by analyzing the spectral shape of the observed tritium β-decay. On the one hand, a spectral fit can mitigate systematic uncertainties in the rate determination, as, for example, this method is less prone to shifts of the detector gain. On the other hand, the spectral analysis allows for a sterile neutrino search. In this work, a

6. Conclusion

simplified tritium β-decay model was developed, taking into account the most relevant detector effects. A good agreement between the model and the observed β-decay spectrum above $10\,\text{keV}$ was found. Finally, this model was used to calculate the sensitivity of the TRISTAN FBM to sterile neutrinos. For an observation time of $50\,\text{d}$, which corresponds to the already taken data during KNM2, an unprecedented sensitivity for the mixing angles down to 2×10^{-5} could potentially be reached.

The application of a 7-pixel TRISTAN prototype in the KATRIN beam line depicts a major milestone of the TRISTAN project. This concerns the advanced technological solutions like high-rate data handling and vacuum compatibility as well as the analysis techniques, by providing first high-statistics, high-resolution differential tritium β-decay spectra.

A. Appendix

A. Appendix

A.1. FBM Pinout

Table A.1 shows the pin assignment of the FBM detector board.

#		#	
1	Back Frame	12	GND
2	Reset	13	Output 4
3	GND	14	V_{SSS}
4	Ring X	15	Output 3
5	Output 7	16	V_{IO}
6	V_{S}	17	Output 2
7	Output 6	18	GND
8	V_{IO}	19	Temp
9	GND	20	Output 1
10	GND	21	Back Contact
11	Output 5	22	Ring 1

Table A.1.: Pinout of the TRISTAN FBM detector board. The blue shaded pins are the ones that supply the depletion and drift voltages for the SDD.

A.2. Fano Noise

The Fano factor F of a detector describes the statistics of charge creation in the detector. It is defined as

$$F = \frac{\text{observed variance in } N}{\text{Poisson predicted variance } (= N)} \tag{A.1}$$

N is the number of charge units created by an event in the detector. It follows $\sigma_N = \sqrt{FN}$.

For a certain incoming energy E this leads to the following observed sigma of the measured energy

$$\sigma_E = \epsilon \cdot \sigma_N = \epsilon \cdot \sqrt{F\frac{E}{\epsilon}} = \sqrt{FE\epsilon}, \tag{A.2}$$

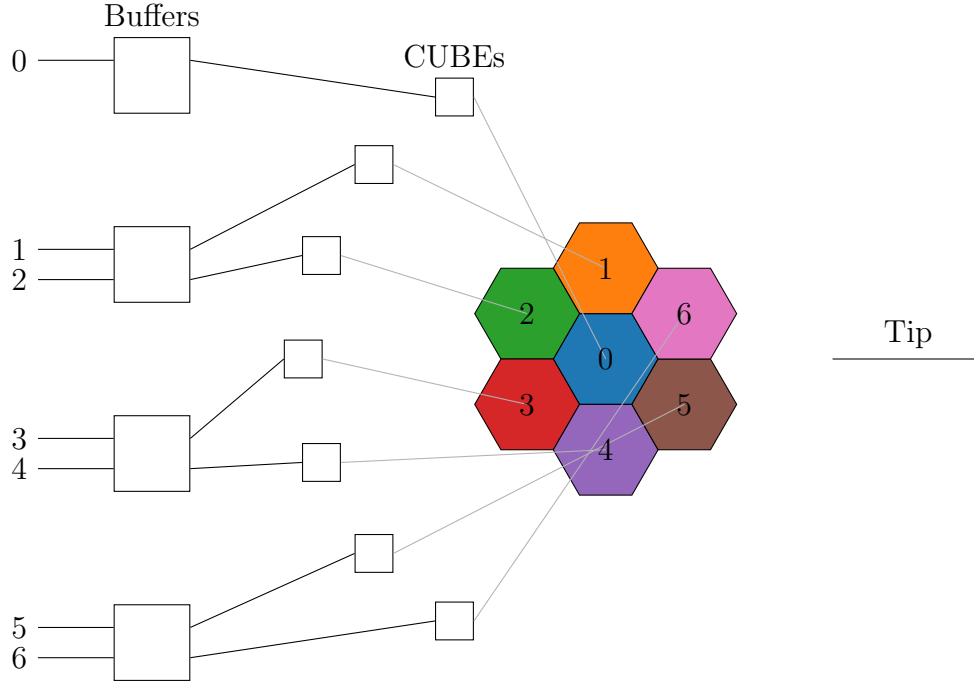where ϵ is the pair creation energy.–

A.3. Pixel Map

Figure A.1.: Pixel map for the TRISTAN FBM detector board. The buffers are dual operational amplifiers (ADA4807-2) each. This is the view to the top of the PCB (SDD entrance window side). Keep in mind that the CUBEs and the bonds (grey) are on the bottom side of the PCB.

A.4. DAQ ToDo List

During installation some issues occurred, that were not considered beforehand:

- If the stepper motors are active, the signal of all channels are completely noisy. This is a problem as the DAQ triggers to frequent and even crashes as it cannot handle such a high trigger throughput. Stopping and starting the DAQ for motor action is at the moment not possible, as the CoMPASS software cannot be scripted. The temporary solution to this was to set the *trigger holdoff* parameter to 5 µs, which limits the maximum event throughput to 200 kcps. This prevents the DAQ from crashing, but has the drawback that it introduces a significant deadtime to the tritium activity measurement. The issue can be resolved when the C/C++ API libraries are used for the DAQ communication instead of CoMPASS.

- During monitoring mode, the DAQ card will run for many days without a restart. The timestamps for the events are obtained from a card internal 100 MHz clock.

The error of this clock was measured to be 4 ppm, which leads to a time error of 3 s per week. Due to this shift the DAQ should be restarted every two weeks, to keep the time synchronization within ±10 s. The issue can also be resolved when the C/C++ API libraries, as a new DAQ run can ten be started on a regular time basis.

- In was planned to disable the *pole zero* correction in the DAQ card settings by choosing a very long time constant, because the shaping time of 300 ns is short compared to the decay time of 10 µs. This was later found out to cause events with non physical energy values, which is a not understood behavior of the moment. The solution was to set the *pole zero* correction to a reasonable value again. This should be investigate further

- Due to the long *trigger holdoff* the baseline correction cannot be applied, as events happening within the hold-off time are not excluded from the baseline calculation, as all events should be. It should be investigated how the baseline correction and a trigger hold-off can be combined. This may be irrelevant when the C/C++ API libraries are used.

A.5. Table of Materials in Vacuum

Table A.2 summarizes the used materials and parts of the new vacuum components of the TRISTAN FBM. This includes the detector board, the aluminum pad and the copper shielding. The cables and the connector are not included, as these components were reused from the previous setup.

#	Description	Material	Amount	Size
1	Pad	Aluminum EN AW-6060	1	Total surface: $\sim 70\,cm^2$
2	Cover	Copper	1	Total surface: $\sim 70\,cm^2$
3	Distance Holder	Copper	2	D3×5 mm
4	Screw	Copper	2	M2.5×3 mm
5	PCB	Kapton®	1	Total surface: $\sim 50\,cm^2$
6	CUBE amplifiers	Silicon	7	$750 \times 750 \times 250\,\mu m^3$
7	SDD	Silicon	1	$4 \times 4 \times 0.4\,mm^3$
8	SDD glue	EPO-TEK®920-FL		
9	SMD resistors		8	0805
10	SMD resistors		4	0603
11	SMD capacitors	X7R	4	1206
12	SMD capacitors	X7R	15	0603
13	SMD capacitors	X7R	12	0402
14	Op.amplifiers	ADA4807-2	4	MSOP8, $3 \times 3\,mm^2$

Table A.2.: List of materials

A.6. Bias Board

The bias board that is used for the FBM setup is shown in figure A.2. The board has 8 channel, thus on is not used.
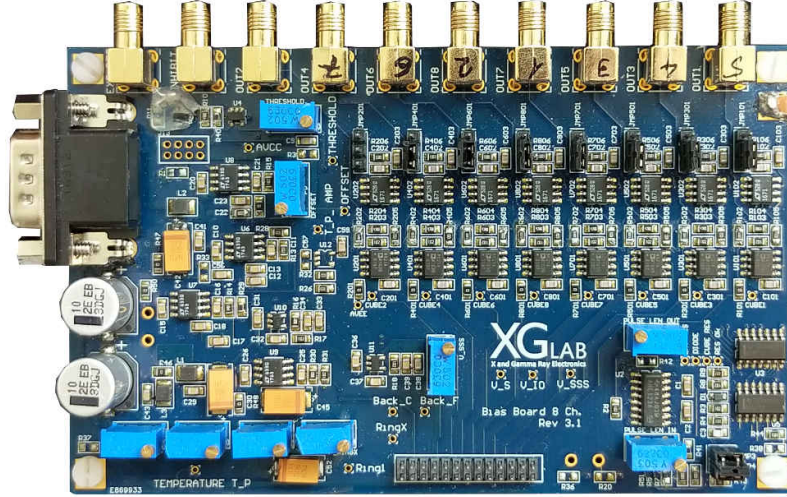
Figure A.2.: Bias board used for the FBM. The detector is attached to the 26-pin connector at the bottom. The board is supplied with high voltage (70 V and 130 V DC) and low voltage (±9 V) through the D-sub-9 connector at the left.

A.7. CAEN DAQ Settings

Table A.3.: CAEN v1781 DAQ settings used during KNM2

Energy filter	$T_{\text{shaping}} =$	300 ns
	$T_{\text{gap}} =$	300 ns
RCCR2 fast filter	$T_{\text{av}} =$	320 ns
	$T_{\text{diff}} =$	100 ns

Table A.4.: CAEN v1781 DAQ settings used in the ^{241}Am measurement

Energy filter	$T_{\text{shaping}} =$	300 ns
	$T_{\text{gap}} =$	500 ns
RCCR2 fast filter	$T_{\text{av}} =$	320 ns
	$T_{\text{diff}} =$	100 ns

Bibliography

[1]   C. L. Cowan et al. "Detection of the Free Neutrino: a Confirmation". In: *Science* 124.3212 (1956), pp. 103–104. ISSN: 0036-8075. DOI: `10.1126/science.124.3212.103`.

[2]   Raymond Davis, Don S. Harmer, and Kenneth C. Hoffman. "Search for Neutrinos from the Sun". In: *Physical Review Letters* 20.21 (1968), pp. 1205–1209. ISSN: 0031-9007. DOI: `10.1103/PhysRevLett.20.1205`.

[3]   A. Yu Smirnov. *Solar neutrinos: Oscillations or No-oscillations?* URL: `http://arxiv.org/pdf/1609.02386v2`.

[4]   Q. R. Ahmad et al. "Direct evidence for neutrino flavor transformation from neutral-current interactions in the Sudbury Neutrino Observatory". In: *Physical Review Letters* 89.1 (2002), p. 011301. ISSN: 0031-9007. DOI: `10.1103/PhysRevLett.89.011301`.

[5]   K. Eguchi et al. "First results from KamLAND: evidence for reactor antineutrino disappearance". In: *Physical Review Letters* 90.2 (2003), p. 021802. ISSN: 0031-9007. DOI: `10.1103/PhysRevLett.90.021802`.

[6]   Y. Fukuda et al. "Evidence for Oscillation of Atmospheric Neutrinos". In: *Physical Review Letters* 81.8 (1998), pp. 1562–1567. ISSN: 0031-9007. DOI: `10.1103/PhysRevLett.81.1562`.

[7]   M. Tanabashi et al. "Review of Particle Physics". In: *Physical Review D* 98.3 (2018). ISSN: 2470-0010. DOI: `10.1103/PhysRevD.98.030001`.

[8]   M. Agostini et al. "Improved Limit on Neutrinoless Double-β Decay of 76Ge from GERDA Phase II". In: *Physical Review Letters* 120.13 (2018), p. 132503. ISSN: 0031-9007. DOI: `10.1103/PhysRevLett.120.132503`.

[9]   E. W. Otten and C. Weinheimer. "Neutrino mass limit from tritium β decay". In: *Reports on Progress in Physics* 71.8 (2008), p. 086201. ISSN: 0022-3735. DOI: `10.1088/0034-4885/71/8/086201`.

[10]   M. Aker et al. *An improved upper limit on the neutrino mass from a direct kinematic method by KATRIN.* URL: `http://arxiv.org/pdf/1909.06048v1`.

[11]   Loredana Gastaldo. *Neutrino dark matter from an experimental perspective.* 2017. URL: `https://www.thphys.uni-heidelberg.de/~gk_ppbsm/lib/exe/fetch.php?media=undefined:colliding-pizza-loredana-gastaldo.pdf`.

[12] A. Boyarsky et al. "Sterile neutrino Dark Matter". In: *Progress in Particle and Nuclear Physics* 104 (2019), pp. 1–45. ISSN: 01466410. DOI: `10.1016/j.ppnp.2018.07.004`.

[13] Susanne Mertens et al. "A novel detector system for KATRIN to search for keV-scale sterile neutrinos". In: *Journal of Instrumentation* 46.6 (2019), p. 065203. ISSN: 1367-2630. DOI: `10.1088/1361-6471/ab12fe`.

[14] KATRIN Collaboration. *KATRIN design report*. Karlsruhe: FZKA, 2005.

[15] Nancy Wandkowsky. *Study of background and transmission properties of the KATRIN spectrometers*. 2013. DOI: `10.5445/IR/1000036631`.

[16] Enrico Ellinger. "Development and investigation of the Forward Beam Monitor for the KATRIN Experiment". Dissertation. Bergische Universität Wuppertal, 2019.

[17] Daniel Siegmann. "Investigation of the Detector Response to Electrons of the TRISTAN Prototype Detectors". Master thesis. Technical University of Munich, 2019.

[18] Marc Korzeczek. "Development of high-resolution Si-detectors to search for keV scale sterile neutrinos and analysis of initial KATRIN data". In preparation. Dissertation. Karlsruher Institut für Technologie.

[19] Tim Brunst et al. *Measurements with a TRISTAN prototype detector system at the "Troitsk nu-mass" experiment in integral and differential mode*. URL: `http://arxiv.org/pdf/1909.02898v4`.

[20] *Halbleiterlabor der Max-Planck-Gesellschaft*. URL: `https://www.hll.mpg.de/`.

[21] URL: `https://www.electronics-tutorials.ws/diode/diode_2.html` (visited on 11/26/2019).

[22] Glenn F. Knoll. *Radiation detection and measurement*. 4th ed. Hoboken, N.J.: Wiley, 2010. ISBN: 9780470131480.

[23] P. Lechner et al. "Silicon drift detectors for high count rate X-ray spectroscopy at room temperature". In: *Nuclear Instruments and Methods in Physics Research Section A: Accelerators, Spectrometers, Detectors and Associated Equipment* 458.1-2 (2001), pp. 281–287. ISSN: 01689002. DOI: `10.1016/S0168-9002(00)00872-X`.

[24] Luca Bombelli, Carlo Fiorini, and Tommaso Frizzi. "CUBE: The SDD Preamplifier For Excellent Energy-Resolution and High Count-Rate Performance". In: *Microscopy and Microanalysis* 24.S1 (2018), pp. 710–711. ISSN: 1431-9276. DOI: `10.1017/S143192761800404X`.

[25] R. C. Alig, S. Bloom, and C. W. Struck. "Scattering by ionization and phonon emission in semiconductors". In: *Physical Review B* 22.12 (1980), pp. 5565–5582. ISSN: 0163-1829. DOI: `10.1103/PhysRevB.22.5565`.

[26] Tiemo Steinmann. "Vacuum compatibility of high-enddetector components for a sterile neutrino search with KATRIN". In preparation. Bachelor Thesis. KIT Department of Physics, 2019.

[27] Stephen Seltzer. *XCOM-Photon Cross Sections Database, NIST Standard Reference Database 8*. 1987. DOI: 10.18434/T48G6X.

[28] Martin Descher. "High rate systematic effects for keV sterile neutrino searches at KATRIN". Master's Thesis. Institute of Experimental Particle Physics, 2019.

[29] U. Tietze and Ch. Schenk. *Halbleiter-Schaltungstechnik*. 4., völlig neuarb. und erw. Aufl. Berlin: Springer, 1978. ISBN: 0387086285.

[30] M. Zbořil et al. "Ultra-stable implanted 83 Rb/ 83 m Kr electron sources for the energy scale monitoring in the KATRIN experiment". In: *Journal of Instrumentation* 8.03 (2013), P03009–P03009. ISSN: 1367-2630. DOI: 10.1088/1748-0221/8/03/p03009.

[31] D. Vénos et al. "Properties of 83 mKr conversion electrons and their use in the KATRIN experiment". In: *Journal of Instrumentation* 13.02 (2018), T02012–T02012. ISSN: 1367-2630. DOI: 10.1088/1748-0221/13/02/T02012.

[32] Emilio Gatti et al. "Dynamics of electrons in drift detectors". In: *Nuclear Instruments and Methods in Physics Research Section A: Accelerators, Spectrometers, Detectors and Associated Equipment* 253.3 (1987), pp. 393–399. ISSN: 01689002. DOI: 10.1016/0168-9002(87)90522-5.

[33] M.-M. Bé et al. *Table of Radionuclides*. Vol. 5. Monographie BIPM-5. Pavillon de Breteuil, F-92310 Sèvres, France: Bureau International des Poids et Mesures, 2010. URL: http://www.bipm.org/utils/common/pdf/monographieRI/Monographie_BIPM-5_Tables_Vol5.pdf.

[34] Matthew Newville. *X-ray DB*. 2016. URL: http://scikit-beam.github.io/XrayDB.

[35] Pascal Renschler. *KESS - A new Monte Carlo simulation code for low-energy electron interactions in silicon detectors*. 2011. DOI: 10.5445/IR/1000024959.

Acknowledgments